

Influences of Anatomy and Blood Flow Changes in the Head Layers on Optical Mapping

Shuping Wang

Thesis submitted in Partial Fulfillment
of the Requirements for the Degree of
Doctor of Philosophy

The University of Electro-Communications
Tokyo, Japan

March, 2014

Influences of Anatomy and Blood Flow Changes in the Head Layers on Optical Mapping

APPROVED BY SUPERVISORY COMMITTEE:

CHAIRPERSON: Professor Takuji KOIKE

MEMBER: Professor Makoto SHIMOJO

MEMBER: Professor Hiroshi YOKOI

MEMBER: Professor Yukio YAMADA

MEMBER: Professor Eiji OKADA

MEMBER: Associate Professor Kazuto MASAMOTO

Copyright

by

Shuping Wang

2014

概要

脳上部の頭部各層における解剖学的および生理学的変化が脳活動の光マッピング画像に与える影響を調べるために、数値計算シミュレーションおよびファントム（模擬試料）実験を行った。シミュレーションではヒト頭部を模擬した多層モデルを対象として光拡散方程式を有限要素法により解いて光マッピングの画像を得、ファントム実験では多チャンネルの連続光型近赤外分光システムを用いて画像を得た。特に、頭蓋骨と脳脊髄液(CSF)層の厚さ、およびCSF層内に存在する太い血管や皮膚層の血液動態が光マッピング画像に与える影響を定量的に評価・議論した。この結果から、ヒト頭部の個体差や脳上部の血液動態がマッピング画像における影響を補正することが可能になる。

Abstract

Optical mapping has been applied to image brain activation two-dimensionally along the head surface by detecting the intensity changes of light that passes through the brain. In optical mapping for imaging brain activity, it is assumed that the head tissue is spatially homogeneous and temporally invariable except the activated region in the brain. However, in the superficial layers above the brain, the tissues are inhomogeneous and vary hemodynamically. Furthermore, light propagation and the optical pathlength inside the head are highly dependent on the anatomy and physiology in the head.

In particular, the spatial variations in the thickness of skull and cerebrospinal fluid (CSF) layers, the existence of the blood vessels and the hemodynamic changes in the superficial layers such as the CSF and skin layers would have significant influences on light propagation and would result in the difference in the mapping images. However, it is difficult to know these influences by *in vivo* experiments.

The aim of this study is to investigate these influences by numerical and experimental methods. Three-dimensional head models are used to simulate light propagation in the head by solving the photon diffusion equation using the finite element method (FEM), and the optical mapping images are constructed from the simulated measurement data. Tissue-mimicking phantoms with spatially varying thickness and changeable optical properties of head layers were also developed and multi-channel near-infrared spectroscopy (NIRS) experiments were performed on the dynamic phantoms.

In the numerical simulations and phantom experiments, the changes in the optical densities (ΔOD) due to activated regions are obtained to construct the mapping images, and the light path probability distributions between one pair of source and detector are calculated to show the sensitivity of the tissue regions to the mapping images. As the results, the influences of (1) the spatial variations of the skull and CSF layers and (2) the blood volume changes in the skin and CSF layers on the mapping images of brain

activities are investigated quantitatively. The optical mapping for the single or multiple activated regions and the effects of the position of the activated regions relative to the probe arrays on mapping images are also discussed.

The quantitative results about the influences of the superficial layers in this study provide information for compensating the optical mapping images among different individuals or different head regions in an individual. *In vivo* experiments considering the influences of structural and hemodynamic differences in the superficial layers on optical mapping remain as a future subject.

Contents

List of Figures	i
------------------------------	----------

List of Tables	vi
-----------------------------	-----------

Abbreviations & Symbols.....	vii
---	------------

Chapter 1 Introduction.....	1
------------------------------------	----------

1.1 OVERVIEW	1
1.2 OPTICAL MAPPING	1
1.2.1 <i>Disadvantages of optical mapping</i>	2
1.2.2 <i>Comparison with other human functional imaging</i>	4
1.3 ANATOMY OF HUMAN HEAD	4
1.4 RESEARCH MOTIVATION	6
1.5 MAIN CONTRIBUTION OF THE DISSERTATION.....	7
1.6 OUTLINE OF THE DISSERTATION	8

Chapter 2 Methods of numerical simulations and phantom experiments of optical mapping.....	10
---	-----------

2.1 NIR LIGHT PROPAGATION IN THE HUMAN HEAD.....	10
2.1.1 <i>Introduction</i>	10
2.1.2 <i>Absorption and scattering of light in the human head</i>	11
2.1.3 <i>Modeling of light propagation in tissues</i>	14
2.2 THEORY OF OPTICAL MAPPING	16
2.3 SIMULATION OF OPTICAL MAPPING	21
2.3.1 <i>Modeling of optical mapping</i>	21
2.3.2 <i>Modeling of light propagation</i>	22

2.4 PHANTOM EXPERIMENTS.....	25
2.4.1 Materials and methods of manufacturing tissue mimicking phantoms.....	25
2.4.2 Measurement of the optical properties of the phantom	25
2.4.3 Design of the phantom.....	28
2.4.4 Measuring system for optical mapping	29

Chapter 3 Effects of Spatial Variations of Skull and Cerebrospinal Fluid Layers on Optical Mapping of

Brain Activities: Numerical Study..... 33

3.1 INTRODUCTION.....	33
3.2 MODEL OF HUMAN HEAD FOR OPTICAL MAPPING	34
3.3 RESULTS AND DISCUSSION	37
3.3.1 Effect of the thickness of the skull layer on mapping images	37
3.3.2 Effect of the variation in the thickness of the CSF layer on mapping images	48
3.4 CONCLUSIONS	56

Chapter 4 Effects of Spatial Variation of Skull and Cerebrospinal Fluid Layers on Optical Mapping of

Brain Activities: Phantom Experiments..... 59

4.1 INTRODUCTION.....	59
4.2 HEAD PHANTOMS	60
4.2.1 Variation of the skull thickness	60
4.2.2 Variation of the CSF thickness.....	61
4.3 RESULTS AND DISCUSSIONS	65
4.4 CONCLUSIONS	74

Chapter 5 Influences of Blood Volume Changes in

Cerebrospinal Fluid and Skin Layers on Optical

Mapping: Numerical Study..... 75

5.1 INTRODUCTION.....	75
5.2 QUALITATIVE EXPLANATION OF THE INFLUENCE OF THE SUPERFICIAL LAYERS ON OPTICAL MAPPING.....	76
5.2.1 Reference state.....	76
5.2.2 Existence of blood vessel in the CSF layer.....	78
5.2.3 Blood volume changes in the skin layer	80
5.3 ESTIMATION OF THE ABSORPTION COEFFICIENT IN THE SKIN LAYER WITH INCREASED BLOOD VOLUME	82
5.4 MODELS OF HUMAN HEAD WITH ACTIVATED REGION, BLOOD VESSEL IN THE CSF AND BLOOD VOLUME CHANGES IN THE SKIN	85
5.4. 1 Blood vessel in the CSF layer.....	86
5.4. 2 Blood volume changes in the skin layer	88
5.5 RESULTS	89
5.5.1 Influence of the blood vessel in the CSF layer on mapping images	89
5.5.2 Influence of the blood volume changes in the skin layer on mapping images.....	94
5.5.3 When the blood volume in the skin layer increases simultaneously with the brain activation.....	99
5.6 DISCUSSION AND CONCLUSION.....	102

Chapter 6 Influences of Blood Volume Changes in

Cerebrospinal Fluid and Skin Layers on Optical

Mapping: phantom experiments 104

6.1 INTRODUCTION.....	104
6.2 HEAD PHANTOM	105
6.2.1 Head model with a blood vessel in the CSF layer.....	105
6.2.2 Head model with blood volume changes in the skin layer.....	106

6.3 MEASURING METHODS	108
6.4 EXPERIMENTAL RESULTS	110
6.4.1 <i>Effect of the blood vessel in the CSF layer</i>	110
6.4.2 <i>Effect of the blood volume changes in the skin layer</i>	113
6.5 DISCUSSIONS AND CONCLUSIONS	114
Chapter 7 General Conclusions	117
References.....	119
Acknowledgements	126
Publications	127

List of Figures

Fig. 1.1: (a) Side view of the human head, and (b) skull of the human head (from Merck manual of medical information, 2003)..... 5

Fig. 1.2: Anatomy of the CSF layer and sagittal sinus (from Human Anatomy, 6th edition, 2009).
..... 6

Fig. 2.1: A NIR light traveling through the head in a banana-shaped photon path. 10

Fig. 2.2: (a) Attenuation of light through a non-scattering medium. (b) Attenuation of light through a scattering medium. 12

Fig. 2.3: Absorption spectra of oxy-Hb and deoxy-Hb. 12

Fig. 2.4: Scattering phase function. The incident light travels in the \hat{s} direction and the scattered photon exits in the \hat{s}' direction..... 13

Fig. 2.5: The changes in the concentrations of HbO₂, Hb and total-Hb in a typical fNIRS measurement for brain activation. The shadow area indicates the stimulus duration. 17

Fig. 2.6: (a) rest state, and (b) activated state with an activated region in the gray matter. 17

Fig. 2.7: Arrangement of the sources, detectors, data points and activated region. 21

Fig. 2.8: The light path probability of light detected after passing through the position r . $\phi_s(r)$ is the fluence rate at the position r for light injected at the source position. $\phi_d(r)$ is the fluence rate at the position r for light injected at the detector position..... 24

Fig. 2.9: Calibration results of the optical properties. (a) μ_s' of the epoxy resin as a function of the mass fractions of the TiO_2 particles, f_{mT} , and (b) μ_a of the epoxy resin as a function of the mass fractions of the black ink, f_{mI} 27

Fig. 2.10: Design of five-layered phantom with rest rod and activated rod..... 28

Fig. 2.11: NIRS imaging system (FOIRE-3000) and block diagram of the system configuration. 31

Fig. 2.12: Side view of the phantom experimental setup. 32

Fig. 3.1: Simulation models of human heads having five layers; skin, skull, CSF, gray matter, and white matter layers. The thickness of the skull or CSF layer is (a) uniform or (b) linearly varying in the x -direction, and the other layers are assumed uniform. 35

Fig. 3.2: Arrangement of the sources, detectors, data points, and activated regions..... 36

where ΔOD_m is the maximum of ΔOD and t_s is the skull thickness. The relationship of ΔOD_m and t_s is an exponentially decreasing function, and ΔOD_m decreases to 40 % of its original value with every 1 mm increase in the skull thickness. Due to the strong light scattering by the skull layer, the value of ΔOD decreases significantly as the skull thickness increases. With the same scaling of ΔOD of 5×10^{-3} , the image of the activated region for (S3) is not observable as stated above. However, when the ΔOD values are normalized by the ΔOD_m in each case of Fig. 3.3, almost the same images of ΔOD for (S1), (S2) and (S3) are obtained although the figures are not presented. This can be quantitatively understood by calculating the full width at half maximum (FWHM) of the ΔOD profiles. Fig. 3.3 (d) shows the ΔOD profiles along the line in the x -direction indicated by the chain lines in panels (a), (b) and (c). The FWHMs of the curves in Fig. 3.3 are 24.7 mm, 24.9 mm and

25.9 mm for (S1), (S2) and (S3), respectively, and this slight change in the FWHM is hardly observable in the mapping image..... 38

Fig. 3.4: Simulated optical mapping images of single activated regions at position A for the uniform skull layers with the thicknesses of (a) 5 mm (S1), (b) 10 mm (S2), and (c) 20 mm (S3). Panel (d) shows the ΔOD profiles along the line in the x -direction indicated by the chain lines in panels (a), (b) and (c). 39

Fig. 3.5: Simulated optical mapping images of (a) single activated regions at position A or (b) that at position B, and (c) of double activated regions at positions A&B for the uniform skull layers with the thicknesses of 5 mm (S1). Panel (d) shows the ΔOD profiles along the line in the x -direction indicated by the chain lines in panels (a), (b) and (c). 41

Fig. 3.6: Simulated optical mapping images of single activated regions at position A for the spatially varying thicknesses of the skull layer, (a) from 5 mm to 10 mm (S4) and (b) from 5 mm to 20 mm (S5). Panel (c) shows the ΔOD profiles along the line in the x -direction going through the center of the activated region at position A shown by the chain lines in panels (a) and (b). Panel (d) shows the ΔOD profiles similar to panel(c) expect that the activated region is at position B for (S4) and (S5). 43

Fig. 3.7: Simulated optical mapping images of double activated regions with the spatially varying thickness of the skull layer from 5 mm to 10 mm (S4); (a) for the active regions at position A, and (b) for those at position B. Panel (c) shows the ΔOD profiles along the line in the x -direction shown by the chain lines in panels (a) and (b). 44

Fig. 3.8: Calculated path probability (sensitivity) distributions, $\log_{10}(\psi)$, for the uniform skull layers with the thickness of (a) 5 mm (S1), (b) 10 mm (S2), and (c) 20 mm (S3). Thick

solid curves indicate the contours of constant $\log_{10}(\psi)$ with the value of 12.5 % of the maximum $\log_{10}(\psi)$ in each case. (d) The integrated value of ψ in the gray matter for (S1), (S2) and (S3). 47

Fig. 3.9: Simulated optical mapping images of single activated regions at position A for the uniform CSF layers with the thicknesses of (a) 0 mm (C0), (b) 1 mm (C1), (c) 3 mm (C2), and (d) 6 mm (C3). Panel (e) shows the ΔOD profiles along the lines in the x-direction indicated by the chain lines in panels (a) to (d). (f) The maximum of ΔOD for (C0) ~ (C3). 49

Fig. 3.10: Simulated optical mapping images of single activated regions at position A for the spatially varying thickness of the CSF layer, (a) from 1 mm to 3 mm (C4) and (b) from 1 mm to 6 mm (C5). Panel (c) shows the ΔOD profiles along the line in the x-direction shown by the chain lines in the panels (a) and (b). 51

Fig. 3.11: Simulated optical mapping images of double activated regions with the spatially varying thickness of the CSF layer from 1 mm to 6 mm (C5); (a) for the active regions at position A, and (b) for those at position B. Panel (c) shows the ΔOD profiles along the line in the x-direction shown by the chain lines in the panels (a) and (b). 53

Fig. 3.12: Calculated path probability (sensitivity) distributions, $\log_{10}(\psi)$, for the uniform CSF layers with the thickness of 0 mm (C0), 1 mm (C1), 3 mm (C2), and 6 mm (C3). Thick solid curves indicate the contours of constant $\log_{10}(\psi)$ with the value of 12.5 % of the maximum $\log_{10}(\psi)$ in each case. (e) The integrated value of ψ in the gray matter for (C0) ~ (C3). 55

Fig. 3.13: (a) Simulation model with sulcus in gray matter. The optical properties of sulcus is the same with that of the CSF layer. (b) ΔOD profiles along the line in the x -direction going through the center of the activated region at position A for the cases of no sulcus and with sulcus in the gray matter..... 56

Fig. 4.1: Human head phantoms with a uniform thickness of the skull layer, (S1) 5 mm, (S2) 10 mm and (S3) 15 mm..... 60

Fig. 4.2: Human head phantoms with linearly varying thickness of the skull layer in the x -direction, (a) (S4) skull: 5 mm-10 mm, (b) (S5) skull: 5 mm-20 mm. (c) Rods simulating the rest and activated states in the gray matter for (S4) and (S5)..... 61

Fig. 4.3: Human head phantoms with a uniform thickness of the CSF layer. (C1) 0 mm, (C2) 1 mm and (C3) 3 mm. 62

Fig. 4.4: Human head phantoms with the linearly varying thickness of the CSF layer in the x -direction. (a) (C4) CSF: 1 mm-3 mm, (b) (C5) CSF: 1 mm-6 mm. (c) Rods simulating the rest and activated states in the gray matter for (C4) and (C5)..... 63

Fig. 4.5: Arrangement of the sources, detectors, data points and activated regions. (a) Single activated region for the uniform thickness of the skull or CSF layer, (b) Double activated regions for the linearly varying thickness in the x -direction of skull or CSF layer. Positions B and D in the gray matter layer were below the middle of the four neighboring data points, positions A and C in the gray matter layer below the data points. 64

Fig. 4.6: Optical mapping images of single activated region at position A or B obtained by phantom experiments, for the uniform skull thickness of (S1) 5 mm, (S2) 10 mm and (S3) 15 mm. The dashed circles in the mapping images indicate the true activated regions..... 65

Fig. 4.7: Maxima of ΔOD in the activated regions at position A or B as a function of the uniform skull thickness of (S1) 5 mm, (S2) 10 mm and (S3) 15 mm. Error bars represent the standard deviations of the repeated five measurements. 66

Fig. 4.8: Optical mapping images obtained by phantom experiment for the linearly varying skull thickness with (S4) 5 mm - 10mm and (S5) 5 mm - 20mm when the double activated regions were located at position C or D. The dashed horizontal lines pass through the centers of the double activated regions. 67

Fig. 4.9: Profiles of ΔOD along the dashed lines in Fig. 4.8. (S4-C) skull thickness varying from 5 mm to 10 mm with the double activated regions at position C, (S5-C) skull thickness varying from 5 mm to 20 mm with the double activated regions at position C, (S4-D) skull thickness varying from 5 mm to 10 mm with the double activated regions at position D, and (S5-D) skull thickness varying from 5 mm to 20mm with the double activated regions at position D. 68

Fig. 4.10: Optical mapping images by phantom experiments for the uniform CSF thickness, (C1) 0 mm, (C2) 1 mm and (C3) 3 mm with the activated region at position A or B. 70

Fig. 4.11: Maximum of ΔOD in the mapping images for the cases of uniform CSF thicknesses with the activated regions at positions A and B. Error bars represent the SD of repeated five measurements. 71

Fig. 4.12: Optical mapping images by the phantom experiments for the cases of linearly varying CSF thickness, (C4) 1 mm - 3mm and (C5) 1 mm - 6 mm with the double activated regions at positions C or D. The dashed lines indicate the horizontal line through the center of the activated region. 72

Fig. 4.13: Profile of ΔOD along the dashed lines in Fig. 4.12. (C4-C) varying CSF thickness from 1 mm to 3 mm with the double activated regions at position C, (C5-C) varying CSF thickness from 1 mm to 6 mm with the double activated regions at position C, (C4-D) varying CSF thickness from 1 mm to 3 mm with the double activated regions at position D, and (C5-D) varying CSF thickness from 1 mm to 6 mm with the double activated regions at position D. 73

Fig. 5.1: A cross-section of the head model with an activated region in the gray matter and the standard state of the superficial layers. 77

Fig. 5.2: A cross-section of the head model indicating a thick blood vessel existing in the CSF layer and an activated region in the gray matter layer..... 79

Fig. 5.3: A cross- section of head model indicating blood flow changes in the skin layer and an activated region in the gray matter layer. 81

Fig. 5.4: The simulation model of the human head for optical mapping with an activated disk region..... 86

Fig. 5.5: (a) The blood vessel model in the CSF layer, and (b) the cross-section of the CSF layer with a thick blood vessel. 87

Fig. 5.6: The skin layer model of the epidermis (1.0 mm) and dermis (4.0 mm). The dermis layer is exchangeable with the layers having different absorption coefficients. 89

Fig. 5.7: The simulation results of mapping images with or without a blood vessel in the CSF layer. (A)-(E) simulated mapping images of cases (C1)-(C5). (F) the profiles of ΔOD along the horizontal lines (indicated by the blue dashed lines in image (A)) through the center of the activated region. 90

Fig. 5.8: The maximum of ΔOD to the profiles of ΔOD along the horizontal lines through the center of the activated region as for Fig. 5.7 (F). 91

Fig. 5.9: (A) Top view of the head model shows the distance between the activated region and the square vessel. The profiles of ΔOD along the horizontal line through the center of the activated regions a function of the distance between the activated region and (B) the square vessel with the size of 1 mm-side having μ_a of 0.26 mm^{-1} , and (C) the rectangular vessel with the size of 1 mm \times 2 mm having μ_a of 0.26 mm^{-1} 93

Fig. 5.10: The simulation results of the mapping images for cases (S1), (S2) and (S3) where μ_{a-skin} of the dermis layer changes. 95

Fig. 5.11: (A) The measured light intensities, Φ^n and Φ^a , and (B) OD at the 24 data points for three cases of different μ_a of dermis layer. Superscripts “a” and “n” indicate the activated and rest states. 96

Fig. 5.12: The lightpath probability distributions $\psi(r)$ for three cases of different μ_{a-skin} 97

Fig. 5.13: The ratios of ψ_{gray}/ψ_{skin} in Table 5.4 are plotted..... 98

Fig. 6.1: Head model and blood vessel phantoms to be inserted into the CSF layer. 105

Fig. 6.2: Head model with blood volume changes in the skin layer..... 107

Fig. 6.3: An example of the measured OD values in the measurement process for studying the effect of the blood vessel in the CSF layer. OD values at the data point 9 are shown. The vessel size was 150mm \times 1mm \times 1mm, and its $\mu_a = 0.13 \text{ mm}^{-1}$ 108

Fig. 6.4: (left) Arrangements of source, detector, data point and the position of the activated region in the gray matter. (right) green dots are the averages of ΔOD at 24 data points, and the red error bars are the standard deviation for repeated five measurements. 110

Fig. 6.5: (A) Top view of the head model including the activated region in the gray matter and blood vessel in the CSF layer. (B)-(F) experimental mapping images of cases (C1)-(C5). The dashed circle and rectangular superimposed on the mapping images indicated the shapes of the activated region and blood vessel. (G) the profiles of ΔOD along the horizontal lines through the center of the activated region. 111

Fig. 6.6: (A) Top view of the head model including the activated region in gray matter and blood vessel in CSF layer. (B) to (E) experimentally obtained mapping images for different distances, (B) $d = 5$ mm, (C) $d = 10$ mm, (D) $d = 15$ mm, and (E) $d = 20$ mm for the blood vessel having a 1-mm \times 2-mm rectangular shape with $\mu_a = 0.26$ mm⁻¹. The dashed circles and rectangles superimposed on the mapping images indicate the shapes of the activated region and blood vessel. (F) the profiles of ΔOD along the horizontal lines through the center of the activated region. The dashed green and red curves show the profiles of ΔOD for no vessel and $d = 0$ mm. 113

Fig. 6.7: (A) to (C) The experimental mapping images of cases (S1) to (S3), respectively. (D) the profiles of ΔOD along the horizontal lines through the center of the activated region. 114

Fig. 6.8: The comparison of simulation and phantom experimental results of 24 ΔOD s. A head phantom with no vessel in the CSF layer was used. 115

List of Tables

Table 2.1	The optical properties of the head models (805nm).....	29
Table 2.2	FOIRE-3000 Specifications.....	30
Table 3.1	Thicknesses of the skull and CSF layers.	37
Table 5.1	The optical properties of the dermis layer with blood volume changes.....	85
Table 5-2	Cases of a thick blood vessel existing in the CSF layer.....	87
Table 5-3	Cases of blood volume changes in the dermis layer.....	88
Table 5-4	The lightpath probabilities averaged over the skin and gray matter layers. The ranges of the averaging in the skin and gray matter layers are marked in Fig 5.12 as dashed line.....	97
Table 6-1	The size and optical properties of blood vessel in the CSF layer.....	106
Table 6-2	The optical properties of the skin layer consisting of the epidermis and dermis. ..	107

Abbreviations & Symbols

Abbreviations

BOLD	blood oxygen level dependent
CBF	cerebral blood flow
CBV	cerebral blood volume
CSF	cerebrospinal fluid
CW	continuous wave
DOT	diffuse optical tomography
EEG	electroencephalography
FEM	finite element method
FWHM	full width at half maximum
fMRI	functional magnetic resonance imaging
fNIRS	functional near-infrared spectroscopy
Hb	deoxyhaemoglobin
HbO ₂	oxy-haemoglobin
ICA	independent component analysis
LCD	liquid crystal display
NIRS	near-infrared spectroscopy
OD	optical density
SD	standard deviations
SO ₂	blood oxygen saturation
TiO ₂	titanium oxide

Symbols

C	molar concentration
c	speed of light
D	diffusion coefficient
d	medium thickness
f_{mT}	mass fraction of TiO ₂ particles in the phantoms
f_{mI}	mass fraction of black ink in the phantoms
f_v	blood volume fraction
g	anisotropy factor of scattering

I	radiance
J	photon flux
l	effective pathlength
p	scattering phase function
q	source light power
q_0	integrated source function
r	position
S	optical attenuation due to scattering
\hat{s}	direction of scattered light
\hat{s}'	direction of incident light
t	time

Greek symbols

ε	molar extinction coefficient
λ	wavelength
μ_a	absorption coefficient
μ_s	scattering coefficient
μ'_s	reduced scattering coefficient. $\mu'_s = \mu_s(1 - g)$
Φ	detected light intensity
Φ_0	source light intensity
ϕ	photon fluence rate
ϕ_d	fluence rate when light is incident at the detector position.
ϕ_s	fluence rate when light is incident at the source position.
ψ	path probability distribution between the source and detector position.
θ	polar angle of scattering

Chapter 1 Introduction

1.1 Overview

In the last two decades, near-infrared spectroscopy (NIRS) has significantly developed from basic studies to clinical applications, particularly in the field of neuroimaging. NIRS is rooted in oximetry, which measures blood oxygenation based on the different absorption spectra of oxy- and deoxyhaemoglobin (HbO₂ and Hb) [1]. Functional optical imaging uses light in the NIR spectral window approximately from 700 nm to 900 nm, at which the overall absorption and scatter of light by tissues are relatively weak.

Frans Jöbsis first reported the noninvasive *in vivo* application of NIRS [2]. Since the early 1990s, when first functional NIRS (fNIRS) study using single-channel measurement was proposed, fNIRS research has gained a new dimension as a useful tool to understand brain disorders in both adults and neonates [3-6].

An obvious limitation of single-channel NIRS is the lack of spatial information. By employing multiple-channel NIRS measurements, the signals from brain cortex can be located. Hitachi Medical Corporation first introduced the concept of so-called optical topography [7]. Optical topography is a continuous wave multi-channel technology to map brain activity 2-dimensionally over a large area of the head surface by measuring reflectances at multiple positions simultaneously [8-10].

1.2 Optical mapping

Commercial instruments for optical mapping (or optical topography) have been developed using continuous wave (CW) measurement based on the modified Beer-Lambert law [11, 12]. Optical mapping allows us to observe hemodynamic changes in the outer region of the brain. Light detected by pairs of source and detector optical fibers varies with the changes in the hemoglobin concentration associated with the

activation of the brain. The source-detector separation is set around 30 mm and gives a penetration depth of about 15 mm, which is sufficient for sampling the adult cortex. Mapping images are constructed using an interpolation (or simple backprojection) approach and presented two-dimensionally along the plane including the sources and detectors.

1.2.1 Disadvantages of optical mapping

There are several disadvantages associated with optical mapping.

- Quantification of hemoglobin concentration changes.

The major problem caused by using CW measurements is the low quantitiveness of hemoglobin concentration changes in human brain. It is because that the optical path length, absorption coefficient and scattering coefficient in the tissue cannot be determined by CW measurements. Then, optical mapping can only show the relative information of brain activity by detecting changes in the light intensity with an assumption that the baseline is constant. Several approaches for better quantification of optical mapping images have been proposed, e.g., time-resolved and frequency-resolved NIRS measurements [13, 14]. The pathlength of individual photons can be recorded by time-domain measurement, which employs a source of ultrashort light pulses and a fast time-resolved detector [15]. The temporal profile of the emerging light can also be obtained by frequency-resolved measurement, using the relation between the time and frequency signals being the Fourier transform. However, due to high-costs and relatively big sizes, they are almost used as laboratory-based devices.

- The influence of the superficial layer.

Optical mapping uses near-infrared light which propagates through the superficial tissues, such as the skin, skull and cerebrospinal fluid (CSF) layers over the brain. Optical mapping is sensitive to blood volumes in the superficial tissues because oxygenated and deoxygenated hemoglobins are the dominant

chromophores in the near infrared window. The existence of the blood vessels and the hemodynamic changes in the superficial layers should be taken into account. Many previous studies have investigated the effects of blood volume changes in the superficial layers on fNIRS signals [16-18]. Several methods have been proposed to eliminate the effect of the blood volume changes in the skin layer, such as the independent component analysis (ICA) and employment of multi-distance optodes [19,20]. Using multi-distance optodes have illustrated the potential to eliminate the skin blood flow on the forehead. More recently, a combination of multi-distance (MD) optodes and ICA, called MD-ICA method [21] is proposed to eliminate the absorption change in the superficial layer. In addition, a method for separating functional and systemic signals based on their hemodynamic differences has been proposed [22].

- Individual difference.

As described later in Sec. 1.3, the anatomy of human head is individually different. The variability in brain anatomy among individuals causes uncertainty in optical mapping. The sensitivity of the NIRS signal to the hemodynamic changes was found to be dependent on the source-detector distance and the model used for investigation [23]. Comparison of the optical mapping images among subjects or regions within a single subject is impossible. A previous study has used MRI to be combined with NIRS to show the structural and functional images simultaneously. Prior anatomical information was first used in the forward problem for image reconstruction of diffuse optical tomography by Pogue et al. [24], and by Schweiger et al. [25]. In optical mapping, Kawaguchi et al [26]. proposed an image reconstruction algorithm using a prior knowledge of the spatial sensitivity profile to improve the optical mapping images.

Although these problems have not yet been overcome, the potential benefits of optical mapping are considerable since optical mapping is safe, noninvasive, portable, does not require strict motion restriction and can be wireless. In addition, optical mapping offers the possibility of simultaneous measurement of neuronal

and vascular signals in the brain with temporal resolution up to the order of ms.

1.2.2 Comparison with other human functional imaging

- Functional magnetic resonance imaging (fMRI), is currently the most popular technology for imaging functional brain activation, which measures blood-oxygen-level-dependent (BOLD) based signals [27]. fMRI uses the magnetic property of deoxy-Hb different from that of water or other tissues and measures relative changes in the concentration of deoxy-Hb. fMRI can image the entire brain and has a better spatial resolution with the order of 1 mm^2 . In contrast, the region where optical mapping is available limited to the outer cortex and its spatial resolution is on the order of 1 cm^2 . However, optical mapping can be applied to developmental studies of infants and children and to patients with significant symptoms that are impossible to be checked with fMRI.
- Electroencephalographic (EEG) records electrical signals at the scalp by measuring voltage fluctuations from ionic current flows within the neurons of the brain [28]. The limitation of EEG is that the precise locations of electrical sources cannot be provided. It seems probable that optical mapping combined with EEG provides more enhanced spatial information.
- Diffuse optical tomography (DOT) uses widely distributed sources and detectors to measure light which passed through the brain and to obtain sectional images of the hemodynamics in the head [29, 30]. It solves the forward and inverse problems to reconstruct the distributions of the scattering and absorption coefficients in the head. Due to scattering, DOT is usually used for relatively small sizes of tissues, e.g., infant's head, breast and arm.

1.3 Anatomy of human head

For numerical simulations and phantom experiments of optical brain imaging, the structure of the head must be considered to estimate light propagation in it. The human

head consists of skin (scalp), skull, CSF and brain (gray matter and white matter) as shown in Fig. 1.1(a). Among them, skin, skull and CSF layers are barriers to protect the brain against accidents and illnesses.

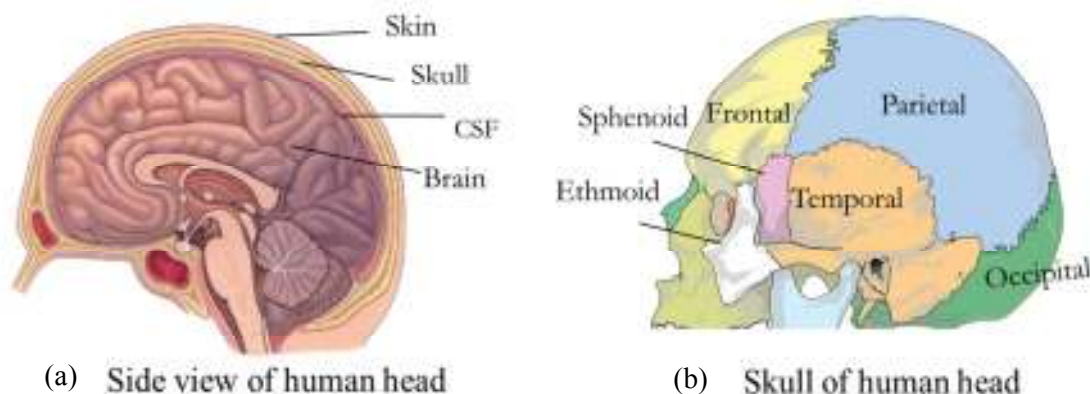


Fig. 1.1: (a) Side view of the human head, and (b) skull of the human head (from Merck manual of medical information, 2003).

Skull is covered by scalp and formed by the combination of 8 juxtaposed bones, 2 pairs (temporal and parietal) and odd 4 (frontal, sphenoid, ethmoid and occipital) as shown in Fig. 1.1(b). Temporal bone is the thinnest and occipital bone is the thickest. The thickness of skull varies from 4mm~10mm for adult [31].

Dura mater is a wrapper of the brain as shown in Fig. 1.2. Arachnoid space exist just inside dura mater. CSF is a low-scattering and absorbing liquid that is located in the space between arachnoid and pia mater. The thickness of the CSF layer is 1 mm ~ 3 mm changing with age, and easily varies because it is between the skull and the brain which can move or expand [32]. The CSF layer is a region in the head where small trabeculae and blood vessels are weaved through this space. It has been suggested that the presence of CSF in the head will affect light propagation in the brain during measurements for optical imaging and NIRS [33, 34].

Sagittal sinus is covered by dura mater and filled with venous blood which absorbs light strongly. The diameter of sagittal sinus is about 1 mm to 2 mm. Finally, pia mater is very tenuous and highly vascularized membrane attached closely to the cerebral cortex.

The skin and CSF layers are anatomically separated by the skull layer, and the physiological changes in the intracranial and extracranial blood volumes due to vaso-dilation or vaso-constriction should be taken into account because they have great effects on light propagation and mapping images.

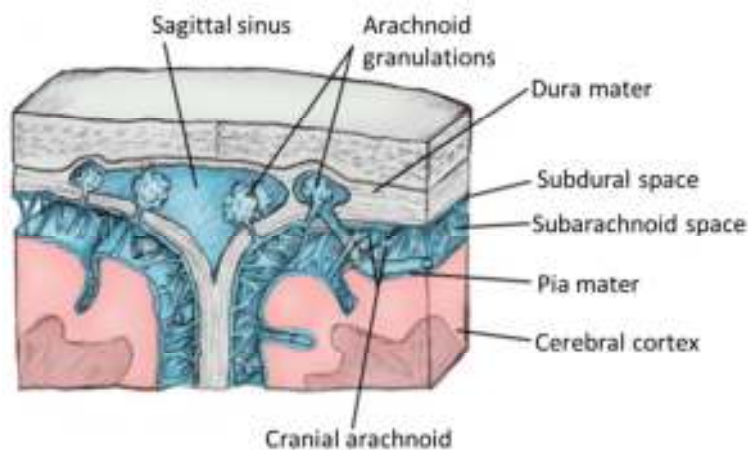


Fig. 1.2: Anatomy of the CSF layer and sagittal sinus (from Human Anatomy, 6th edition, 2009).

1.4 Research motivation

In optical mapping, images of the changes in the product of the absorption coefficient and the optical pathlength are constructed by a simple algorithm. However, it is impossible to determine the optical pathlength as long as CW light is employed. Because the near-infrared light passes through the superficial layers of the head both before and after reaching the brain, light propagation and the optical pathlength inside the head are highly dependent on the anatomy and physiology in the head. In particular, the spatial variations in the thickness of skull and CSF layers, the existence of the blood vessels and the hemodynamic changes in the superficial layers such as the CSF and skin layers would have significant influences on light propagation and resulting optical mapping images. But, it is difficult to know these influences by *in vivo* experiments.

Numerical simulation of optical mapping is an effective way to assess the

sensitivity of the detected signals to brain activation, because the signals specifically arising from the brain tissue cannot be detected experimentally. In contrast, the origins of the signals can be estimated by numerical simulation.

To investigate the influences of the anatomical and physiological changes in the superficial layers on the optical mapping images, numerical simulations of optical mapping are performed by solving the photon diffusion equation for layered-models simulating human heads using the finite element method (FEM), and phantom experiments are carried out using a multi-channel CW-NIRS system. Previously these influences have been studied by fMRI [35,36], DOT [37,38] and one-channel NIRS [39]. In optical mapping, to my knowledge, this study is the first to investigate the influences of the spatial variations in the thickness of skull and CSF layers and the hemodynamic changes in the skin layer quantitatively. The quantitative results about the influences of the anatomical and physiological changes in the superficial layers on the optical mapping images in this study will provide information for compensating the optical mapping images among different individuals and for different head regions in an individual.

1.5 Main contribution of the dissertation

The main contributions within the scope of this dissertation are as follows.

- A numerical model of a human head with variation in the uniform and nonuniform thickness of the skull and CSF layer is proposed to investigate the effect of spatially varying thickness of superficial layers on mapping images of brain activation. Light propagation in the head model is simulated by solving the photon diffusion equation using the FEM, and the optical mapping images are constructed from the simulated measurement data. The mapping images of activated region in the gray matter layer are also discussed with the varied number and position of the activated regions. This research work has been published in *Optical Review*, 17 (4), July, 2010, pp. 410-420.

- The influences of the existence of sagittal sinus in the CSF layer and the blood volume changes in the skin layer on optical mapping are studied by numerical simulations and phantom experiments. It is found that the increase in the blood volume in the skin layer increase the sensitivity of mapping images to the brain activity while the existence of the venous vasculature in the CSF layer decreases the sensitivity of the mapping images to the brain activity. A part of this research work has been presented in the *35th Annual International Conference of the IEEE Engineering in Medicine and Biology Society (IEEE EMBC2013), Osaka, Japan, 2013, pp. 2632-2635.*

1.6 Outline of the Dissertation

The content of the dissertation is outlined as follows.

Chapter 1 is an introduction to optical mapping with explaining its basic principles and problems. This chapter reviews fNIRS and other functional imaging modalities, discusses the present status of optical mapping, and refers to the differences in light propagation caused by the differences in the anatomy of the individual head. The last part of chapter 1 shows the aims and highlights of this study.

Chapter 2 explains propagation of NIR light in the head and the principle of optical mapping. A simulation method of optical mapping is proposed. Three-dimensional (3D) head models are constructed to calculate light propagation in the head by solving the photon diffusion equation using FEM. To further support the simulation method, phantom experiments are performed. Materials and a method of making tissue mimicking phantoms are reviewed. Finally, the measurement systems of optical mapping and its operation are explained.

Chapter 3 investigates the influences of spatial variations in the thickness of skull and CSF layers on optical mapping images of activated brain regions by numerical simulation of optical mapping. It is well known that the CSF layer with very weak absorption and scattering of light has a strong influence on light propagation. The

influences of spatial variations in the skull and CSF layer thicknesses on the mapping images are quantified and discussed for the cases of different positioning of an activated region in the probe array, and for the case of single and multiple activated regions. In addition, the light path probability distributions between one pair of source and detector are calculated to show the sensitivity of the mapping images to an activated region.

Chapter 4 is for the phantom experiments to investigate the influences of spatial variations of the skull and CSF layers on optical mapping. The method of making head phantoms are explained and the measurement procedure is described. The measurement reproducibility is discussed. The last part of this chapter shows the experimental results of optical mapping and comparisons with the simulation results.

Chapter 5 investigates the influences of anatomical and physiological changes in the superficial layer on optical mapping. Hemoglobin is the dominant chromophore in the near infrared wavelength range. Therefore, the influences of the existence of a sagittal sinus in the CSF layer and the blood volume changes in the skin layer on optical mapping are studied by numerical simulations. The results show that mapping images of an activated region in the gray matter layer are affected by the existence of blood vessels in the CSF layer and by the blood volume changes in the skin layer. The light path probability distributions are calculated to quantify the contribution of the superficial layer and deep layer to the measured light intensity. The influences on the mapping images are discussed for quantitative evaluation of the mapping images.

Chapter 6 shows the results of the phantom experiments to validate the simulation results on the influences of a thick blood vessel in the CSF layer and blood volume changes in the skin layer on optical mapping. A model of the skin layer including epidermis and dermis is used. The mapping images of the activated brain region depend on the size and absorption coefficient of the venous vasculature in the CSF layer. The absorption coefficient of the dermis affects the mapping images greatly. Thus, the experimental results demonstrate further support to the simulation results.

Chapter 7 presents general conclusions of the whole research and provides insights for future related work.

Chapter 2 Methods of numerical simulations and phantom experiments of optical mapping

2.1 NIR light propagation in the human head

2.1.1 Introduction

NIR light is defined as light with a wavelength range from about 700 nm to 1300 nm. Most biological tissues are relatively transparent to light in the NIR range between 700 nm and 900 nm because light in this region is less scattered than visible light and is weakly absorbed by only a few chromophores. NIR light illuminates the scalp and passes through the tissue with either being scattered or absorbed. Some of the photons of the incident light follow a banana-shaped path back to the surface of the scalp as shown in Fig. 2.1. This shape is slightly changed by the optical heterogeneity in the head, especially the low scattering subarachnoid space. Although a number of theoretical and experimental investigation on NIR light propagation in the human head

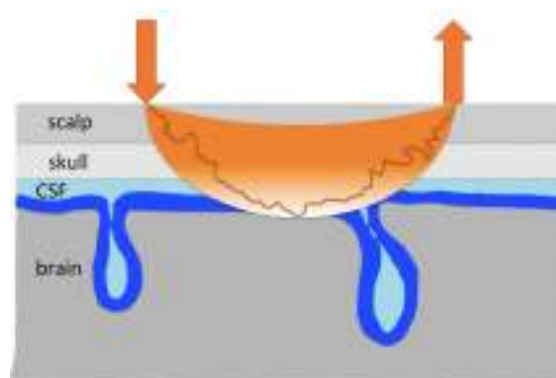


Fig. 2.1: A NIR light traveling through the head in a banana-shaped photon path.

have been performed, knowledge about which regions in the brain are sampled by NIR light is still incomplete. In optical mapping, the optical properties in each layer of the head are the key factors for prediction of light propagation.

2.1.2 Absorption and scattering of light in the human head

To understand light propagation in the human head and interaction of light with the tissues, the optical properties of the tissues are necessary, which are primarily described in terms of the absorption and scattering coefficients. Both of them are dependent on the wavelength of light and tissue types.

- Absorption coefficient

The absorption coefficient μ_a is defined as the probability of photon being absorbed per unit length. Fig. 2.2(a) shows the attenuation of light through a non-scattering medium. If light with the intensity of I_0 and wavelength of λ passes through a non-scattering medium with thickness of d , the intensity of the emerging light is given as

$$I = I_0 e^{-\mu_a(\lambda)d} \quad (2.1)$$

The absorption coefficient of a medium may be due to a number of absorbing substances (chromophores) mixed together. The value of μ_a of the medium containing a variety of chromophores is expressed as the sum of the products of the concentration of each chromophores, C , with its molar extinction coefficient, ε [40],

$$\mu_a(\lambda) = \sum C\varepsilon(\lambda) \quad (2.2)$$

NIR light passing through the human head is absorbed by some biological chromophores, such as hemoglobin, myoglobin, and cytochrome oxidase. NIRS focuses on hemoglobin, because myoglobin and cytochrome oxidase are much less changeable in the context of mapping brain activity. Hemoglobin is the oxygen carrier in red blood cells which deliver oxygen to tissues by attaching to oxygen in the lung to become oxy-hemoglobin, HbO_2 , then by releasing oxygen in tissues to become

deoxy-hemoglobin, Hb.

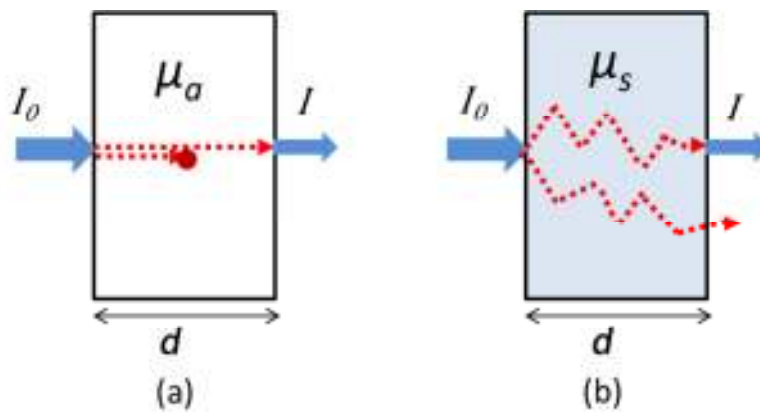


Fig. 2.2: (a) Attenuation of light through a non-scattering medium. (b) Attenuation of light through a scattering medium.

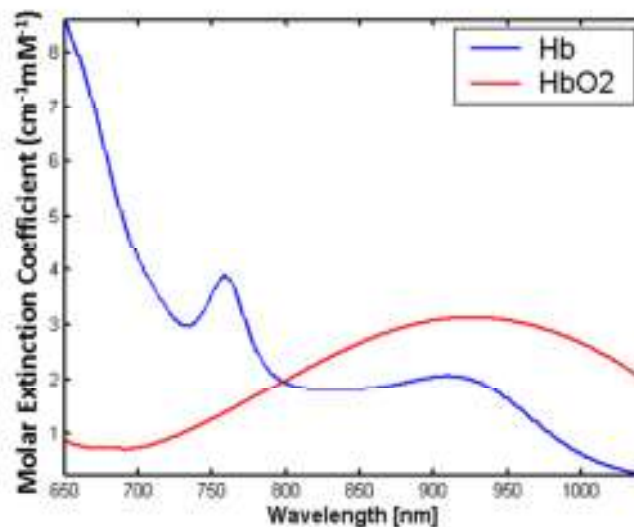


Fig. 2.3: Absorption spectra of oxy-Hb and deoxy-Hb.

Figure 2.3 shows the difference in the absorption spectrum between HbO₂ and Hb in the NIR wavelength range. Optical mapping is based on the fact that the spectrum of hemoglobin in the NIR region varies with its oxygenation state.

- Scattering coefficient

Biological tissues are optically inhomogeneous from the view point that the

distribution of the refractive index is inhomogeneous in the tissues. When light is incident on a medium containing particles with different refractive index of the medium, scattering will occur when light hits the particles. The scattering coefficient, μ_s , is defined as the probability of a photon being scattered per unit length, which is determined by the refractive index of the two materials and the size and shape of the scatterer. Figure 2.2(b) shows the attenuation of light through a scattering medium. Due to scattering, the emerging photons are detected at any position of the medium surface. Scattering of light in the human head is complex because the head consists of layers with different optical properties as illustrated in Fig. 2.1. As a consequence of the complex light scattering by different tissue layers, the length of light passing through the head (the effective optical pathlength) is longer than the physical distance between the source and detector.

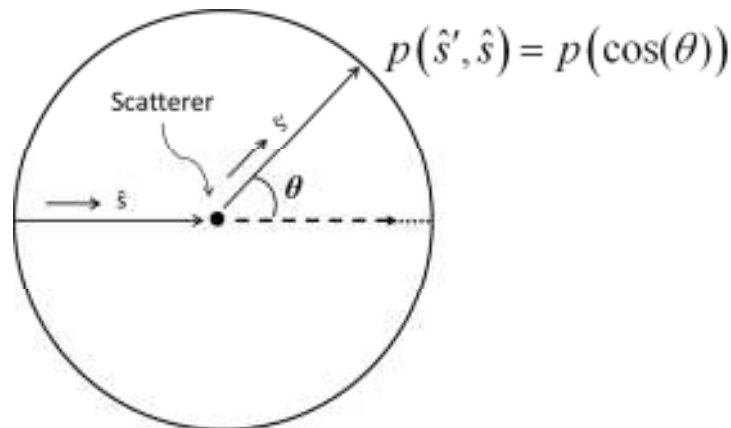


Fig. 2.4: Scattering phase function. The incident light travels in the \hat{s} direction and the scattered photon exits in the \hat{s}' direction.

In every scattering event, the angular distribution of the scattered light relative to the incident light is described by a scattering phase function, p (Fig. 2.4).

The phase function, p , is a function of the angle between the incident and scattered light and depends only on the scalar product of \hat{s}' and \hat{s} . The scattering coefficient, μ_s , is a function of the number density of the scatters. The anisotropy factor of scattering, g , is given by the mean cosine of the phase function, p ,

$$g = \int_{4\pi} p(\cos \theta) \cos \theta d\hat{s}' \quad (2.3)$$

The scattering properties of medium are often described in terms of the reduced scattering coefficient μ'_s which is given by

$$\mu'_s = \mu_s (1 - g) \quad (2.4)$$

If $g = 0$ then the scattering is isotropic, and if $g = 1$, the scattering is entirely forward directed. Biological tissues reveal strongly forward directed scattering with $g = 0.8 \sim 0.95$ [41].

2.1.3 Modeling of light propagation in tissues

NIR light propagation in thick biological tissues can be described by the diffusion approximation to the radiative transfer equation. The fundamental equation describing light propagation in absorbing and scattering media like tissues is the time-dependent Boltzmann transport equation (or radiative transfer equation) expressed by

$$\left\{ \frac{1}{c} \frac{\partial}{\partial t} + \hat{s} \nabla + (\mu_s + \mu_a) \right\} I(r, \hat{s}, t) = \mu_s \int_{4\pi} p(\hat{s}', \hat{s}) I(r, \hat{s}', t) d\hat{s}' + q(r, \hat{s}, t) \quad (2.5)$$

where c is the speed of light in the medium, $I(r, \hat{s}, t)$ is the radiance at position r and time t , propagating in the direction \hat{s} . The phase function $p(\hat{s}', \hat{s})$ is the probability of scattering from direction \hat{s}' to \hat{s} and satisfies the following normalization, eqn. (2.6),

$$\int_{4\pi} p(\hat{s}', \hat{s}) d\hat{s}' = 1 \quad (2.6)$$

$q(r, \hat{s}, t)$ is the light power injected per unit volume at position r in the direction \hat{s} and at time t . Now the following quantities are defined for the diffusion approximation,

Photon fluence rate

$$\phi(\mathbf{r}, t) = \int_{4\pi} I(r, \hat{s}, t) d\hat{s} \quad (2.7)$$

Photon flux

$$J(r, t) = \int_{4\pi} \hat{s} I(r, \hat{s}, t) d\hat{s} \quad (2.8)$$

Integrated source function

$$q_0(r, t) = \int_{4\pi} q(r, \hat{s}, t) d\hat{s} \quad (2.9)$$

The P_N approximation expands the variables I , q and p in spherical harmonics, and the first order P_1 approximation converts the radiative transfer equation into a simpler time-dependent partial differential equation,

$$\frac{1}{c} \frac{\partial \phi(r, t)}{\partial t} = \nabla \cdot D(r) \nabla \phi(r, t) - \mu_a \phi(r, t) + q_0(r, t) \quad (2.10)$$

Here, the photon flux is related to the photon fluence rate by

$$J(r, t) = -D(r) \nabla \phi(r, t) \quad (2.11)$$

and D is the diffusion coefficient expressed by

$$D(r) = \frac{1}{3\mu'_s(r)} = \frac{1}{3(1-g)\mu_s(r)} \quad (2.12)$$

In the P_1 approximation, the source term is assumed to be isotropic. Equation (2.12) is justified by assuming $\mu_a \ll \mu'_s$ [42, 32]. Equation (2.10) is called the photon diffusion equation which is valid after a number of scattering events, and is believed to hold for biological tissues thicker than a few millimeters.

2.2 Theory of optical mapping

Optical mapping provides 2-dimensional images of brain activation along the head surface using a CW multi-channel NIR system. It's based on the fact that activation of brain induces the change in the hemoglobin concentration and then results in the change in optical absorption. It is well known that the functional state of the tissues influences the optical properties of the tissues. During brain activity, the local cerebral blood flow (CBF) and cerebral blood volume (CBV) increase with the increased glucose and oxygen consumption in the local capillary bed, a mechanism known as neurovascular coupling. Fig. 2.5 displays the changes in the concentrations of HbO₂, Hb and total-Hb (= HbO₂ + Hb) in a typical fNIRS measurement during brain activation [43]. The increase in the concentration of HbO₂ and decrease in the concentration of Hb reflect the increase in CBF and the concentration of total-Hb.

Optical mapping uses the characteristics of the absorption spectra of HbO₂ and Hb in the NIR range (see Fig. 2.3). To measure the hemoglobin concentration changes by brain activation, many source and detector fibers are attached on the head surface and the scattered light passing through the scalp, skull and brain is picked up by the multiple pairs of source and detector fibers. As shown in Fig. 2.6, the head is modeled to consist of five layers, skin, skull, CSF, gray and white matter layers. When the brain shifts from a rest state to an activated state, an activated region is assumed existing in the gray matter layer.

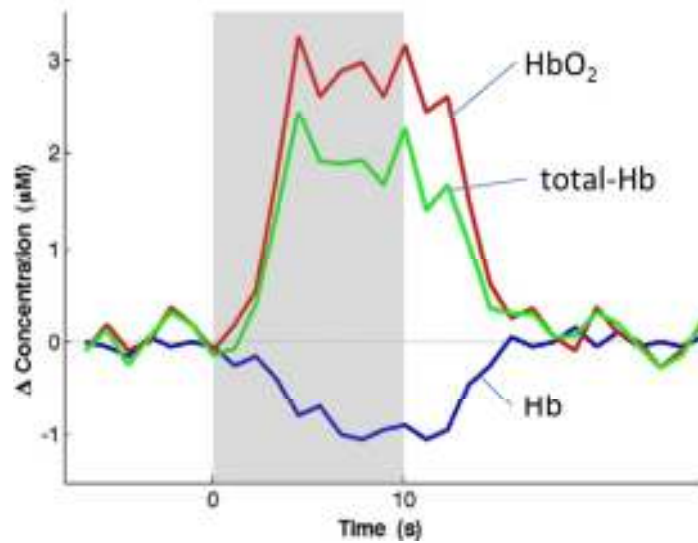


Fig. 2.5: The changes in the concentrations of HbO₂, Hb and total-Hb in a typical fNIRS measurement for brain activation. The shadow area indicates the stimulus duration.

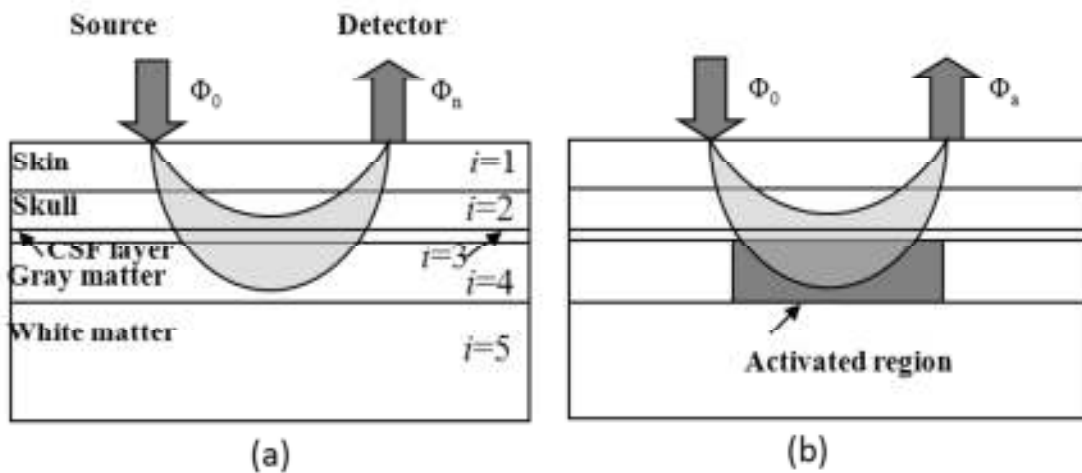


Fig. 2.6: (a) rest state, and (b) activated state with an activated region in the gray matter.

To obtain the absorption change in the brain, the change in the intensity of the detected light is measured. Source light with the wavelength of λ irradiates a head surface and is detected at the distance of about 30mm from the source position. The optical density, $OD(\lambda)$, is defined by,

$$OD(\lambda) = -\ln \frac{\Phi(\lambda)}{\Phi_0(\lambda)} \quad (2.13)$$

where $\Phi_0(\lambda)$ and $\Phi(\lambda)$ are the source and detected light intensities, respectively. Based on the modified Beer-Lambert law, $OD(\lambda)$ is related to the concentration changes in the chromophores in a single homogeneous layer as,

$$OD(\lambda) = -\ln \frac{\Phi(\lambda)}{\Phi_0(\lambda)} = \sum_k \varepsilon_k(\lambda) C_k l + S \quad (2.14)$$

where $\varepsilon_k(\lambda)$ is the molar extinction coefficient of the k -th chromophore [$\text{mm}^{-1}\text{mM}^{-1}$], C_k is the molar concentration of the k -th chromophore [mM], l is the effective pathlength in the layer [mm], S denotes optical attenuation mainly due to scattering. The major chromophores in the brain are oxy- and deoxy-hemoglobin. Thus, $OD(\lambda)$ is expressed as,

$$OD(\lambda) = -\ln \frac{\Phi(\lambda)}{\Phi_0(\lambda)} = \sum_k \varepsilon_k(\lambda) C_k l + S = \{ \varepsilon_{HbO_2}(\lambda) C_{HbO_2} + \varepsilon_{Hb}(\lambda) C_{Hb} \} l + S \quad (2.15)$$

where subscripts “ Hb ” and “ HbO_2 ” denote oxy- and deoxy-hemoglobin, respectively. Optical mapping uses the measured data of the differences in the OD between the activated and rest states of brain, $\Delta OD(\lambda)$. OD s at the rest and activated states are given by the sum of OD s for multiple layers in the head as,

·Rest state

$$OD^n(\lambda) = -\ln \frac{\Phi^n(\lambda)}{\Phi_0(\lambda)} = \sum_{i=1}^5 \left[\{ \varepsilon_{HbO_2}(\lambda) C_{HbO_2}^n + \varepsilon_{Hb} C_{Hbi}^n \} l_i + S_i \right] \quad (2.16)$$

·Activated state

(2.17)

$$OD^a(\lambda) = -\ln \frac{\Phi^a(\lambda)}{\Phi_0(\lambda)} = \sum_{i=1}^5 \left[\left\{ \varepsilon_{HbO_2}(\lambda) C_{HbO_2i}^a + \varepsilon_{Hb} C_{Hbi}^a \right\} l_i + S_i \right]$$

where $\Phi(\lambda)$ is the detected light intensity, i is the number of the layers from 1 to 5 corresponding to Fig. 2.6(a), and the superscripts “ n ” and “ a ” indicate the rest and activated states, respectively. Here, each layer is assumed to be homogeneous. Even when the brain condition changes from the rest to activated states, S_i can be considered to be constant. Then, $\Delta OD(\lambda)$ is given by the following,

·Difference between the activated and rest states

$$\begin{aligned} \Delta OD(\lambda) &= OD^a(\lambda) - OD^n(\lambda) = -\ln \frac{\Phi^a(\lambda)}{\Phi^n(\lambda)} \\ &= \sum_{i=1}^5 \left\{ \varepsilon_{HbO_2}(\lambda) (C_{HbO_2i}^a - C_{HbO_2i}^n) + \varepsilon_{Hb}(\lambda) (C_{Hbi}^a - C_{Hbi}^n) \right\} l_i \\ &= \sum_{i=1}^5 \left\{ \varepsilon_{HbO_2}(\lambda) \cdot \Delta C_{HbO_2i} \cdot l_i + \varepsilon_{Hb}(\lambda) \cdot \Delta C_{Hbi} \cdot l_i \right\} \end{aligned} \quad (2.18)$$

The measured mapping data, $\Delta OD(\lambda)$, are the sum of the products of the molar extinction coefficient, the change in the concentration and the optical pathlength in the five layers.

In general, because NIR light is strongly scattered by biological tissues and the structure of head differs by individuals, it is difficult to determine the effective path length of each layer, l_i . In the process of generating images, optical mapping assumes that brain activation occurs only in the gray matter ($i = 4$ as shown in Fig. 2.6) resulting in the hemoglobin concentration changes only in the gray matter too. Therefore, Eq. (2.18) reduces to Eq. (2.19) with retaining the term of $i = 4$ only,

$$\Delta OD(\lambda) = -\ln \frac{\Phi^a(\lambda)}{\Phi^n(\lambda)} = \varepsilon_{HbO_2}(\lambda) \cdot \Delta C_{HbO_2,4} \cdot l_4 + \varepsilon_{Hb}(\lambda) \cdot \Delta C_{Hb,4} \cdot l_4, \quad (2.19)$$

where l_4 is the path length in the gray matter, so-called the partial pathlength.

In optical mapping, measurements of $\Delta OD(\lambda)$ are made at two wavelengths of $\lambda =$

λ_1 and λ_2 , and the values of $\Delta C_{HbO_2} \cdot l_4$ and $\Delta C_{Hb} \cdot l_4$ are obtained by solving the two simultaneous equations of (2.19) for λ_1 and λ_2 ,

$$\Delta C_{HbO_2} \cdot l_4 = \frac{\varepsilon_{Hb}(\lambda_2)\Delta OD(\lambda_1) - \varepsilon_{Hb}(\lambda_1)\Delta OD(\lambda_2)}{\varepsilon_{Hb}(\lambda_2)\varepsilon_{HbO_2}(\lambda_1) - \varepsilon_{Hb}(\lambda_1)\varepsilon_{HbO_2}(\lambda_2)}, \quad (2.20)$$

$$\Delta C_{Hb} \cdot l_4 = \frac{\varepsilon_{HbO_2}(\lambda_2)\Delta OD(\lambda_1) - \varepsilon_{HbO_2}(\lambda_1)\Delta OD(\lambda_2)}{\varepsilon_{Hb}(\lambda_1)\varepsilon_{HbO_2}(\lambda_2) - \varepsilon_{Hb}(\lambda_2)\varepsilon_{HbO_2}(\lambda_1)}. \quad (2.21)$$

Because the molar extinction coefficients are known as shown in Fig. 2.3 and ΔOD s are obtained by measurements, these values of $\Delta C_{HbO_2} \cdot l_4$, $\Delta C_{Hb} \cdot l_4$ and $\Delta C_{Hbt} \cdot l_4$ ($=\Delta C_{HbO_2} \cdot l_4 + \Delta C_{Hb} \cdot l_4$) are calculated and allocated at the midpoints between the neighboring source and detector positions which are called the data points.

If light with a single wavelength of $\lambda_3 = 805$ nm which is the isobestic point of the absorption spectra of *Hb* and *HbO₂* (i.e., $\varepsilon_{HbO_2}(\lambda_3) = \varepsilon_{Hb}(\lambda_3)$) is used, the changes in the total-Hb concentration are given simply as the following,

$$\Delta C_{Hbt} \cdot l_4 = \frac{\Delta OD(\lambda_3)}{\varepsilon_{Hb}(\lambda_3)}. \quad (2.22)$$

This study assumes the use of light only at this wavelength of the isobestic point for simplicity, and obtains mapping images of $\Delta OD(\lambda_3) = \Delta C_{Hbt} \cdot l_4 \cdot \varepsilon_{Hb}(\lambda_3)$ instead of $\Delta C_{Hbt} \cdot l_4$ as usually done in optical mapping. ΔOD s are obtained by employing an array of light sources and detectors, and ΔOD values allocated at the data points are used to construct 2-D mapping images by spline interpolation [44].

2.3 Simulation of optical mapping

2.3.1 Modeling of optical mapping

The arrangement of the source and detector probes in the simulation is shown in Fig. 2.7. Sixteen probes with eight sources and eight detectors are used. The separation of each source-detector pair is fixed at 30mm. The whole area where the probes cover is the square of 90 mm by 90 mm. A total of 24 data points are allocated at the middle points between the neighboring sources and detectors. The area of simulation of light propagation is 150 mm by 150 mm as the result of 30 mm extension at all sides of the area that the probes cover. Both the source and detector have the same diameter of 1 mm at the contact points to the head surface.

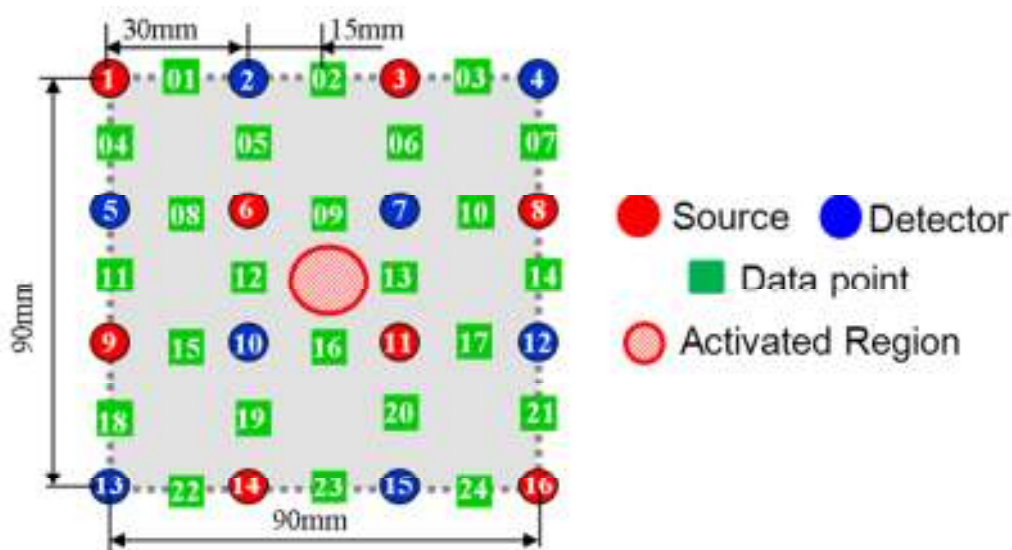


Fig. 2.7: Arrangement of the sources, detectors, data points and activated region.

Simulation of optical mapping is performed as the following. First, a light source is injected at one source position for the two states of brain at rest (without an activated region) and at activation (with an activated region). Then the light intensities at the detectors neighboring to the source position for the two states (Φ^r , Φ^a) are calculated by

solving the photon diffusion equation as mentioned later. ΔOD s are calculated by Eq. (2.19) from the detected intensities (Φ^n , Φ^a) and then put at the data points which are the midpoints between the source and detector positions. This process is repeated for all eight source positions, and the values of ΔOD at all the 24 data points are given. Finally, an image of ΔOD reflecting the activated region is constructed by the spline interpolation of the 24 ΔOD data at the 24 data points.

2.3.2 Modeling of light propagation

There are two categories of simulation methods of light propagation, statistical and deterministic methods. A Monte Carlo method [45] is an example of the former. The disadvantage of Monte Carlo methods is time-consuming, and it is impractical to employ a Monte Carlo method for the case of optically thick media. One of the deterministic methods is to solve the equation of radiative transfer which is the strict representation of light propagation in scattering and absorbing media like biological tissues [46, 47]. However, it is not easy to solve the equation of radiative transfer even by numerical methods, and the photon diffusion equation which is the approximation (P1 approximation) of the equation of radiative transfer by expanding the intensity in a series of spherical harmonics (see Chap 2.1.3).

In the time-dependent photon diffusion equation (2.10), the term of time derivative vanishes for CW light which is used in optical mapping. In addition, no light source is assumed inside the medium, so the source term also vanishes. Therefore, CW light propagation is described by the steady state photon diffusion equation,

$$\nabla[D(r)\nabla\phi(r)] - \mu_a(r)\phi(r) = 0 \quad (2.23)$$

where r is the position vector, ϕ is the fluence rate, $D = 1/(3\mu_s')$ is the diffusion coefficient, μ_s' and μ_a are the reduced scattering and absorption coefficients, respectively.

The photon diffusion equation is applicable not only to homogeneous media but

also to layered media by specifying the optical properties (μ_s' and μ_a) of each layer. Applicability of the photon diffusion equation to the low-scattering CSF layer has been discussed. Koyama *et al.* [48] have reported that the reduced scattering coefficient of the CSF layer had the value of about $\mu_s' = 0.3 \text{ mm}^{-1}$ which was estimated from the time-resolved measurement for adult human heads, and have concluded that the photon diffusion equation can be applied to the CSF layer having μ_s' of about 0.3 mm^{-1} and greater. Therefore, in this study the reduced scattering coefficient of the CSF layer is assumed to be 0.3 mm^{-1} which satisfies the condition of application of the photon diffusion equation to the CSF layer.

- **Boundary conditions**

Then, Eq. (2.23) is solved for ϕ under the appropriate boundary conditions at the surface of the model as follows,

$$\phi = -2DA \frac{\partial \phi}{\partial n} \text{ : except the source position,} \quad (2.24)$$

$$\phi = -2DA \frac{\partial \phi}{\partial n} + \frac{4}{1-r_d} I_0 \text{ : source position,} \quad (2.25)$$

where n indicates the direction outward normal to the surface, I_0 is the source intensity which is given as unity in the simulation, parameter A is defined by $A = (1+r_d)/(1-r_d)$, where r_d is the internal reflectivity at the surface and determined using the relative refractive index n_r by[49]

$$r_d = -1.440n_r^{-2} + 0.710n_r^{-1} + 0.668 + 0.0636n_r \quad (2.26)$$

The boundary condition at the interface between the adjacent layers i and $i+1$ is given by

$$-D_i \frac{\partial \phi}{\partial n_i} = -D_{i+1} \frac{\partial \phi}{\partial n_{i+1}} \quad (2.27)$$

where the flux of ϕ perpendicular to the interface is assumed to be equal at the both layers of the interface. The measured intensity Φ at the head surface is given as the flux of ϕ outgoing from the surface as

$$\Phi = -D_1 \left(\frac{\partial \phi}{\partial n_1} \right) : \text{at surface, } z = 0. \quad (2.28)$$

- Light path probability distribution

To show the path of light propagation, the path probability distribution between the source and detector positions, $\psi(r)$, is calculated by[50]

$$\psi(r) = \phi_s(r) \phi_d(r) / I_0^2 \quad (2.29)$$

where $\phi_s(r)$ and $\phi_d(r)$ are the fluence rates at the position r when the light is incident at the source and detector positions, respectively. I_0 is the incident light intensity.

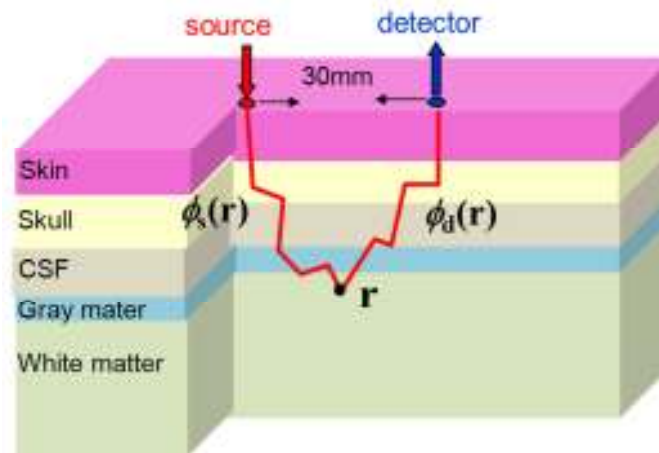


Fig. 2.8: The light path probability of light detected after passing through the position r . $\phi_s(r)$ is the fluence rate at the position r for light injected at the source position. $\phi_d(r)$ is the fluence rate at the position r for light injected at the detector position.

In this study, solving Eq. (2.23) for ϕ under the boundary conditions of Eqs. (2.24), (2.25) provides Φ and $\psi(r)$ in Eqs. (2.28) and (2.29), respectively. A commercially available software (COMSOL Multiphysics, COMSOL Inc.) was used to solve Eq. (2.23) by the finite element method (FEM), which is frequently used to solve partial differential equations, like the photon diffusion equation, in complex geometries. The numerical solutions calculated by FEM in homogeneous medium have been shown to agree well with the analytical solution [51]. Therefore, the reliability of the numerical solutions in this study has been verified.

2.4 Phantom experiments

2.4.1 Materials and methods of manufacturing tissue mimicking phantoms

The phantoms were made of epoxy resin mixed with titanium oxide (TiO_2) particles and black ink to adjust the reduced scattering and absorption coefficients of the phantoms. Epoxy resin was used as a base material which was made by mixing the primary resin and hardener (Buehler Ltd) with the mixing ratio of 8:1 by weight. TiO_2 particles (diameter: $0.35\mu\text{m}$, index of refraction: 2.71, Titan. Kogyo. Ltd) were used as a scattering material. A black ink for plastic (Altechno. Ltd) was mixed to control the absorption coefficient of the tissue mimicking phantom. Using these materials, phantoms with the desired optical properties were manufactured.

2.4.2 Measurement of the optical properties of the phantom

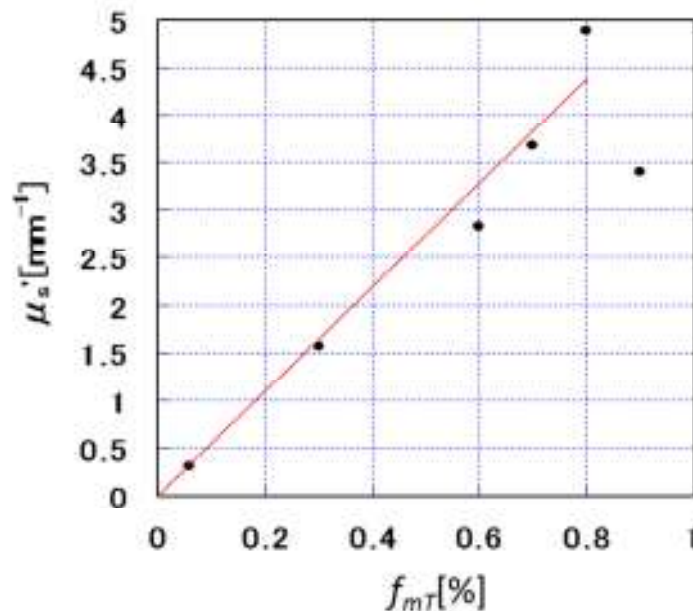
It is assumed that the values of μ_s' and μ_a of the phantoms are proportional to mass fractions of the TiO_2 particles and black ink, respectively. Therefore, the values of μ_s' of the epoxy resin containing the TiO_2 particles and the values of μ_a of the epoxy resin containing the black ink were measured to calibrate the relations of their mass fractions,

f_{mT} , f_{mI} , and the optical properties, μ_s' and μ_a .

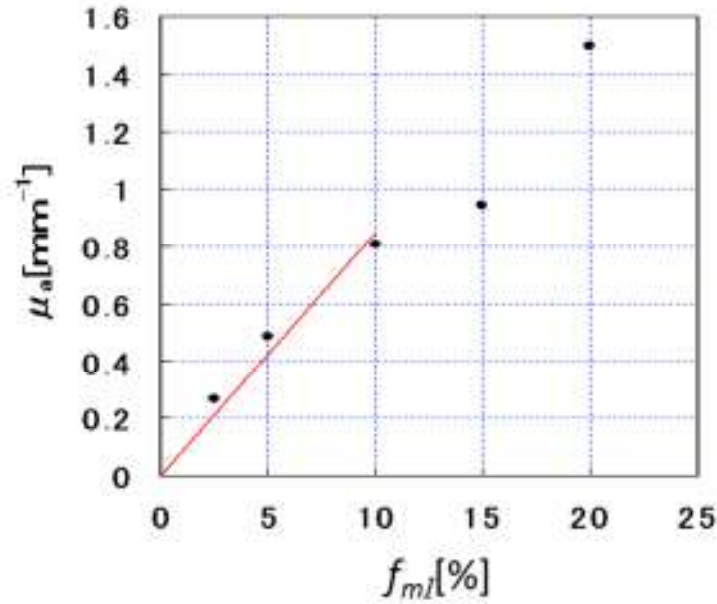
Two kinds of samples for measurement of the optical properties were prepared. First kind of sample was the epoxy resin containing only TiO_2 particles for measuring μ_s' . Six different samples with the TiO_2 mass fractions of $f_{mT} = 0.06\%$, 0.3% , 0.6% , 0.7% , 0.8% and 0.9% were prepared.

Second kind of sample was the epoxy resin containing only black dye for measuring μ_a . Five different samples with the black ink mass fractions of $f_{mI} = 2.5\%$, 5.0% , 10% , 15% and 20% were prepared. All samples had a form of disk with a diameter of 45 mm and a thickness of 2 mm.

As for the measurement of μ_s' , a spectrophotometer with an integrating sphere (UV-3150, Shimadzu Corporation) was used to measure the transmittances and reflectances of light after multiple scattering in the samples. Then, the values of μ_s' were determined so that the transmittances and reflectances calculated by a Monte Carlo simulation agreed with those obtained by measurements.



(a)



(b)

Fig. 2.9: Calibration results of the optical properties. (a) μ_s' of the epoxy resin as a function of the mass fractions of the TiO_2 particles, f_{mT} , and (b) μ_a of the epoxy resin as a function of the mass fractions of the black ink, f_{ml} .

The values of μ_a of the samples were determined from the measured transmittances simply using the Beer-Lambert law because the epoxy resin samples containing only the black ink did not scatter light. All measurements were done at the wavelength of 805 nm at the isobestic point.

Figure 2.9 (a) shows the values of μ_s' of the epoxy resin as a function of the mass fraction of the TiO_2 particles, f_{mT} , and (b) shows the values of μ_a of the epoxy resin as a function of the mass fraction of the black ink, f_{ml} . Red regression lines are drawn which are proportional to the mass fractions of f_{mT} and f_{ml} . Using these regression lines, phantoms were manufactured to have the desired optical properties.

2.4.3 Design of the phantom

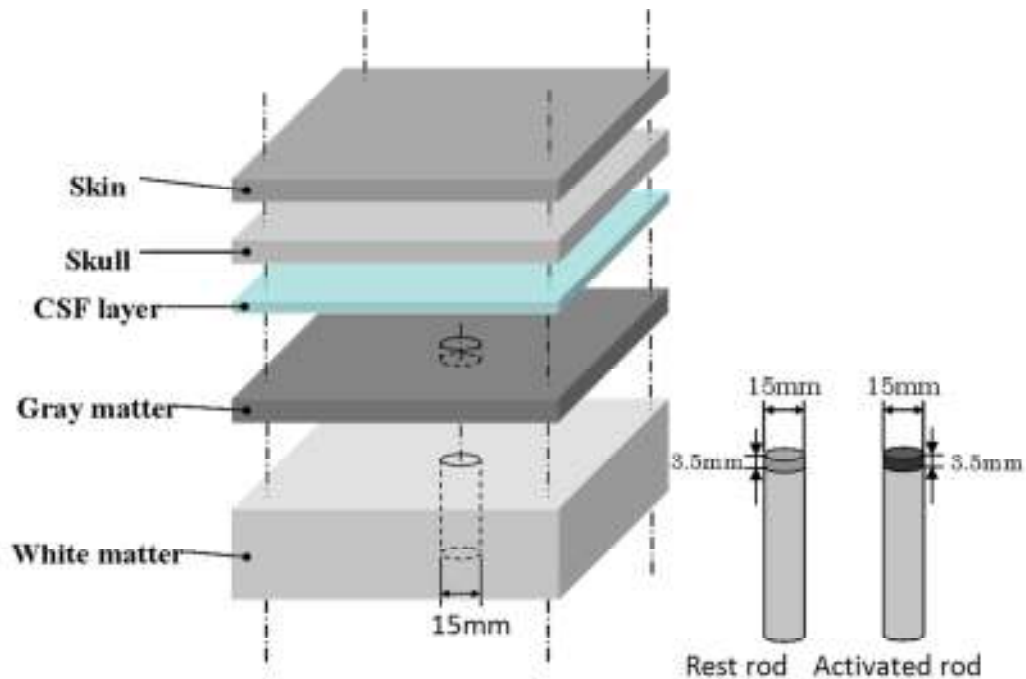


Fig. 2.10: Design of five-layered phantom with rest rod and activated rod.

Figure 2.10 show the structure of the phantoms used in this study. To simulate the adult head, five-layer models were constructed which consisted of skin, skull, CSF, gray matter and white matter layers. In addition, cylindrical cavities in the gray matter and white matter layers were opened for inserting rods simulating the rest or activated state of the brain. The diameters of the rods were 15 mm.

The thickness of the whole head model was fixed as 50 mm. The thickness of the gray matter was changed according to the specified variation in the thicknesses of the skull and CSF layers. The thickness of the white matter layer at the bottom was greater than 30 mm which was large enough to ensure that light was scattered back to the surface without escaping from the bottom surface.

The optical properties of the five layers at the wavelength of 805 nm were

determined by referencing literatures as listed in Table 2.1 [52-55]. The values of μ_s' of the activated region were assumed to remain the same as that of the gray matter, while the values of μ_a of the activated region were assumed to increase by about 50% due to the increased blood volume.

Table 2.1 The optical properties of the head models (805nm)

Tissue type	μ_a (mm ⁻¹)	μ_s' (mm ⁻¹)
skin	0.03	0.73
skull	0.012	1.8
CSF	0.002	0.3
Gray matter	0.036	2.3
White matter	0.014	4.4
Activated region	0.052	2.3

2.4.4 Measuring system for optical mapping

A multi-channel CW NIRS imaging system (FOIRE-3000: Shimadzu Corporation) as shown in Fig. 2.11 was used in the experiment to obtain optical mapping images. Table 2.2 shows the specifications of FOIRE-3000. Figure 2.11(a) is the photo of the system, and Fig. 2.11(b) shows the block diagram of the system configuration.

Based on the principle described in Sec. 2.2, the system can image the relative changes in the concentrations of oxy-Hb, deoxy-Hb and total-Hb multiplied by the effective optical pathlength two-dimensionally along the head surface. Three wavelengths of 780 nm, 805 nm and 830 nm were used to improve the S/N ratio of the obtained concentrations. The system used eight sets of three laser diodes for light sources which were temporally multiplexed. Eight photomultipliers were employed to detect the signals continuously in parallel.

The arrangement of the probes is shown in Fig. 2.7. There are 24 data points for the arrangement of 8 sources and 8 detectors, and 24 measured values of $\Delta OD(\lambda)$ are put

at the 24 data points. The optical mapping image is constructed by 2-D spline interpolation of ΔODs at the 24 data points.

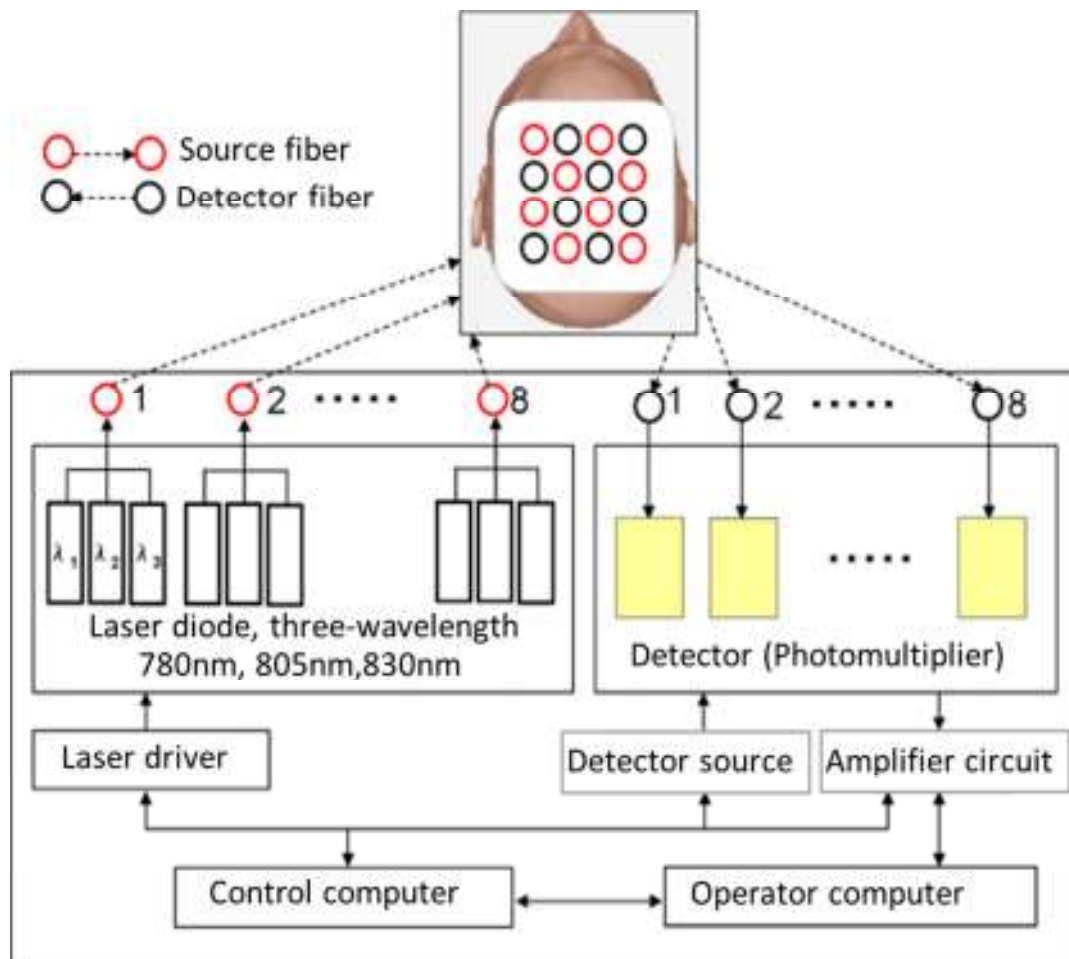
Figure 2.12 shows the side view of the phantom experimental setup. The probe holder and five phantom layers (six layers when the skin layer was divided into epidermis and dermis layers) were tightly fixed at the four corners with screws to keep good contacts between the neighboring layers. The white matter layer was set on the top to make the exchange of the rest and activated rods easy.

Table 2.2 FOIRE-3000 Specifications

Wavelengths of source light	780 nm, 805 nm and 830 nm
Light sources	Three near-infrared semiconductor laser diodes of 3 wavelength (Class 1M, IEC60825-1), (1.5mW~7.2mW) light intensity depends on the illumination time.
Number of sources	8
Light detectors	Multi-alkali photomultipliers
Number of detectors	8
Optical glassfibers	Multicomponent glass bundle fiber
Source-detector fiber pairs	8 sets



(a)



(b)

Fig. 2.11: NIRS imaging system (FOIRE-3000) and block diagram of the system configuration.

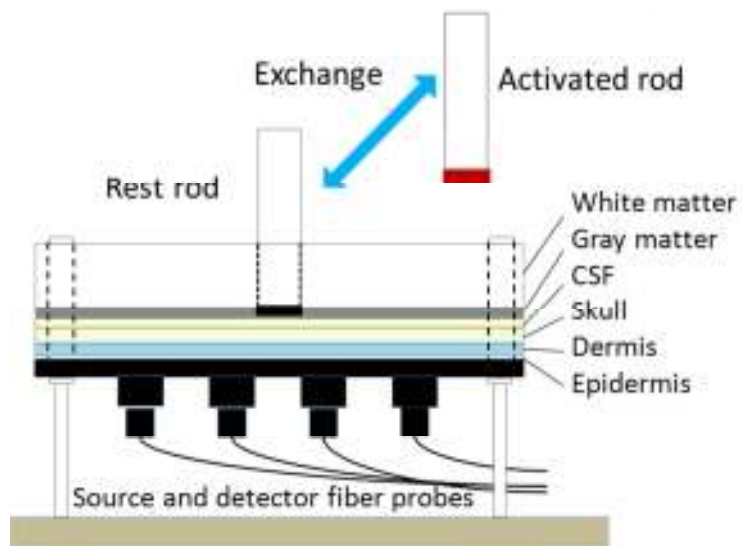


Fig. 2.12: Side view of the phantom experimental setup.

Chapter 3 Effects of Spatial Variations of Skull and Cerebrospinal Fluid Layers on Optical Mapping of Brain Activities: Numerical Study

3.1 Introduction

Light propagation and the optical pathlength inside the head are highly dependent on the head structure, and resultantly the optical mapping images are influenced by the head structure. The thicknesses of the superficial layers in the head vary with different regions and individuals. The thickness of skull varies from 4mm~10mm for adult and the thickness of the CSF layer is 1 mm ~ 3 mm. Particularly, the CSF layer has the optical properties of low absorption and low scattering which are very different from other tissues, and it has been reported that the existence of the CSF layer has a strong effect on light propagation in the brain [56-58].

A few previous studies have studied the effects of the thickness of superficial layers on NIRS signals. Okada et al. [59] reported the effects of the uniformly varying thickness of the skull and CSF layers on the NIRS signal sensitivity with Monte Carlo (MC) simulations for a 5-layered slab model. Their results suggested that at a source-detector spacing of 30 mm, the optical pathlength in the brain decreased as the skull thickness increased; however, the optical pathlength in the brain hardly depended on the thickness of the CSF layer. More recently, Strangman et al. [60] investigated the contributions of the regional variation of the scalp and skull thicknesses to the NIRS brain sensitivity for a more sophisticated MRI head model using MC simulations. At the source-detector separation of 30 mm, thicker layers of the scalp and skull decrease the relative NIRS sensitivity to the brain tissue. A similar problem is known to exist in the

brain activation mapping by EEG. For brain mapping by EEG, the effect of the inhomogeneity of the skull layer has been investigated [61].

However, to our knowledge, no investigation has reported the effects of the spatial variations of the superficial layer thickness on the optical mapping images. Also, the cases with multiple activated-regions in the brain under the spatially varying thicknesses of the superficial layers have not been studied. To study these effects, three-dimensional head models are constructed to calculate light propagation in a five-layer model: skin, skull, CSF, gray matter and white matter layers. Light propagation in tissues is calculated by solving the steady-state photon diffusion equation under appropriate boundary conditions. The light path probability distributions between one pair of source and detector are calculated to show the sensitivity of the mapping images to the activated region.

As the results, the distributions of ΔOD of an activated region to the mapping image in the tissue volume interrogated by a pair of source and detector are obtained. The effect of the thickness of the CSF layer on the mapping image is found to be opposite to that of the skull layer. The effects of spatial variation of the skull and CSF layer thicknesses on the mapping images are shown and discussed for the single and multiple activated regions.

3.2 Model of human head for optical mapping

The simulation model of a human head for optical mapping is shown in Fig. 3.1 with the x - y - z coordinate. The head model consists of five layers, skin, skull, CSF, gray matter and white matter layers. In this study the thicknesses of the skin and gray matter layers are fixed to be 5 mm and 3.5 mm, respectively, and the effects of the spatial variation in the thicknesses of the skull and CFS layers on the mapping images are investigated. The thickness of the skull layer is varied as the following five cases; i.e., uniform thickness of 5 mm (Case S1), 10 mm (Case S2), 20 mm (Case S3), and linearly varying thickness in the x -direction of the simulation area from 5 mm to 10 mm (Case

S4), and from 5 mm to 20 mm (Case S5) with the unchanged CSF thickness of 3 mm. Likewise, the CSF layer is varied as no CSF layer (Case C0), uniform thickness of 1 mm (Case C1), 3 mm (Case C2), 6 mm (Case C3), and linearly varying thickness in the x -direction of the simulation area from 1 mm to 3 mm (Case C4), and from 1 mm to 6 mm (Case C5) with the unchanged skull thickness of 5 mm. These variations of the thicknesses of the skull and CSF layers are given by referring literatures which indicate the variations of humans. For example, the skull thickness varies from about 5 mm at forehead to about 20 mm at inion for standard human adults [62], and the thickness of the CSF layer of subarachnoid space consisting of some membranes ranges from 1 mm to 6 mm for humans [48]. The depth of the whole head model is fixed as 50 mm, and the thickness of the white matter layer is changed according to the variations in the thicknesses of the skull and CSF layers.

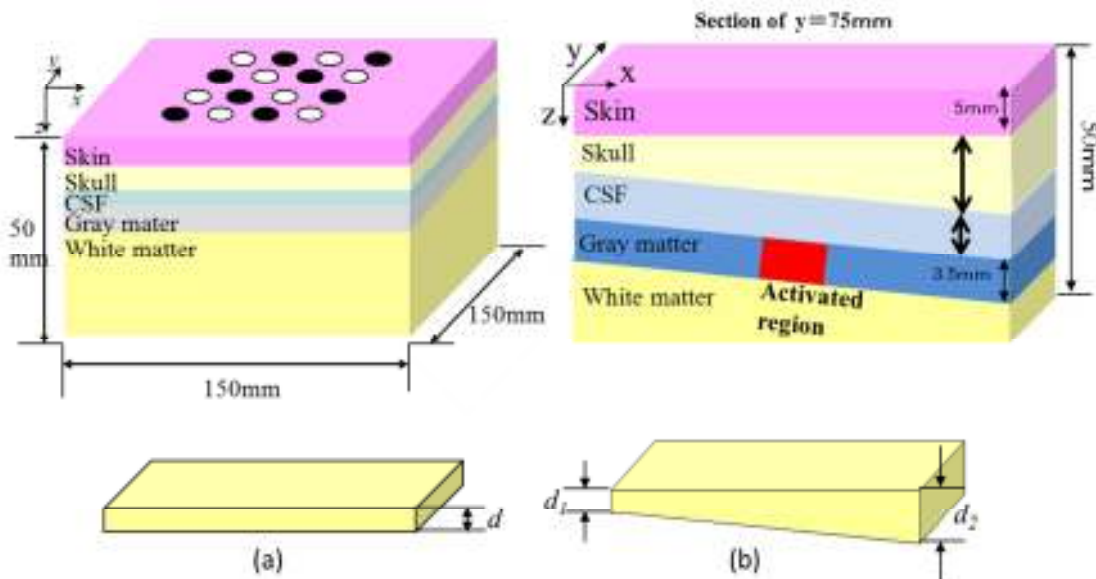


Fig. 3.1: Simulation models of human heads having five layers; skin, skull, CSF, gray matter, and white matter layers. The thickness of the skull or CSF layer is (a) uniform or (b) linearly varying in the x -direction, and the other layers are assumed uniform.

The thicknesses of the skull and CSF layers for the all cases are listed in Table 3.1. The optical properties of each layer at the wavelength of 805 nm are listed in Table 2.1. The arrangement of the source and detector probes in the simulation is based on Fig. 2.7. The activated regions are assumed to exist in the gray matter with the higher absorption coefficient than that of the surrounding brain tissues. The shape of an activated region is a circular disk with a diameter of 15 mm and a thickness of 3.5 mm. The activated region is located in two different ways as shown in Fig. 3.2; one is position A (the active region is just under a data point) and the other is position B (the active region is just under the middle of four data points).

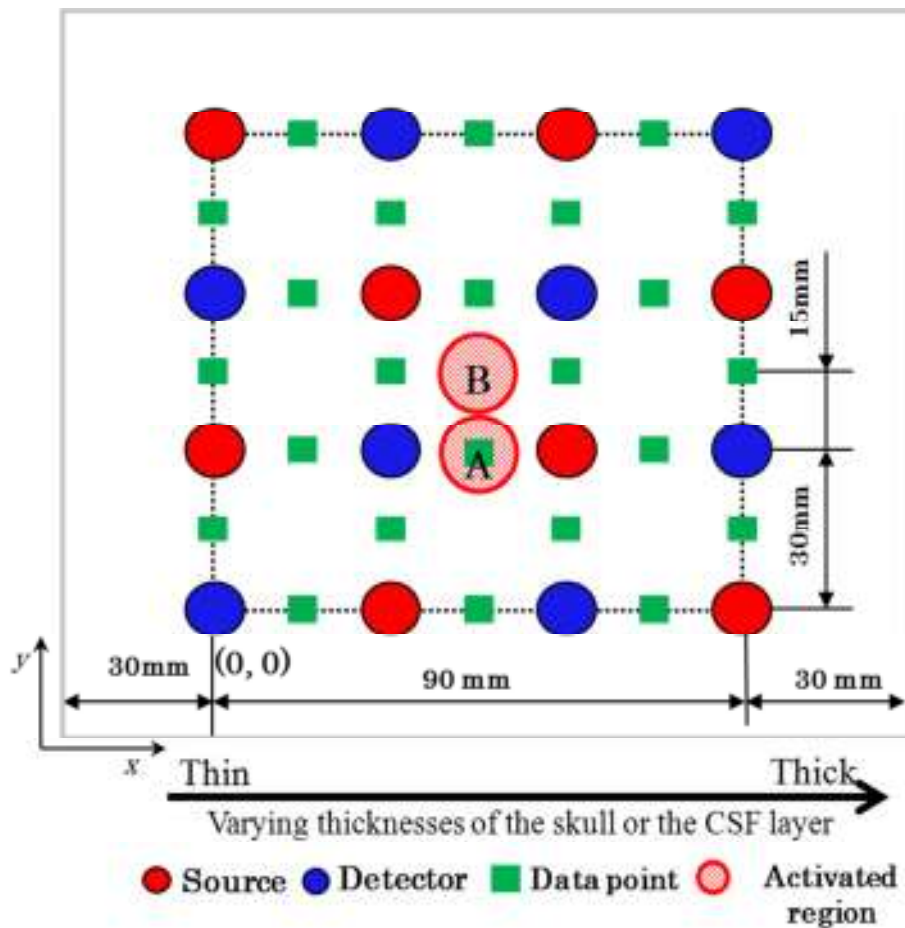


Fig. 3.2: Arrangement of the sources, detectors, data points, and activated regions.

Table 3.1 Thicknesses of the skull and CSF layers.

Case	Skull layer	CSF layer
S1	5 mm	
S2	10 mm	
S3	20 mm	3 mm
S4	5 - 10 mm	
S5	5 - 20 mm	
C1		1 mm
C2		3 mm
C3	5 mm	6 mm
C4		1 - 3 mm
C5		1 - 6 mm

Note: Thicknesses of the skin and gray matter layers are fixed as 5 mm and 3.5 mm, respectively, and the thickness of the white matter layer is the residual of the total 50 mm minus the thicknesses of the other four layers.

3.3 Results and Discussion

3.3.1 Effect of the thickness of the skull layer on mapping images

The thicknesses of the skin, CSF and gray matter layers are fixed to be 5 mm, 3 mm and 3.5 mm, respectively, and the thickness of the skull layer is varied for the cases from (S1) to (S5) as listed in Table 3.1.

3.3.1.1 Mapping images for uniform skull layer model

Before investigating the effects of the spatially varying thickness of the skull layer, the effects of the thickness of the uniform skull layer must be understood. The simulation results of mapping images with the uniform skull thickness of 5 mm (S1), 10 mm (S2) and 20 mm (S3) are shown in Fig. 3.3(a), (b) and (c), respectively. The

mapping images show the distributions of ΔOD for the cases of the activated region at position A with the same scale of the color bar as indicated in Fig. 3.3. As the skull thickness increases from 5 mm to 10 mm and 20 mm, the maximum of ΔOD decreases from 1.62×10^{-2} to 1.91×10^{-3} and 9.07×10^{-6} , respectively; i.e. the maximum of ΔOD decreases more than three orders of magnitudes. Therefore, for the case of the color bar with the maximum of 5×10^{-3} in Fig. 3.3, the image for (S1) is saturated while the image for (S3) is not observable. The relationship between the maximum of ΔOD and the skull thickness is approximately expressed by

$$\Delta OD_m = 0.226 \exp(-0.503 t_s) \quad \text{for position A} \quad (3.1)$$

where ΔOD_m is the maximum of ΔOD and t_s is the skull thickness. The relationship of ΔOD_m and t_s is an exponentially decreasing function, and ΔOD_m decreases to 40 % of its original value with every 1 mm increase in the skull thickness. Due to the strong light scattering by the skull layer, the value of ΔOD decreases significantly as the skull thickness increases. With the same scaling of ΔOD of 5×10^{-3} , the image of the activated region for (S3) is not observable as stated above. However, when the ΔOD values are normalized by the ΔOD_m in each case of Fig. 3.3, almost the same images of ΔOD for (S1), (S2) and (S3) are obtained although the figures are not presented. This can be quantitatively understood by calculating the full width at half maximum (FWHM) of the ΔOD profiles. Fig. 3.3 (d) shows the ΔOD profiles along the line in the x -direction indicated by the chain lines in panels (a), (b) and (c). The FWHMs of the curves in Fig. 3.3 are 24.7 mm, 24.9 mm and 25.9 mm for (S1), (S2) and (S3), respectively, and this slight change in the FWHM is hardly observable in the mapping image.

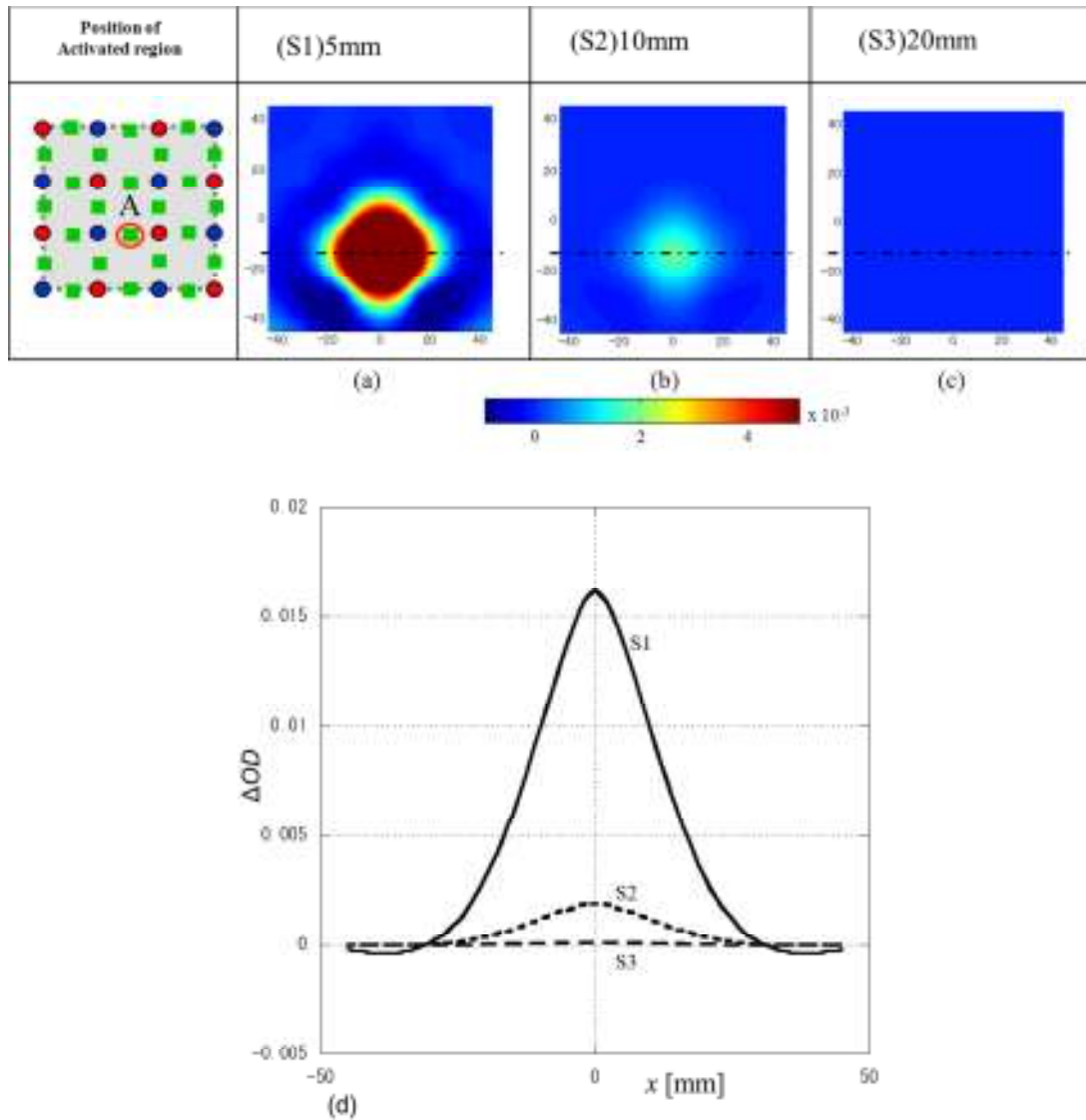


Fig. 3.4: Simulated optical mapping images of single activated regions at position A for the uniform skull layers with the thicknesses of (a) 5 mm (S1), (b) 10 mm (S2), and (c) 20 mm (S3). Panel (d) shows the ΔOD profiles along the line in the x -direction indicated by the chain lines in panels (a), (b) and (c).

Figure 3.4 compares the mapping images for the cases of (a) a single activated region at position A, (b) a single activated region at position B and (c) double activated regions at positions A and B for the uniform skull layers when the skull thickness is 5 mm (S1). Even if the size and absorption coefficient of an activated region are fixed,

mapping images are different for the different position of the activated region relative to the data points as investigated previously by Yamamoto et al [63]. In the case of the double activated regions existing at positions A and B simultaneously, the activated region at position B becomes difficult to be recognized as confirmed by Fig. 3.4 (c). In order to avoid this disadvantage, Yamamoto et al.[63] reported that the images can be improved by increasing the density of the probes twice or four times. An image reconstruction algorithm to improve the images of multiple activated regions was also proposed by use of the sensitivity distribution as priori information [26]. Figure 3.4(d) shows the ΔOD profiles along the line in the x -direction indicated by the chain lines in panels (a), (b) and (c). The maxima of ΔOD , ΔOD_m , are almost the same for panels (a) and (c).

Figure 3.4 is presented also for the purpose of comparing the effects of the position of the activated region relative to the data points when the skull thickness is uniform. The value of ΔOD_m of the activated region at position B is 2.82×10^{-3} and this is 17 % of that (1.62×10^{-2}) at position A. The distance between the centers of positions A and B is 15 mm. For the case of (S5) where the skull thickness varies from 5 mm to 20 mm over the lateral distance of 150 mm, the increase in the skull thickness over the distance of 15 mm is 1.5 mm. From eq. (3.1), it is estimated that the increase in the skull thickness (t_s) of 1.5 mm results in the decrease in ΔOD_m to 47 % of its original value. This decrease of 53 % is smaller than the decrease of 83 % which is caused by the difference in the position of the activated region between positions A and B stated above. For the case of (S4) the increase in the skull thickness over the distance of 15 mm is 0.5 mm, and this increase in the skull thickness results in the decrease in ΔOD_m to 78 % of its original value. Therefore, the effect of the difference in the position of the activated region relative to the data points (position A or B) is found to be greater than those of the varying skull thickness within the standard range of the variation such as cases (S4) and (S5).

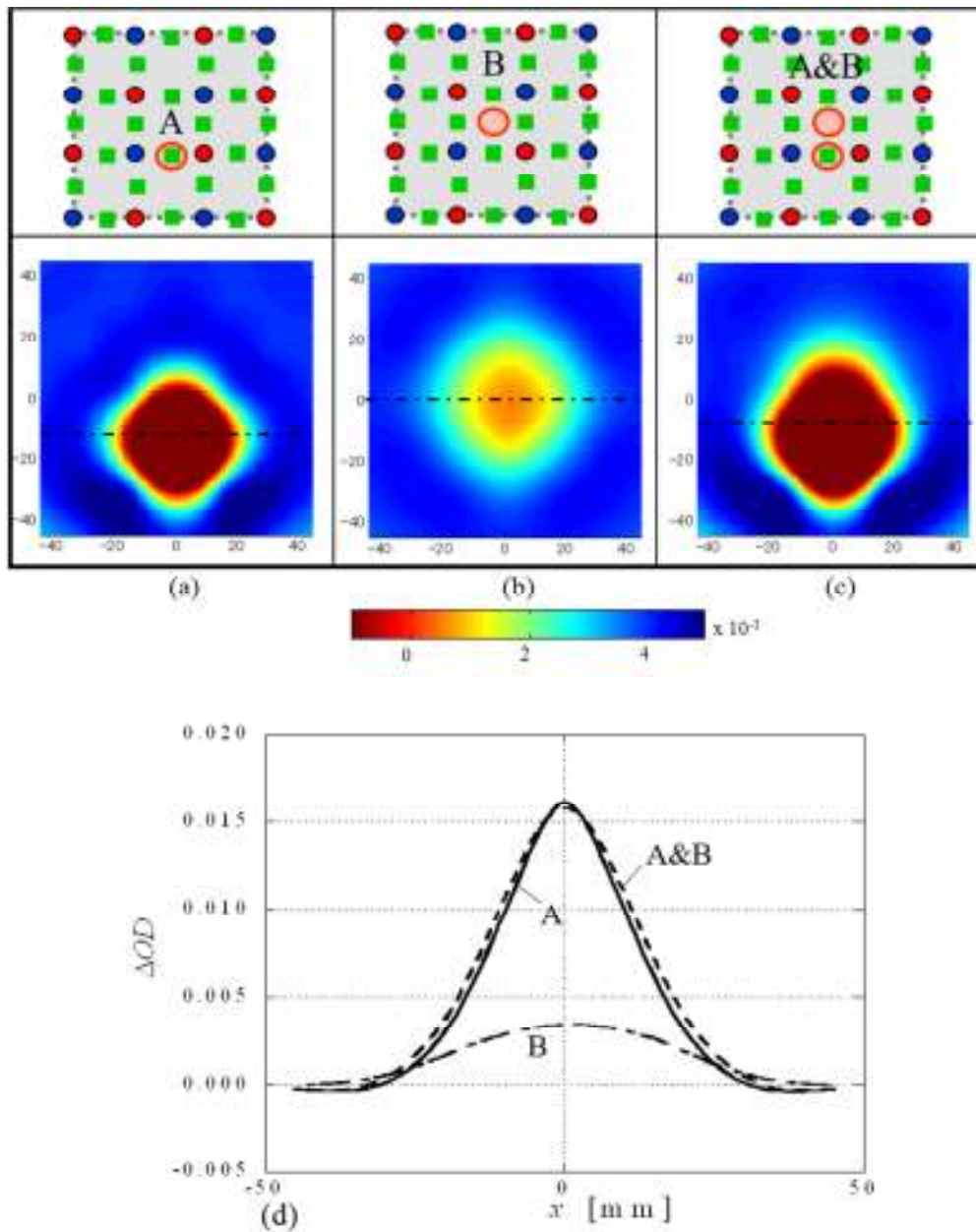


Fig. 3.5: Simulated optical mapping images of (a) single activated regions at position A or (b) that at position B, and (c) of double activated regions at positions A&B for the uniform skull layers with the thicknesses of 5 mm (S1). Panel (d) shows the ΔOD profiles along the line in the x-direction indicated by the chain lines in panels (a), (b) and (c).

3.3.1.2 Mapping images for spatially varying skull layer model

Figure 3.5(a) and (b) shows the results of the cases of spatially varying (non-uniform) thickness of the skull layer, (a) for (S4)(5-10 mm) and (b) for (S5)(5-20 mm) with a single activated region at position A. By comparing the images of non-uniform thickness with those of uniform thickness, it is seen that the shapes of the images are almost the same although ΔOD_m are different. This is because the change in the skull thickness within the size of the activated region in the x -direction (10 mm) is as small as 0.33 mm for (S4), and 1.0 mm for (S5).

To show the difference clearly, Fig. 3.5 (c) presents the profiles of ΔOD along the x -direction going through the center of the activated region at position A as indicated by the chain lines in Fig. 3.5(a) and (b). The distributions of ΔOD show a very small left-right asymmetry with respect to the vertical line at $x = 0$. In Fig. 3.5(c), the peaks of the curves have shifted to the left with 1.0 mm and 3.4 mm for (S4) and (S5), respectively. The (left) + (right) = (total) widths of the half maximum are $12.9 + 11.9 = 24.8$ mm and $14.0 + 11.2 = 25.2$ mm for (S4) and (S5), respectively, while the corresponding total widths for the uniform skull thicknesses are 24.7 mm, 24.9 mm and 25.9 mm for (S1), (S2) and (S3) as stated before. The results show that the spatially varying thickness of the skull layer causes asymmetry of the images of the activated regions.

Although the mapping images is not presented, Fig. 3.5 (d) shows the profiles of ΔOD along the x -direction going through the center of the activated region at position B for (S4) and (S5), to illustrate if the position of the activated region affects the asymmetry of the mapping images for the non-uniform skull thickness. In Fig. 3.5(d), the peaks of the curves have shifted to the left with 1.0 mm and 3.3 mm for (S4) and (S5), respectively. The deviations from the center line are almost the same as the cases in Fig. 3.5(c) for the activated region at position A, although the curves of ΔOD for the activated region at position B is smaller than those for position A. It can be said that the non-uniform variation in the skull layer thickness leads to slight asymmetry of the mapping images with respect to the center of the activated region, but the degree of the

asymmetry is independent of the position of the activated region relative to the data points.

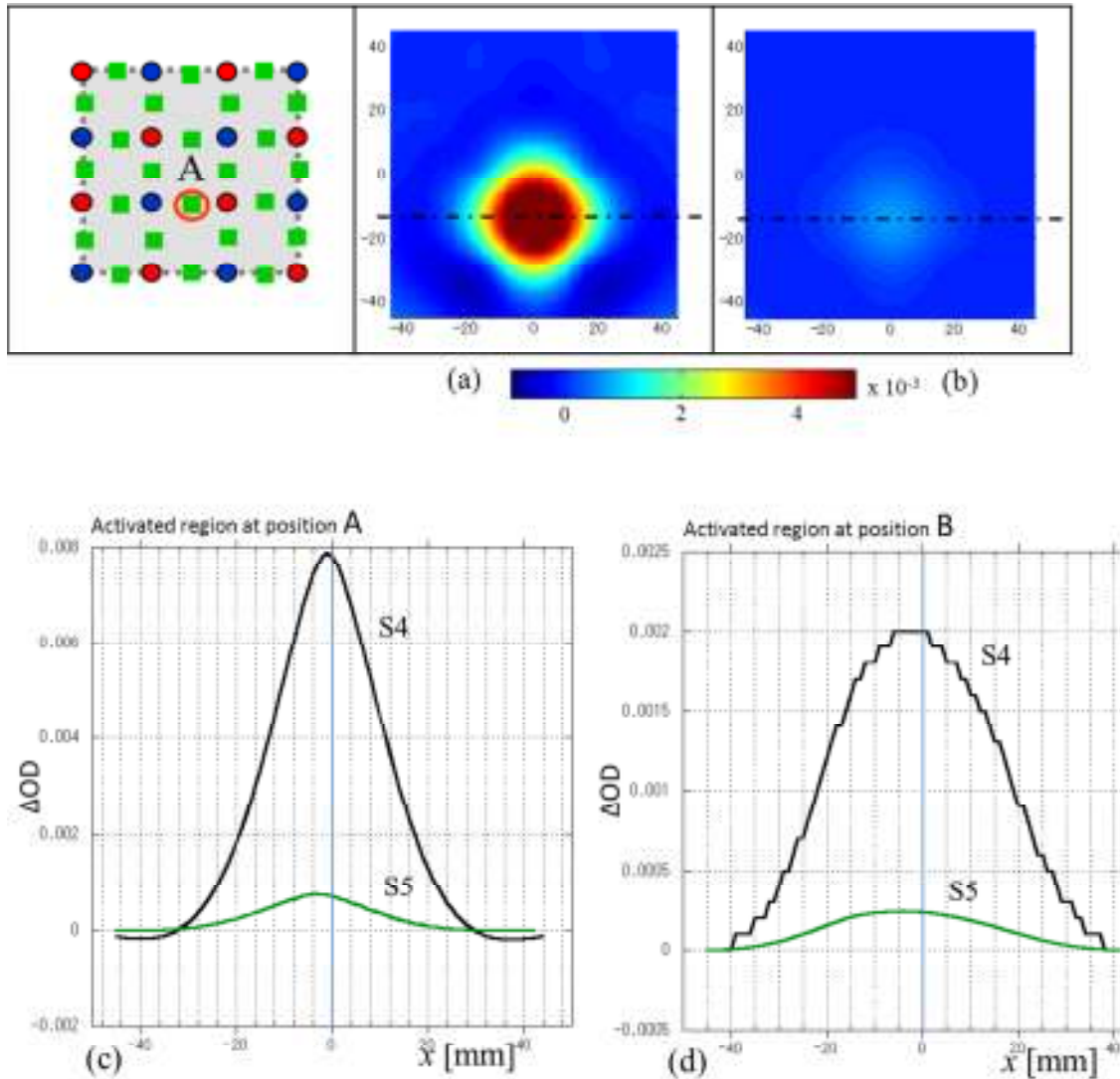


Fig. 3.6: Simulated optical mapping images of single activated regions at position A for the spatially varying thicknesses of the skull layer, (a) from 5 mm to 10 mm (S4) and (b) from 5 mm to 20 mm (S5). Panel (c) shows the ΔOD profiles along the line in the x -direction going through the center of the activated region at position A shown by the chain lines in panels (a) and (b). Panel (d) shows the ΔOD profiles similar to panel(c) except that the activated region is at position B for (S4) and (S5).

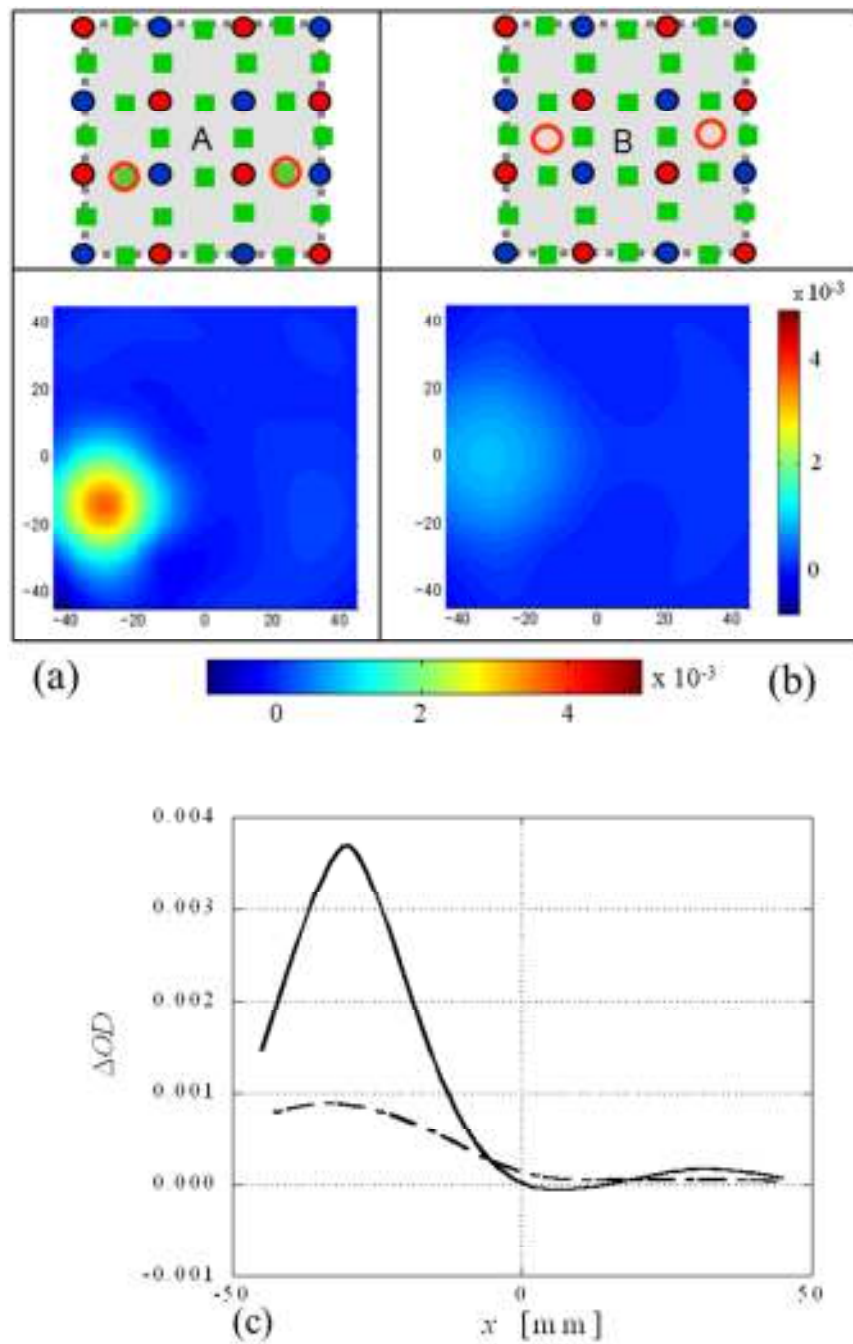


Fig. 3.7: Simulated optical mapping images of double activated regions with the spatially varying thickness of the skull layer from 5 mm to 10 mm (S4); (a) for the active regions at position A, and (b) for those at position B. Panel (c) shows the ΔOD profiles along the line in the x-direction shown by the chain lines in panels (a) and (b).

Figure 3.6 shows the mapping images of double activated regions for the spatially

varying skull thickness of (S4) (5-10 mm) with one activated region located under the thin skull (left hand side) and the other under the thick skull (right hand side). The values of ΔOD for the activated region under the thin skull are significantly greater than those under the thick skull, and the images of the activated regions under the thick skull almost disappear.

This result can be easily imagined after understanding the effect of the skull thickness as shown in Fig. 3.3. Although the result is not shown here by a figure, if the double activated regions exist at positions at A and B of Fig. 3.6 simultaneously under both the thin and thick skull, it is found that ΔOD of the activated region at thin skull and at position A is one-order of magnitude larger than those of the other three activated regions. Therefore, the three activated regions will not be observable unless the displaying range of ΔOD of the image is sufficiently large.

3.3.1.3 Light path probability distribution

To further examine the effect of varying skull thickness on mapping images, its effect on the path of light propagation for the arrangement of only one pair of source and detector with the source-detector distance of 30 mm is investigated by the path probability distribution, $\psi(r)$. For three cases of uniform thickness of skull 5 mm (S1), 10 mm (S2) and 20 mm (S3), the base-10 logarithms of $\psi(r)$ in the x - z plane including source and detector positions are shown in Fig. 3.7. As the skull thickness increases, the probability of light reaching the gray matter monotonically decreases. In order to show this decrease quantitatively, the values of $\psi(r)$ were integrated over the whole volume of the gray matter layer, and they were normalized by that of the case (S1). As shown in Fig.3.7 (d), these normalized values are found to be 1.00 for (S1), 0.47 for (S2) and 0.13 for (S3), respectively, showing that light reaching the gray matter decreases as the skull thickness increases. Because light is strongly scattered in the skull layer, light reaching the layers deeper than the skull layer decreases with the increase in the skull thickness. To see the change in the sensitivity distribution more clearly in Fig. 3.7, the contours of the path probability with the constant value of 12.5 % of the maximum $\log_{10}(\psi(r))$ in

each case are drawn by thick solid curves in each panel of Fig. 3.7. The maximum values of $\log_{10}(\psi(r))$ are -14.1, -14.5, and -14.8 for (S1), (S2) and (S3), respectively. It is clearly observed that light passing through the gray matter decreases with the increase in the skull thickness.

In optical mapping, the change in the measured optical density induced by the variation in the absorption coefficient (i.e. hemoglobin concentration) increases with the changes in the absorption coefficient occurring in the volume where the path probability is large. Therefore, the path probability, $\psi(r)$, can be interpreted as the sensitivity of the tissue at the position r to the change in the absorption coefficient for the case of a single pair of the source and detector. Therefore, the sensitivity at the position just under the data point is the greatest, and the sensitivity decreases as the position in the tissue leaves away from the data point.

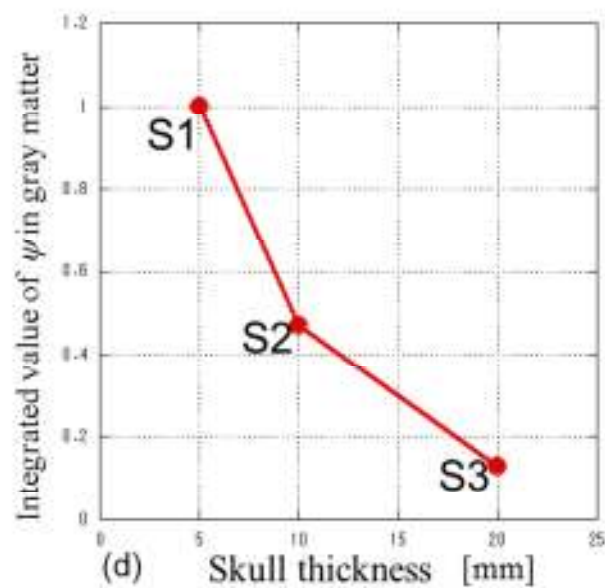
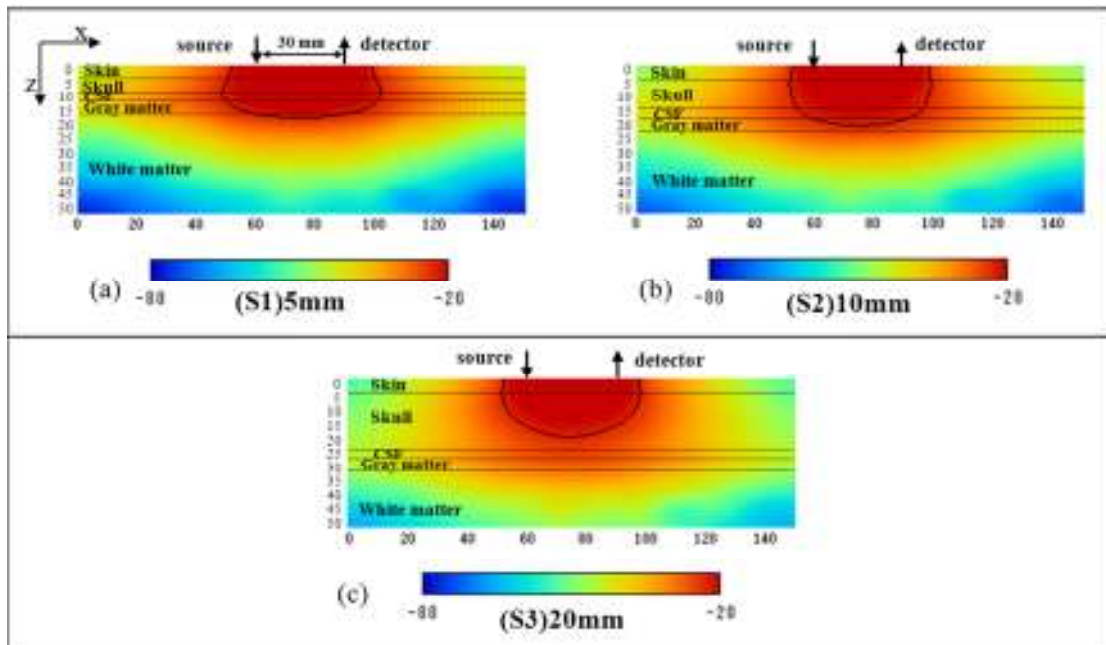


Fig. 3.8: Calculated path probability (sensitivity) distributions, $\log_{10}(\psi)$, for the uniform skull layers with the thickness of (a) 5 mm (S1), (b) 10 mm (S2), and (c) 20 mm (S3). Thick solid curves indicate the contours of constant $\log_{10}(\psi)$ with the value of 12.5 % of the maximum $\log_{10}(\psi)$ in each case. (d) The integrated value of ψ in the gray matter for (S1), (S2) and (S3).

3.3.2 Effect of the variation in the thickness of the CSF layer on mapping images

The thicknesses of the skin, skull and gray matter layers are fixed to be 5 mm, 5 mm and 3.5 mm, respectively, and the thickness of the CSF layer is varied for the cases from (C0) to (C5) as listed in Table 3.1.

3.3.2.1 Mapping images for uniform CSF layer model

The simulation results of the mapping images for the cases of (C0) to (C3) with a uniform thickness and single active region at position A are shown in Fig. 3.8 (a) to (d). The ΔOD profiles along the chain lines in the images are shown in Fig. 3.8(e), and the maxima of ΔOD are plotted as a function of the CSF layer thickness in Fig. 3.8(f). Comparing with the case of no CSF layer (C0), ΔOD increases as the CSF thickness increases from (C0) to (C1), and ΔOD decreases slightly when the CSF thickness increases further from (C1) to (C2) and (C3). The maxima of ΔOD are 1.41×10^{-2} , 1.72×10^{-2} , 1.62×10^{-2} and 1.34×10^{-2} for (C0), (C1), (C2) and (C3), respectively.

The FWHMs of the curves in Fig. 3.8(e) are 24.4 mm, 24.0 mm, 24.5 mm, and 24.8 mm for (C0), (C1), (C2) and (C3), respectively. Therefore, the mapping images normalized by their maxima are almost the same for the cases of (C0) to (C3) as long as the single activated region is located at the same position relative to the data points.

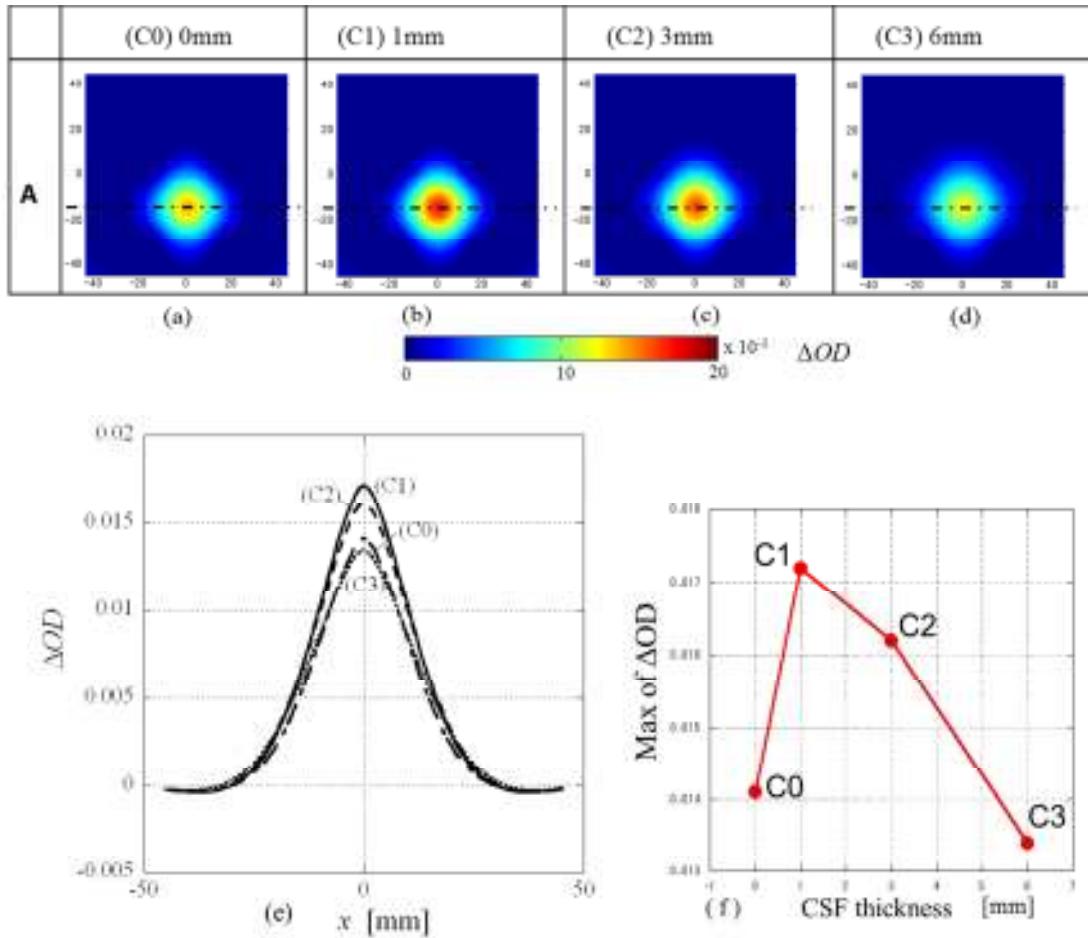


Fig. 3.9: Simulated optical mapping images of single activated regions at position A for the uniform CSF layers with the thicknesses of (a) 0 mm (C0), (b) 1 mm (C1), (c) 3 mm (C2), and (d) 6 mm (C3). Panel (e) shows the ΔOD profiles along the lines in the x-direction indicated by the chain lines in panels (a) to (d). (f) The maximum of ΔOD for (C0) ~ (C3).

3.3.2.2 Mapping images for spatially varying CSF layer model

Figure 3.9 (a) and (b) show the results of the cases (C4) and (C5) where the thickness of the CSF layer is not uniform and changes linearly in the x-direction. The effect of the spatially varying CSF thickness to the images is not observable clearly. This is because that the variation of ΔOD induced by the spatial change in the thickness is much smaller than the values of ΔOD in the images. To show the effect clearly, Fig. 3.9 (c) plots the values of ΔOD in the x-direction along the chain lines indicated in Figs. 3.9 (a) and (b). With respect to the vertical line at $x = 0$, small asymmetries of the curves

are observed showing the effect of the spatial variation in the CSF thickness. The peaks of the curves have shifted to the right with 2.0 mm and 2.1 mm for (C4) and (C5), respectively. The (left) + (right) = (total) widths of the half maximum are $11.1+13.1=24.2$ mm and $11.3+13.4=24.7$ mm for (C4) and (C5), respectively, while the corresponding widths for the uniform CSF thicknesses are 24.0 mm, 24.5 mm and 24.8 mm for (C1), (C2) and (C3), respectively, as stated above. These peak shifts to the right are opposite to those for the cases of the spatial variation in the skull as shown in Fig. 3.5. This difference in the peak shift reflects the opposite effect of the increasing thickness of the skull layer to that of the CSF layer. However, the magnitudes of the asymmetry in Fig. 3.9 (c) are so small that it can be said that the spatial variation of CSF layer has little effect on the distribution of ΔOD for the normalized mapping images, even for the case where the thickness of the CSF layer changes from 1 mm to 6 mm linearly over the distance of 150 mm along the head surface.

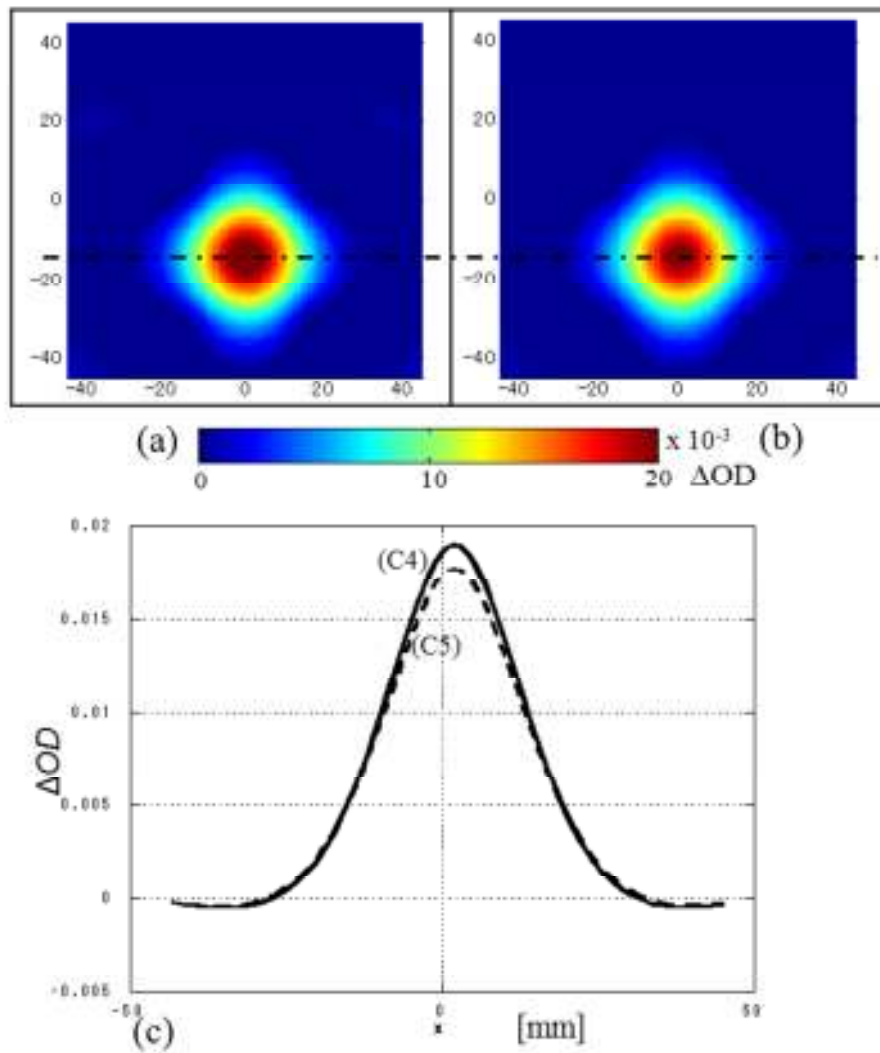


Fig. 3.10: Simulated optical mapping images of single activated regions at position A for the spatially varying thickness of the CSF layer, (a) from 1 mm to 3 mm (C4) and (b) from 1 mm to 6 mm (C5). Panel (c) shows the ΔOD profiles along the line in the x -direction shown by the chain lines in the panels (a) and (b).

Figure 3.10 shows the results for the case of (C5) where multiple activated regions with the same size exist under the locations of different thickness. Figure 3.10 (a) is for double activated regions located at position A, left one under the thinner CSF layer and right one under the thicker CSF layer, while Fig. 3.10 (b) is for double activated regions located at position B. Figures 3.10 (a) and (b) compare the differences in the mapping

images due to the positions of multiple active regions relative to the data points when the CSF thickness varies spatially. Figure 3.10 (c) shows the ΔOD distribution in the x -direction along the chain lines indicated in Figs. 3.10 (a) and (b). It can be seen that in the case of (a) ΔOD of the activated region of the left hand side (thinner CSF layer) is greater than that of the right hand side (thicker CSF layer), whereas in the case of (b) ΔOD of the left hand side is slightly smaller than that of the right hand side. This is because the sensitivity of the activated regions to the variation of CSF thickness changes with the positions of multiple activated regions relative to the data points. However, it may be hard to recognize the difference in the images between the left and right activated regions.

By comparing the images of Fig. 3.6 and Fig. 3.10, the difference in the effects of the thickness of the skull and CSF layers is clearly observed. For the case of varying skull thickness with double activated regions, the activated regions below the thicker skull will not be observable unless the displaying range of ΔOD of the image is sufficiently large. On the other hand, both of the double activated regions for the case of varying CSF thickness are observable even when the displaying range of ΔOD of the image is not large.

Although a figure showing the result is not presented, if the double activated regions at positions A and B in Fig. 3.10 exist simultaneously, ΔOD s of the activated regions at position B are significantly smaller than those of the activated regions at position A. Therefore, two activated regions at position A dominate in the image. However, the images of the two activated regions at position A are slightly elongated in the y -direction due to the existences of the activated regions at position B as seen in Fig. 3.4 (c). From these results, it can be concluded that the effect of the variation in the CSF thickness within the range considered in this study is much smaller than that of the position of the activated region relative to the data points.

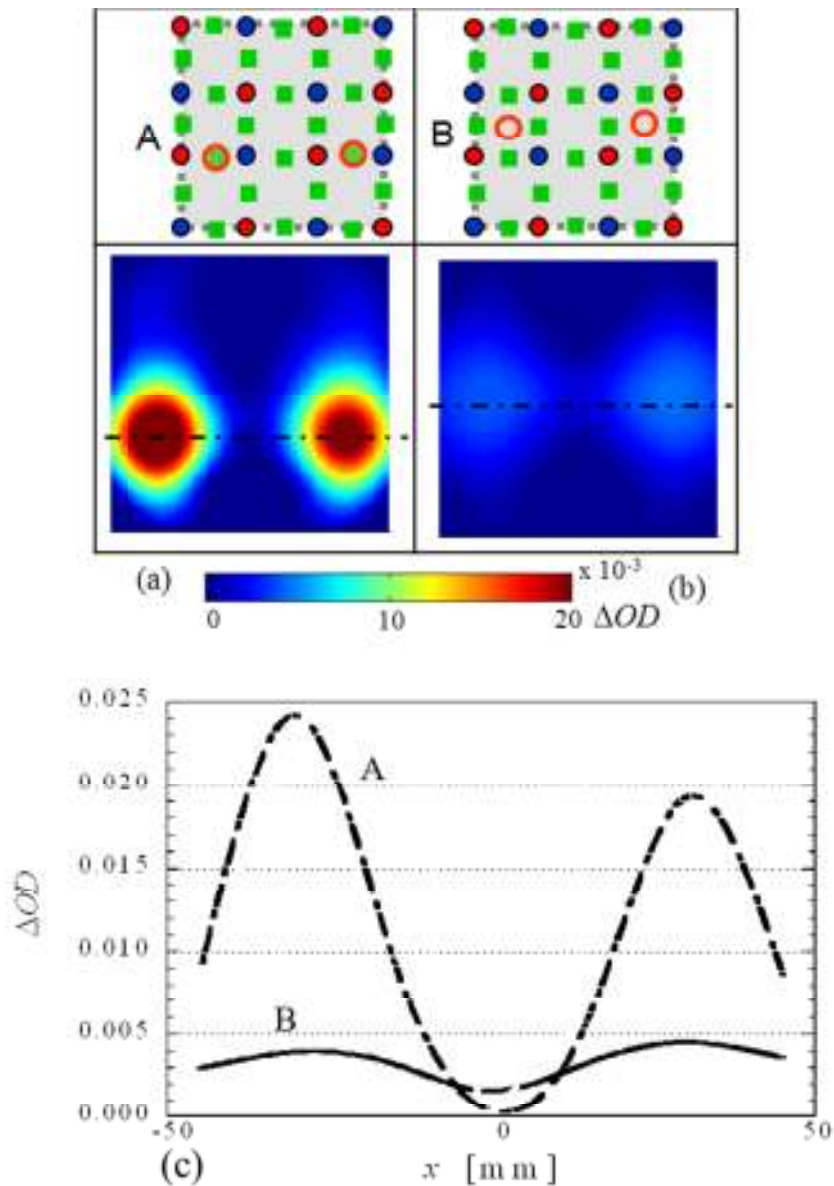


Fig. 3.11: Simulated optical mapping images of double activated regions with the spatially varying thickness of the CSF layer from 1 mm to 6 mm (C5); (a) for the active regions at position A, and (b) for those at position B. Panel (c) shows the ΔOD profiles along the line in the x-direction shown by the chain lines in the panels (a) and (b).

3.3.2.3 Light path probability distribution

To investigate the effect of CSF thickness on the path of light propagation in the head model in more detail, the path probability distribution, $\psi(r)$ is calculated for one

pair of source and detector with the source-detector distance of 30mm.

The CSF layer is assumed to be uniform with the thickness of 0 mm (C0), 1 mm (C1), 3 mm (C2), or 6 mm (C3), and $\psi(r)$ is calculated for the arrangement of only one pair of the source and detector with the source-detector distance of 30 mm. The base-10 logarithms of $\psi(r)$ in the x - z plane containing the source and detector positions are shown in Fig. 3.11(a) to (d). From the pattern of $\psi(r)$, it is seen that the increase in the CSF thickness enhances light spread in CSF layer, and resultantly more light passes through the gray matter. Thick solid curves in Fig. 3.11(a) indicate the contours of the constant sensitivity of 12.5 % of the maximum of $\log_{10}(\psi)$ in each case. The maximum values of $\log_{10}(\psi)$ are -14.68, -13.92, -14.1 and -14.77 for (C0), (C1), (C2) and (C3), respectively. As the thickness of the CSF layer increases, the constant sensitivity curves spread more along the brain surface.

To see it quantitatively, the integrated values of $\psi(r)$ in the gray matter are calculated, and they are normalized by that for the case of no CSF layer (C0). As shown in Fig. 3.11 (e), the integrated and normalized values are 1.00 for (C0), 1.51 for (C1), 1.43 for (C2) and 0.94 for (C3). Comparing with the integrated value for no CSF layer (C0), the amount of light passing through the gray matter for (C1) is more than 1.5 times that for (C0). However, when the CSF thickness increases to 3mm (C2) and 6 mm (C3), light passing through the gray matter slightly decreases to about 1.4 times and 0.9 times that for (C0). The effect of increasing the CSF thickness on the amount of light passing through the gray matter is in two ways, one is to increase the amount by spreading light wider in the CSF layer, and the other is to decrease the amount by putting the gray matter deeper. As the result of these two opposite effects of increasing the CSF thickness, the amount of light passing through the gray matter increases first and decreases as the CSF thickness increases from 1 mm to 6 mm. Normally, the thickness of the CSF layer hardly exceeds a few millimeters. Therefore, in most cases, it can be said that the existence of the low-scattering and low-absorbing CSF layer increases light passing through the gray matter.

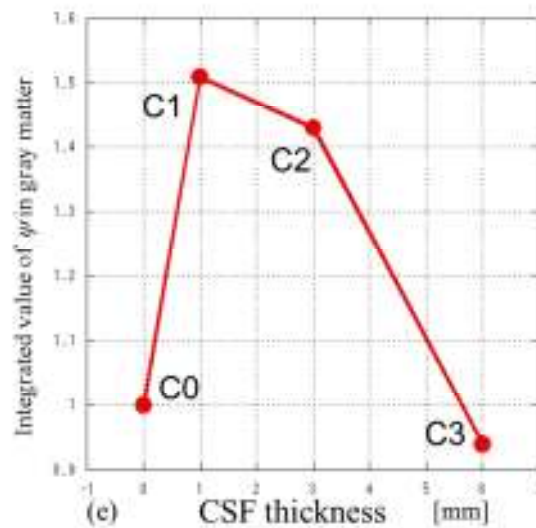
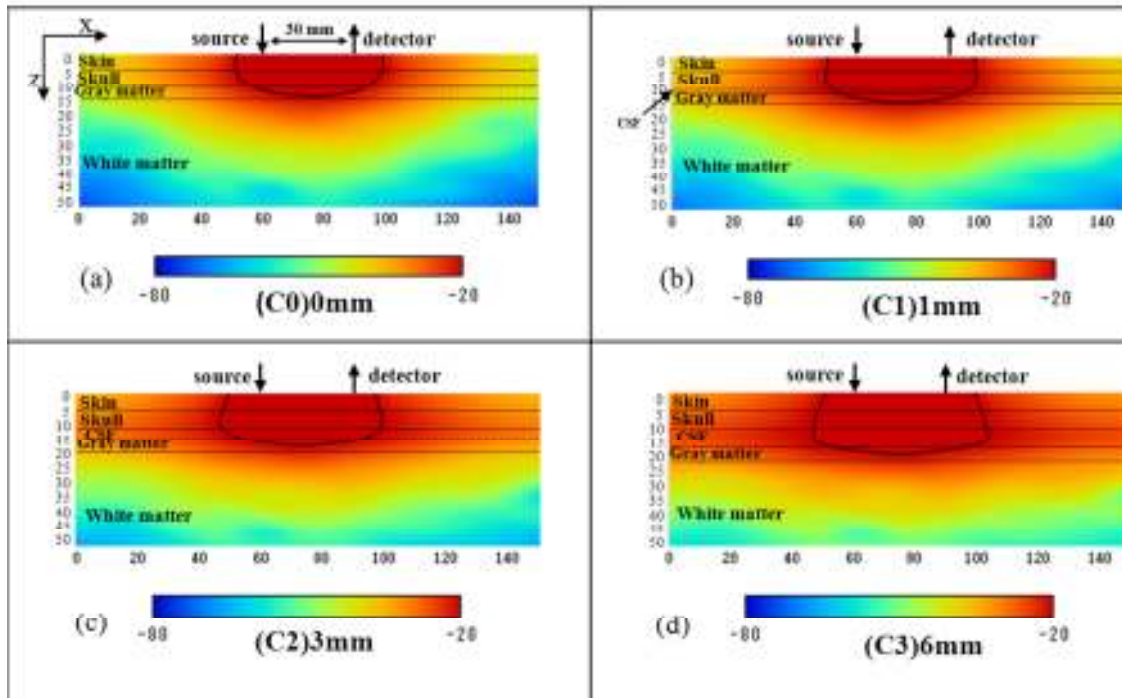


Fig. 3.12: Calculated path probability (sensitivity) distributions, $\log_{10}(\psi)$, for the uniform CSF layers with the thickness of 0 mm (C0), 1 mm (C1), 3 mm (C2), and 6 mm (C3). Thick solid curves indicate the contours of constant $\log_{10}(\psi)$ with the value of 12.5 % of the maximum $\log_{10}(\psi)$ in each case. (e) The integrated value of ψ in the gray matter for (C0) ~ (C3).

3.3.2.4 Existence of sulcus in gray matter

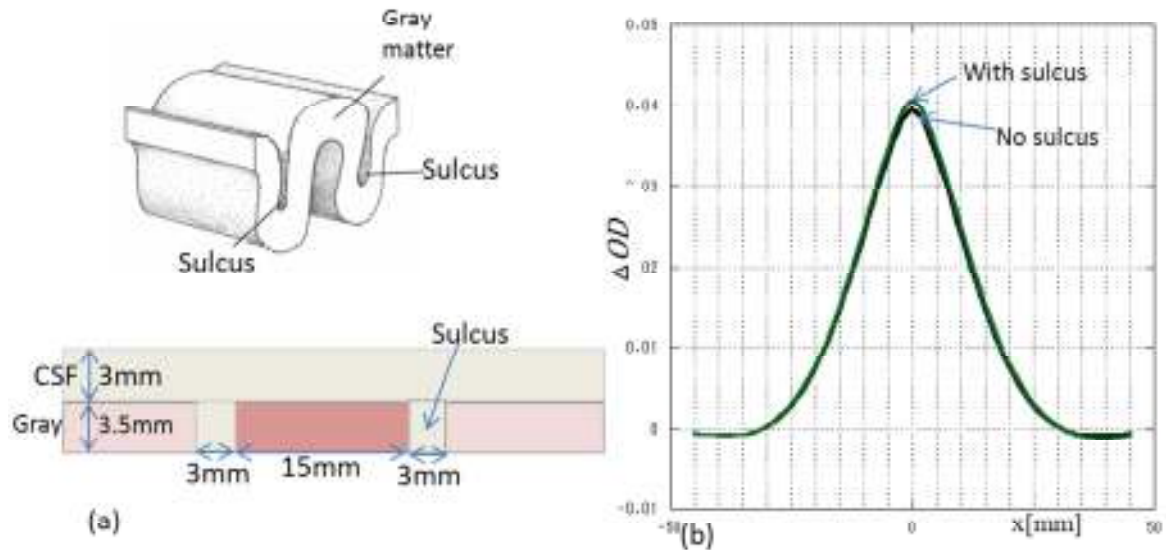


Fig. 3.13: (a) Simulation model with sulcus in gray matter. The optical properties of sulcus is the same with that of the CSF layer. (b) ΔOD profiles along the line in the x -direction going through the center of the activated region at position A for the cases of no sulcus and with sulcus in the gray matter.

Figure 3.13 show that the existence of sulcus near to activated region in gray matter increases the values of ΔOD slightly. If the activated region is located inside the sulcus and extended to deeper brain, the values of ΔOD may decrease because the activated region is more far away from the source-detector. Further study is necessary for this problem.

3.4 Conclusions

The effects of the thicknesses of the skull and CSF layers on optical mapping images are investigated by numerical simulation. The results showed the changes in the mapping images of the activated region caused by the variation in the uniform or non-uniform thickness of the skull or CSF layers with the varied number and position of the activated regions. Also, the sensitivity distributions of light for a single pair of the

source and detector are investigated, and the followings are concluded.

With the increase in the skull thickness from 5 mm to 20 mm, the value of ΔOD of the activated region decreases significantly. If only one activated region exists, it can be imaged in mapping images regardless of the thickness of the skull. When multiple activated regions are located under different skull thicknesses, the activated region under the thicker skull may not be observable in the mapping images unless the displaying range of ΔOD of the images is sufficiently large.

The mapping images of a single activated region located at the center of data points show a small left-right asymmetry for the non-uniform skull thickness of 5 mm to 10 mm and 5 mm to 20 mm. When double activated regions exist for the spatially varying skull thickness with one activated region located under the thinner skull and the other under the thicker skull, the values of ΔOD for the activated region under the thinner skull are greater than those under the thicker skull.

For the varying thickness of the CSF layer, the increase in the CSF layer thickness increases the value of ΔOD of the activated region generally because light spreads wider in the low scattering and low absorbing CSF layer. This is opposite to the case of the skull layer. However, when the CSF thickness increases further more than about 3 mm, the sensitivity slightly decreases because the depth of the gray matter layer increases and light is difficult to reach there. Overall, the effects of the CSF thickness on the mapping images are less significant than those of the skull thickness. The non-uniform variation of the CSF layer (1 mm to 6 mm) has a little effect on the distribution of ΔOD for mapping images.

It has also been found that for standard anatomical variations in human heads the effects of the varying thicknesses of skull and CSF layers on the mapping images are smaller than those of the position of the activated region relative to the data points.

In this chapter, the effects of the thickness variations in the skull and CSF layers on the optical mapping images are investigated quantitatively. To remove the effect of anatomy changes and improve the accuracy of the mapping image of the brain activation, these results can be used to compensate the mapping images in combination

with images of other modalities such as MRI and X-ray CT as a priori information of the head anatomy.

For the effects of the position of the activated region relative to the data points, a method of high-density probe arrangement [63] by increasing the data points can be used to improve the spatial resolution and accuracy of mapping images. In addition, an image reconstruction algorithm by solving inverse problem [26] may improve the spatial resolution of mapping images without increasing the number of source-detector pairs.

Chapter 4 Effects of Spatial Variation of Skull and Cerebrospinal Fluid Layers on Optical Mapping of Brain Activities: Phantom Experiments

4.1 Introduction

In chapter 3, the influences of spatial variations in the thickness of skull and CSF layers on optical mapping images are investigated by numerical simulation. The effect of the thickness of the CSF layer on the mapping image is found to be opposite to that of the skull layer. Besides the numerical approach, phantom experiments were also performed to investigate the effects of thickness variations of the skull and CSF layers on the mapping images. So far, only a few numerical simulations directly have studied the effects of the superficial layer thicknesses of human head on the NIRS signals [59-61]. It is the first time that phantom experiments were performed to investigate the effects of the spatial variations of the skull and CSF layers on the mapping images of brain activities. A five-layered slab phantom model was used to simulate adult heads. The spatial variations in the thicknesses of the skull and CSF layers were adjusted by changing the skull and CSF layer phantoms having different thicknesses. The skull thickness varied from 5 mm to 20 mm and the CSF thickness expanded from 0 mm to 6 mm. The thicknesses of the skin and gray matter layers were fixed. The optical properties of each layer remained the same. As mentioned in Section 2.4.4, the multi-channel CW NIRS imaging system (FOIRE-3000: Shimadzu Corporation) was used in the experiment.

4.2 Head phantoms

The head model consisted of five layers, skin, skull, CSF, gray matter and white matter layers. In this study the thicknesses of the skin and gray matter layers were fixed to be 5 mm and 3.5 mm, respectively. The thickness of the whole head model was fixed as 50 mm, and the thickness of the white matter layer was changed according to the variation in the thicknesses of the skull and CSF layers. The thickness of the skull and CSF layer was uniformly varying or linearly varying in the x -direction, and the other layers were kept uniform.

4.2.1 Variation of the skull thickness

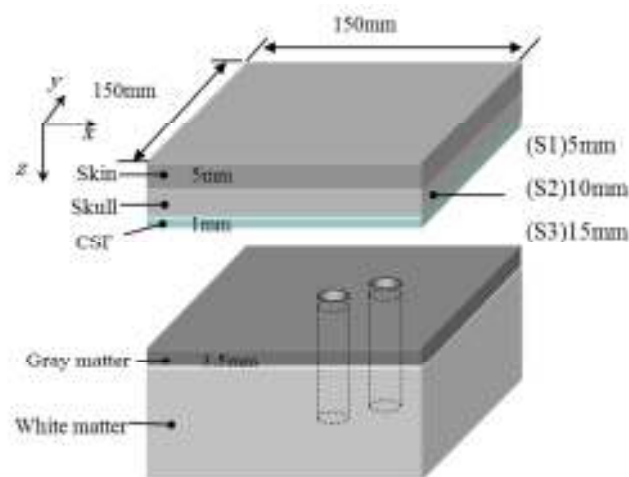


Fig. 4.1: Human head phantoms with a uniform thickness of the skull layer, (S1) 5 mm, (S2) 10 mm and (S3) 15 mm.

The human head phantoms simulating spatial variations of the skull layer thickness are shown in Figs. 4.1 and 4.2. The thickness of the skull layer was varied as the following five cases; i.e., uniform thickness of 5 mm (Case S1), 10 mm (Case S2), 20 mm (Case S3) as shown in Fig. 4.1, and linearly varying thickness in the x -direction of the simulation area from 5 mm to 10 mm (Case S4), and from 5 mm to 20 mm (Case S5) with the unchanged CSF thickness of 1 mm (see Fig. 4.2).

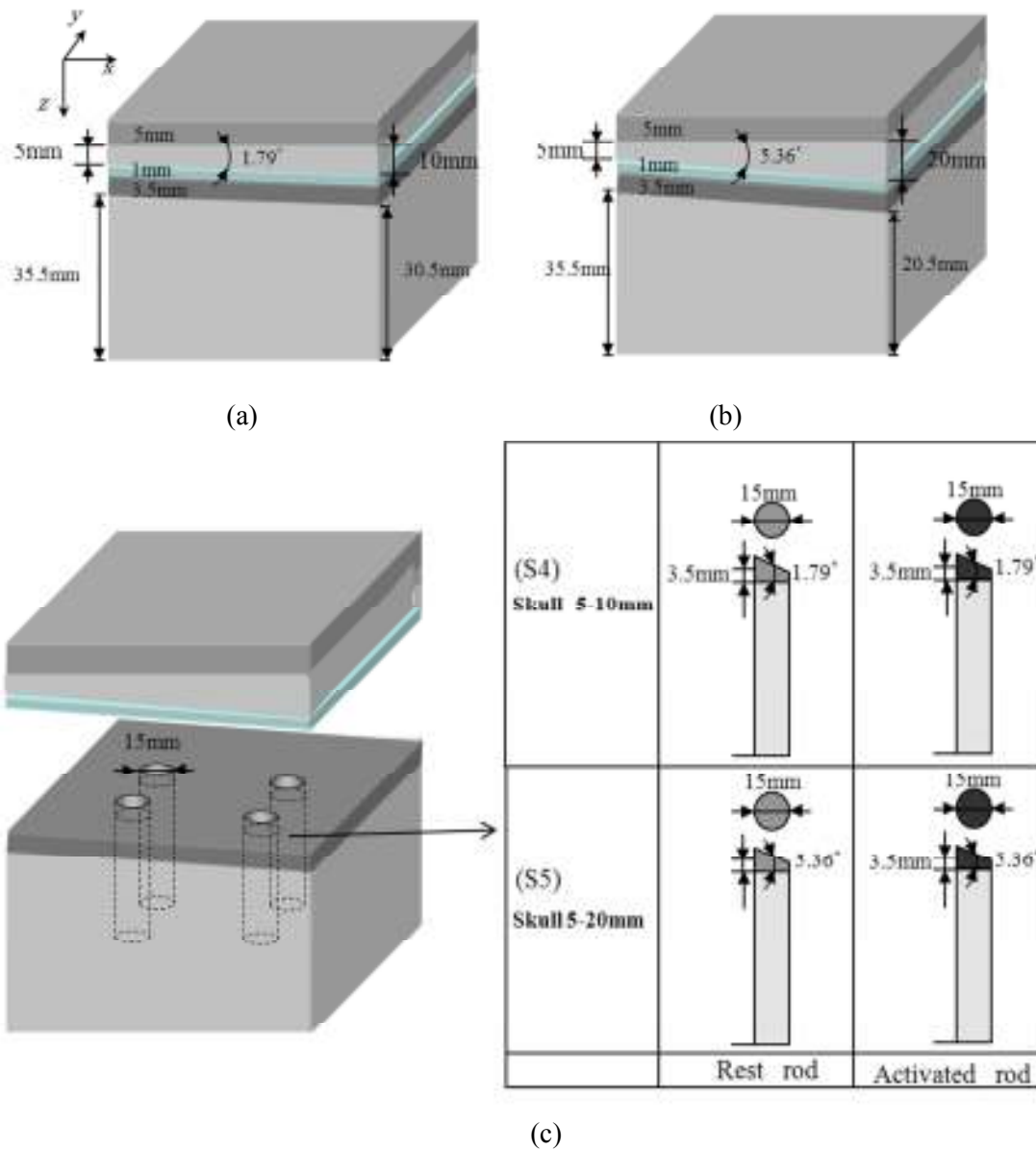


Fig. 4.2: Human head phantoms with linearly varying thickness of the skull layer in the x -direction, (a) (S4) skull: 5 mm-10 mm, (b) (S5) skull: 5 mm-20 mm. (c) Rods simulating the rest and activated states in the gray matter for (S4) and (S5).

4.2.2 Variation of the CSF thickness

The human head phantoms simulating spatial variations of the CSF layer thickness are shown in Figs. 4.3 and 4.4. The CSF layer was varied from no CSF layer (Case C1)

to uniform thickness of 1 mm (Case C2) and 3 mm (Case C3) as shown in Fig. 4.3, and linearly varying thickness in the x -direction of the simulation area from 1 mm to 3 mm (Case C4), and from 1 mm to 6 mm (Case C5) as shown in Fig. 4.4. The skull thickness was unchanged as 5 mm.

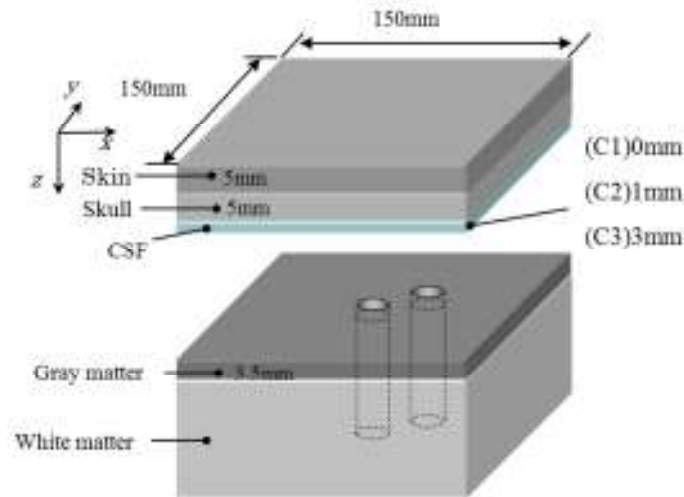


Fig. 4.3: Human head phantoms with a uniform thickness of the CSF layer. (C1) 0 mm, (C2) 1 mm and (C3) 3 mm.

The standard optical properties of each layer at the wavelength of 805 nm are listed in Table 2.16. The size of an active region was assumed as a disk with a diameter of 15 mm and thickness of 3.5 mm. The arrangement of the sources, detectors, data points and activated regions are shown in Fig. 4.5. The single activated region was located at position A or B as shown in Fig. 4.5 (a) for the uniform thickness of the skull or CSF layer, and double activated regions are located at positions C or D as shown in Fig. 4.4 (b) for the linearly varying thickness of the skull or CSF layer.

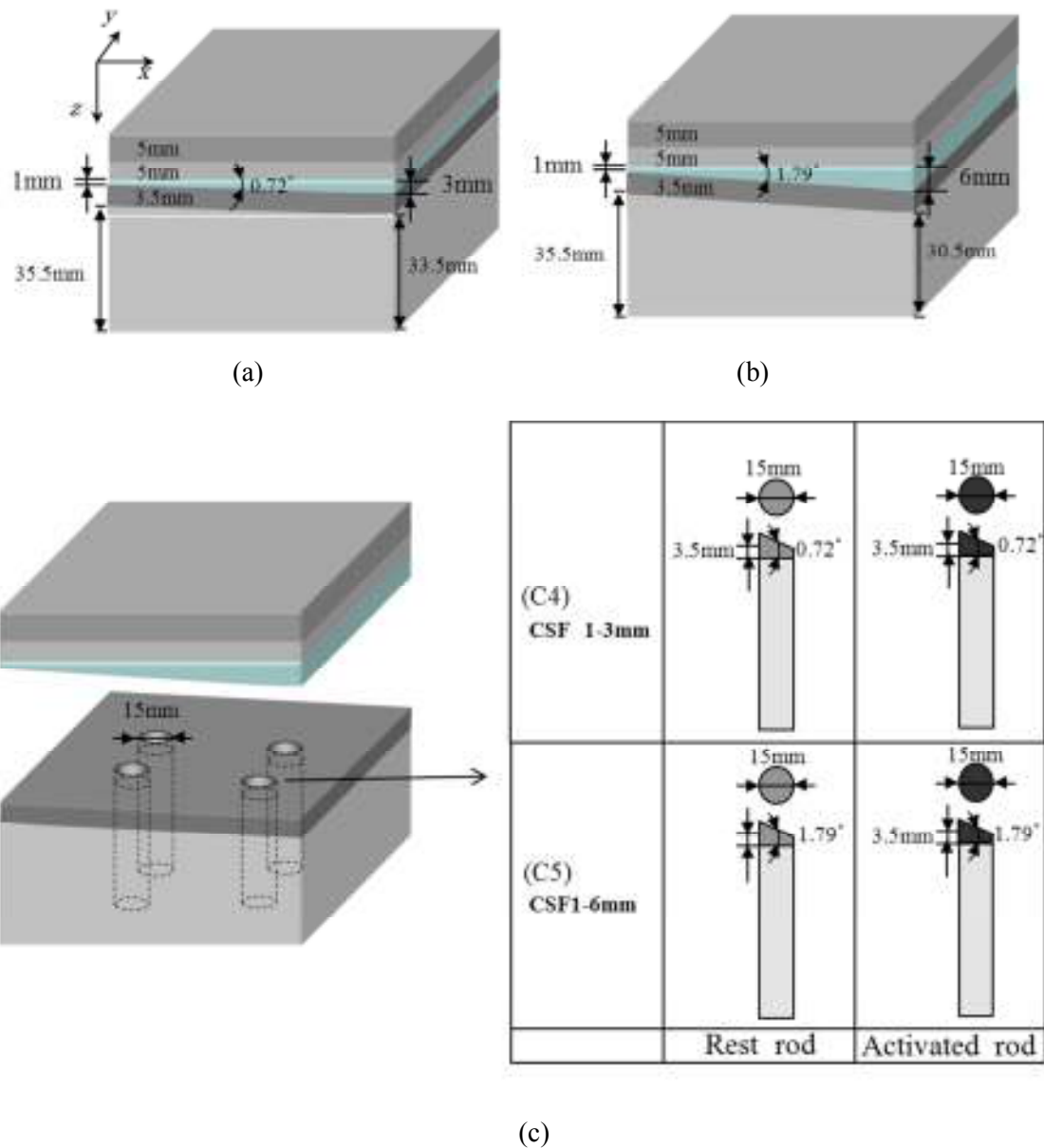


Fig. 4.4: Human head phantoms with the linearly varying thickness of the CSF layer in the x -direction. (a) (C4) CSF: 1 mm-3 mm, (b) (C5) CSF: 1 mm-6 mm. (c) Rods simulating the rest and activated states in the gray matter for (C4) and (C5).

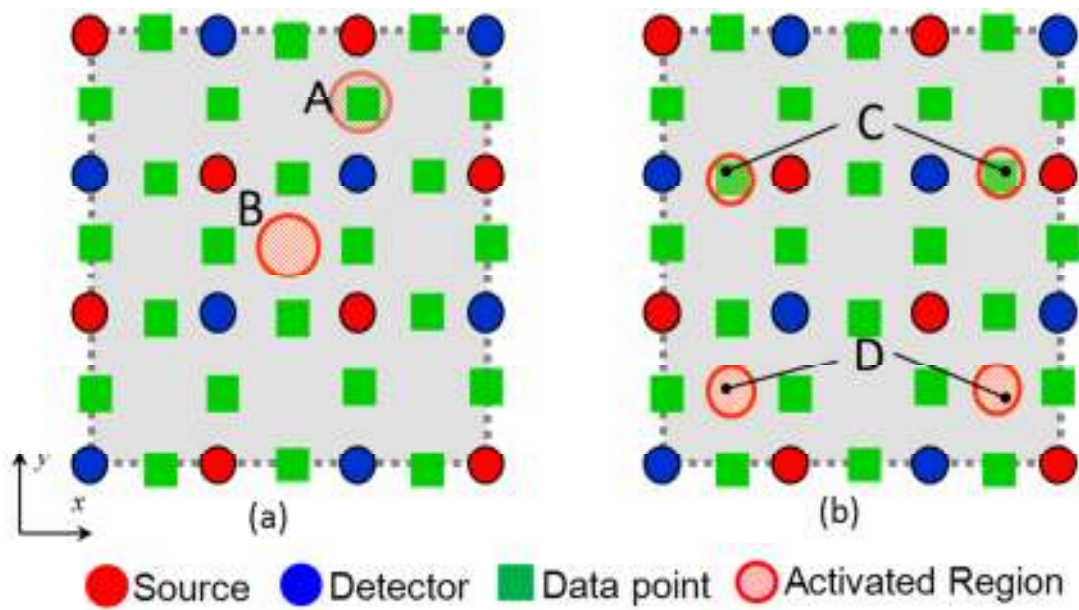


Fig. 4.5: Arrangement of the sources, detectors, data points and activated regions. (a) Single activated region for the uniform thickness of the skull or CSF layer, (b) Double activated regions for the linearly varying thickness in the x -direction of skull or CSF layer. Positions B and D in the gray matter layer were below the middle of the four neighboring data points, positions A and C in the gray matter layer below the data points.

4.3 Results and Discussions

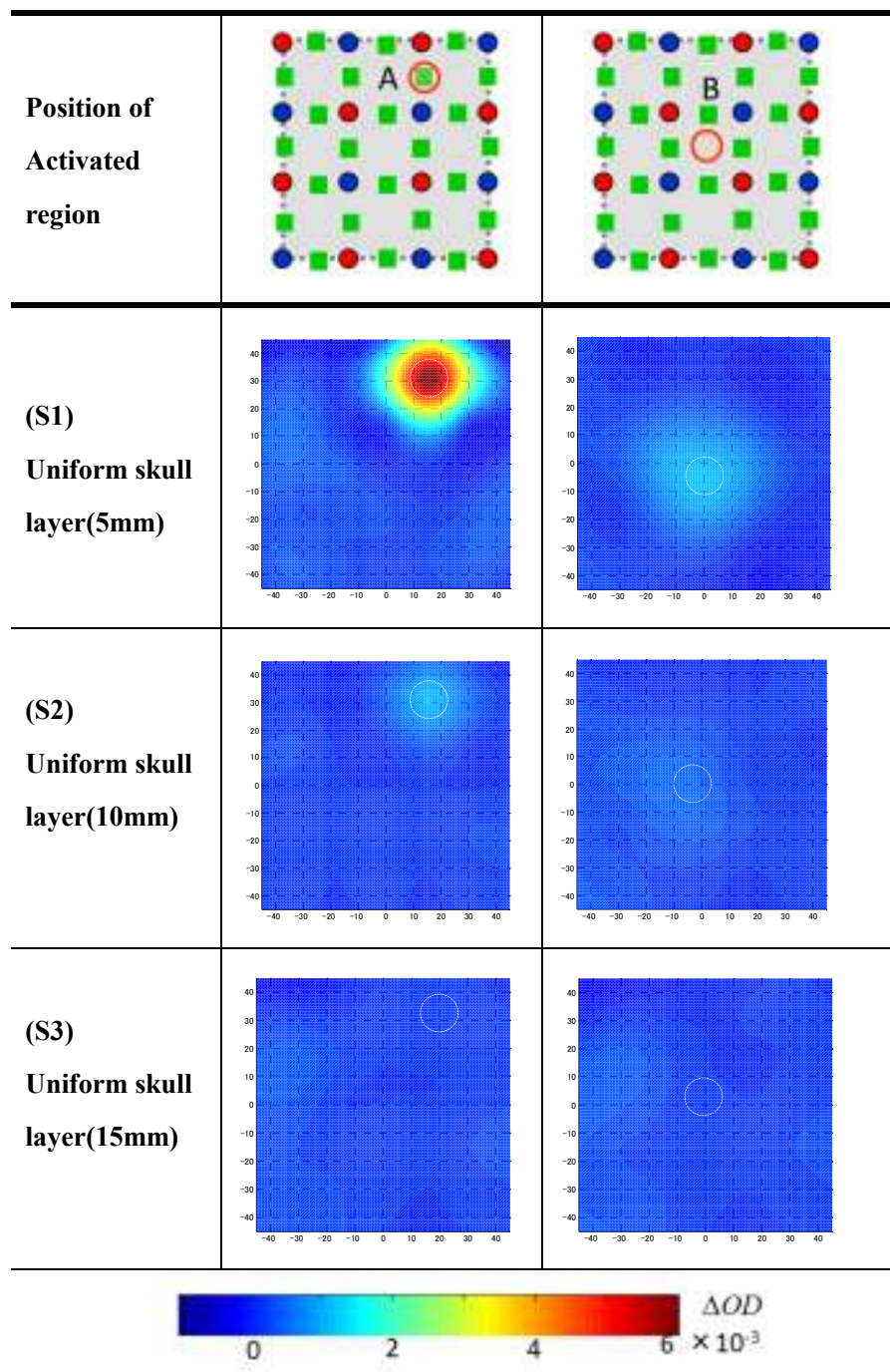


Fig. 4.6: Optical mapping images of single activated region at position A or B obtained by phantom experiments, for the uniform skull thickness of (S1) 5 mm, (S2) 10 mm and (S3) 15 mm. The dashed circles in the mapping images indicate the true activated regions.

The optical mapping images obtained by the phantom experiments are shown in Fig. 4.6 for cases (S1), (S2) and (S3) with the uniform skull thickness. Each measurement was repeated five times and the mean of the ΔOD s were used to construct the mapping images. The color bar shows the value of the ΔOD . Figure 4.7 shows the maxima of ΔOD in the activated regions at positions A and B as a function of the skull thickness. The error bars represent the standard deviations (SD) of the repeated five measurements, which are less than 5% indicating a good reproducibility. As the skull thickness increased from 5 mm to 10 mm and 20 mm, the value of ΔOD by brain activity in the mapping images decreased at both positions A and B. By increasing the skull thickness from 5 mm to 10 mm, the value of ΔOD by brain activity greatly decreased. While the skull thickness increased from 10 mm to 15 mm, the value of ΔOD by brain activity changed slightly. With the same color bar, in the mapping images with the skull thickness of 10 mm (case (S2)), the activated region at position B was unobservable. Moreover, for case (S3) with skull thickness of 15 mm, the activated regions at both positions A and B were unobservable.

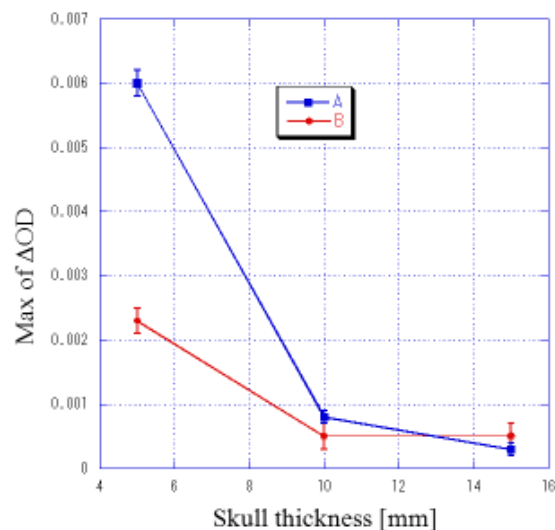


Fig. 4.7: Maxima of ΔOD in the activated regions at position A or B as a function of the uniform skull thickness of (S1) 5 mm, (S2) 10 mm and (S3) 15 mm. Error bars represent the standard deviations of the repeated five measurements.

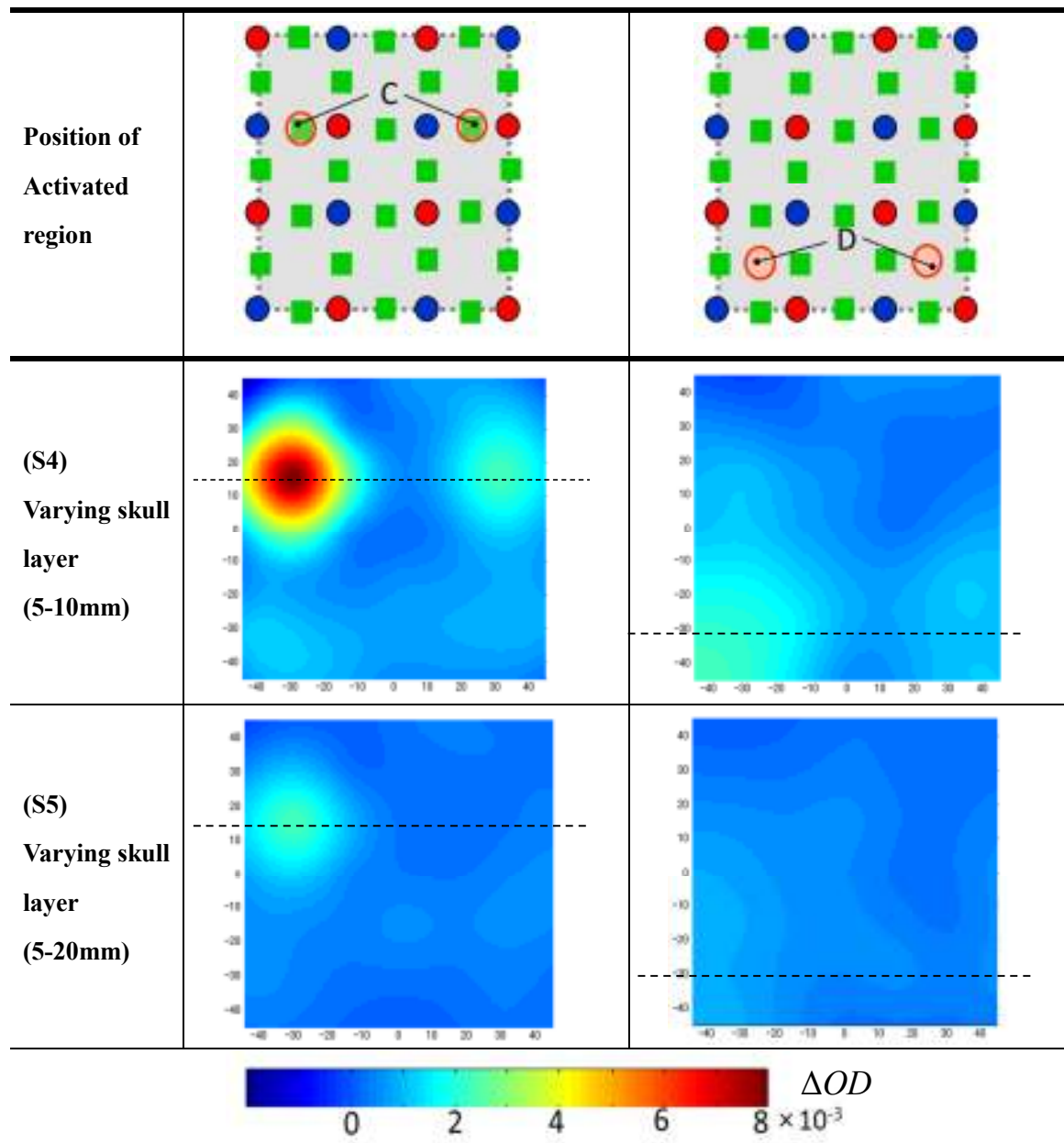


Fig. 4.8: Optical mapping images obtained by phantom experiment for the linearly varying skull thickness with (S4) 5 mm - 10mm and (S5) 5 mm - 20mm when the double activated regions were located at position C or D. The dashed horizontal lines pass through the centers of the double activated regions.

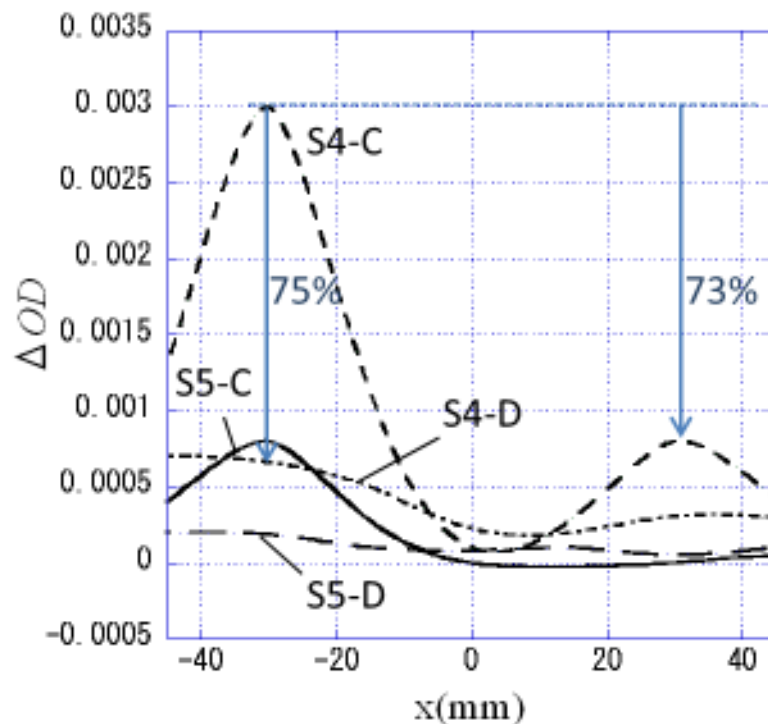


Fig. 4.9: Profiles of ΔOD along the dashed lines in Fig. 4.8. (S4-C) skull thickness varying from 5 mm to 10 mm with the double activated regions at position C, (S5-C) skull thickness varying from 5 mm to 20 mm with the double activated regions at position C, (S4-D) skull thickness varying from 5 mm to 10 mm with the double activated regions at position D, and (S5-D) skull thickness varying from 5 mm to 20 mm with the double activated regions at position D.

Figure 4.8 shows the mapping images for the cases of double activated regions at position C or D with the linearly varying skull thickness of (S4) 5-10 mm and (S5) 5-20 mm. Figure 4.9 plots the ΔOD profiles along the dashed lines in the mapping images of Fig. 4.8. The increase in the skull thickness reduced the values of ΔOD . The values of ΔOD for the activated region below the thin skull were significantly greater than those below the thick skull for the activated regions both at positions C and D. When the skull thickness above the activated regions was more than 10 mm, the activated regions were unobservable for the activated regions both at positions C and D. The experimental results about the effects of the skull thickness and the position of the activated region on the mapping images were similar to the simulation results in section 3.3.1.2.

For case (S4) with the activated region at position C (curve S4-C in Fig. 4.9), the

maximum of ΔOD in the thicker skull decreased 73% from that in the thinner skull. For both cases (S4) and (S5), the ΔOD values for the activated region at position C were larger than those at position D. When the maximum ΔOD s for the activated region at position C in the thinner skull were compared between for the cases (S4) and (S5) (curves S4-C and S5-C in Fig. 4.9), the maximum ΔOD for (S5-C) decreased 75 % from that for (S4-C). The ΔOD values decreased with the increase in the skull thickness and with the increase in the distance between the activated regions and the data points. It is difficult to tell which effect is dominating in the mapping images, the variation in the skull thickness or the positions of the activated regions relative to the data points, only from the ΔOD values.

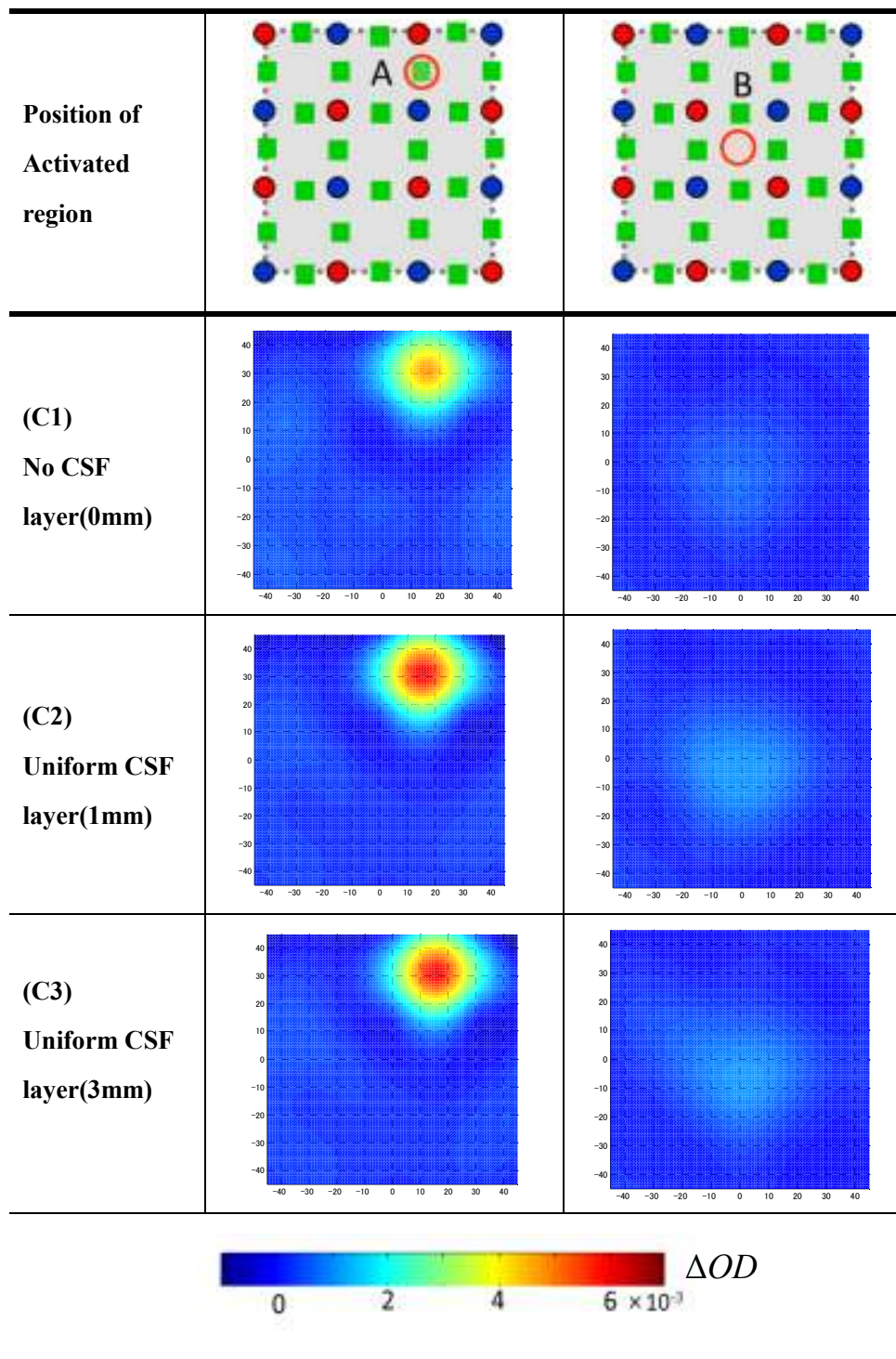


Fig. 4.10: Optical mapping images by phantom experiments for the uniform CSF thickness, (C1) 0 mm, (C2) 1 mm and (C3) 3 mm with the activated region at position A or B.

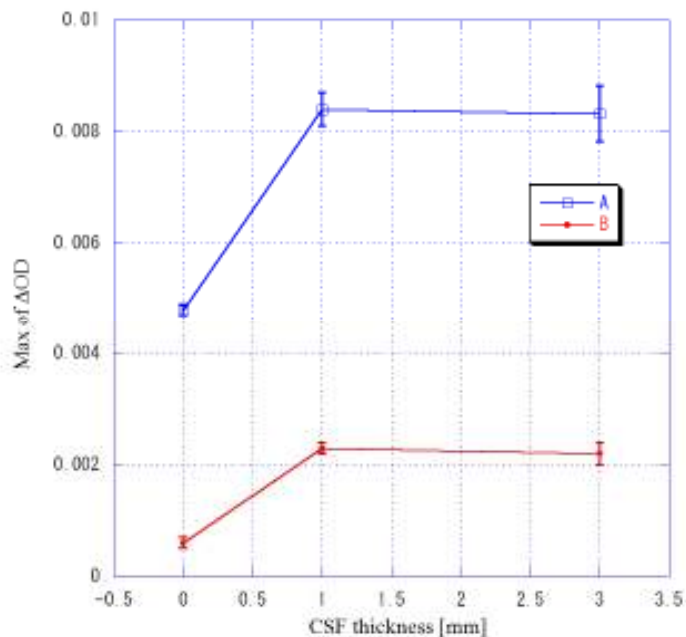


Fig. 4.11: Maximum of ΔOD in the mapping images for the cases of uniform CSF thicknesses with the activated regions at positions A and B. Error bars represent the SD of repeated five measurements.

Mapping images of the phantom experiments with the uniform thickness of the CSF layer are shown in Fig. 4.10 for the cases of (C1) no CSF layer, CSF layer with thickness of (C2) 1 mm and (C3) 3 mm. The single activated region was located at position A or B. Figure 4.11 shows the maxima of ΔOD for the cases of (C1), (C2) and (C3) with the SD of repeated five measurements. Comparing with the case of no CSF layer (C1), the value of ΔOD increased for the cases of (C2) and (C3) with the CSF layer thickness of 1 mm and 3 mm, respectively. The value of ΔOD increased as the CSF thickness increased from 0 mm to 1 mm while it slightly decreased as the CSF thickness increased from 1 mm to 3 mm, for the activated region at both positions A and B. The values of ΔOD for the activated region at position A were larger than those at position B.

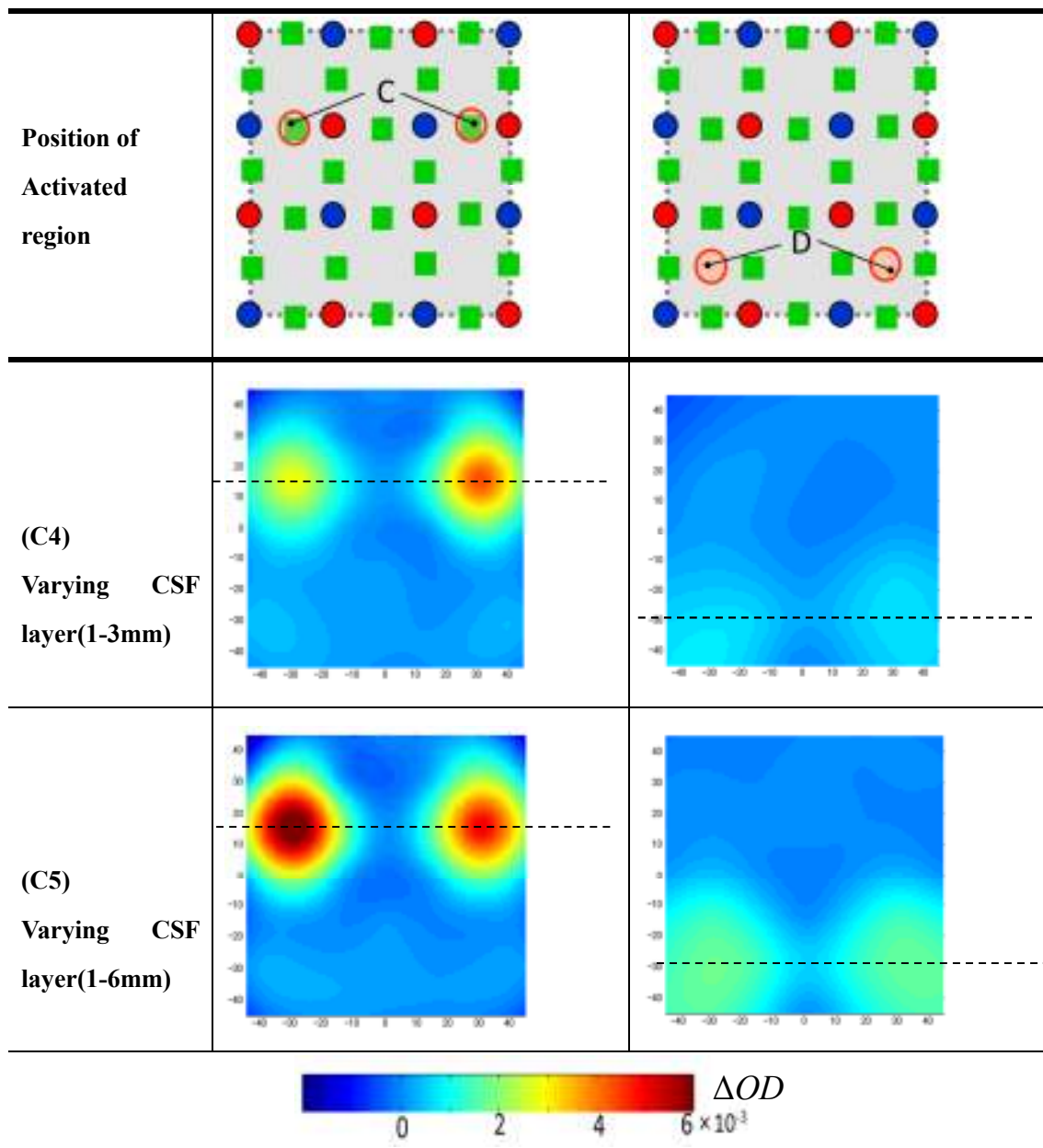


Fig. 4.12: Optical mapping images by the phantom experiments for the cases of linearly varying CSF thickness, (C4) 1 mm - 3mm and (C5) 1 mm - 6 mm with the double activated regions at positions C or D. The dashed lines indicate the horizontal line through the center of the activated region.

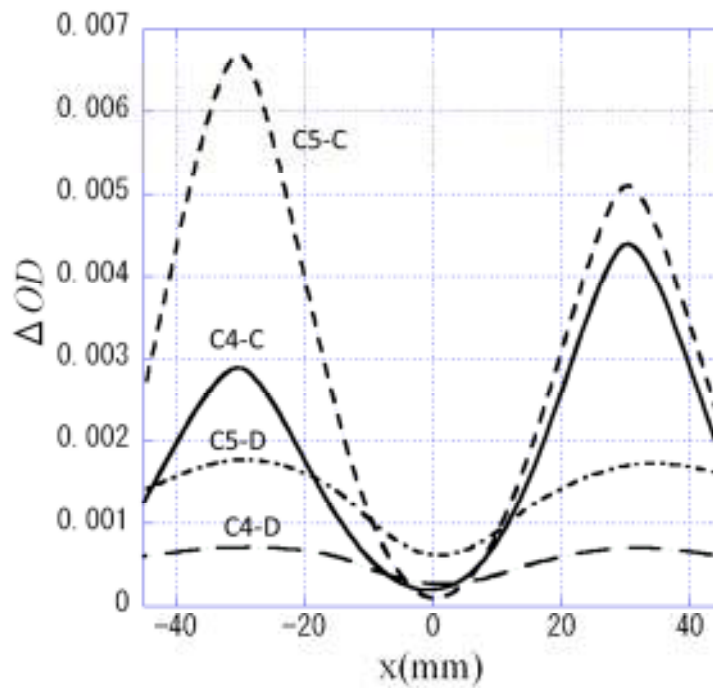


Fig. 4.13: Profile of ΔOD along the dashed lines in Fig. 4.12. (C4-C) varying CSF thickness from 1 mm to 3 mm with the double activated regions at position C, (C5-C) varying CSF thickness from 1 mm to 6 mm with the double activated regions at position C, (C4-D) varying CSF thickness from 1 mm to 3 mm with the double activated regions at position D, and (C5-D) varying CSF thickness from 1 mm to 6 mm with the double activated regions at position D.

Figure 4.12 shows the mapping images for cases of (C4) 1 mm - 3 mm and (C5) 1 mm - 6 mm with the double activated regions existing below the thinner and thicker CSF layer. Both of the double activated regions were located at position C (below the data point) or position D (below the center of the four neighboring data points). Figure 4.13 shows the ΔOD distributions in the x -direction along the dashed lines indicated in Fig. 4.12. For the case of (C4) with the activated regions at position C (curve C4-C in Fig. 4.13), the ΔOD values of the activated region below the thinner CSF layer were smaller than those below the thicker CSF layer. From Fig. 4.11, the ΔOD values were almost the same for the CSF thicknesses of 1 mm and 3 mm. Therefore, the difference observed in the curve C4-C in Fig. 4.13 is contradictory to the results of Fig. 4.11. The

ΔOD values for the case of (C5) with the activated regions at position C (curve C5-C in Fig. 4.13) were about twice those of the curve C4-C. However, the ΔOD values at the thinner CSF layer should be almost the same for C4-C and C5-C, judging from the results of Fig. 4.11. Similarly, for the case of the activated regions at position D, the ΔOD values for the curve C5-D were about twice those of C4-D. These unreasonable results of Figs. 4.12 and 4.13 may have been caused by the experimental difficulties to prepare the phantoms with the linearly varying CSF thickness shown in Fig. 4.4. The phantoms for this experiment should be improved.

4.4 Conclusions

Phantom experiments have been performed to investigate the effect of spatial variation of skull and CSF layer on the optical mapping. The reproducibility of phantom measurement system for optical mapping was confirmed. As the skull thickness increased from 5 mm to 10 and 20 mm, the ΔOD value of brain activity in the mapping images decreased. The ΔOD values of the activated region below the thin skull were significantly greater than those under the thick skull. When the skull thickness was more than 10 mm, the images of the activated region below it were not observable. The ΔOD value increased as the thickness of CSF layer increased from 0 mm to 1 mm. As the thickness of CSF layer increased from 1 mm to 3 mm, the ΔOD value decreased slightly. The ΔOD values of the activated region were dependent on the position of the activated region relative to the data points. The ΔOD values of the activated region below the data point were larger than those below the center of the neighboring four data points. These experimental evidences further support the simulation results in Chap 3.

Chapter 5 Influences of Blood Volume Changes in Cerebrospinal Fluid and Skin Layers on Optical Mapping: Numerical Study

5.1 Introduction

In Chapters 3 and 4, it is revealed that the anatomical variations in the human head such as the variations in the thicknesses of the skull and CSF layers affect the optical mapping images of the activated region. The position of the activated region relative to the data points also influences the mapping images. In the process of generating mapping images, optical mapping assumes that the optical properties of the head tissue are spatially homogeneous and temporally invariable except the activated region in the brain. However, the tissues are actually inhomogeneous and vary hemodynamically. In particular, in the superficial layers above the brain, the existence of the venous vasculature around the CSF layer and the change in the blood volume induced by vasodilation and vasoconstriction in the skin are common phenomena. Actually, the effect of the change in the oxygen saturation in the scalp on NIR signals related to regional cerebral oxygen saturation has been demonstrated [64, 65], and a numerical study [38] has investigated that the existence of extra-cerebral vasculature influences the pathlength of light in the brain and tomography images.

These anatomical and physiological changes due to the intracranial and extracranial blood vessels in the superficial layers should be taken into account because they have great effects on light propagation and mapping images. Optical mapping is sensitive to blood vessels in the superficial tissues which may influence light

propagation in the head and the mapping images. But these influences have not been studied quantitatively so far in optical mapping because *in vivo* experiments are almost impossible.

Numerical simulations of optical mapping in Chap. 3 assume that light absorption in the brain changes only due to brain activation and that the optical properties of the superficial layers remain constant. This chapter focuses on the influences of the existence of a thick blood vessel in the CSF layer and blood volume changes in the skin layer on optical mapping images by numerical simulations. The mapping data, ΔOD , affected by the existence of venous vasculature (sagittal sinus) in the CSF layer and the blood volume changes in the skin layer are analyzed theoretically. The change in the absorption coefficient by vasodilation in the skin layer is estimated from the change in the oxygen saturation and the volume fraction of blood in the skin layer. Three-dimensional head models are constructed to calculate light propagation in the head. The influences on the mapping images are discussed and used to evaluate the mapping images quantitatively.

5.2 Qualitative explanation of the influence of the superficial layers on optical mapping

In Section 2.2, the theory of optical mapping for only absorption changes in the brain is described. In this section, the standard state of the superficial layers with the optical properties in Table 2.1 is considered as the reference state. On the basis of the reference state, the changes in ΔOD due to the existence of a thick blood vessel in the CSF layer and blood flow changes in the skin layer are discussed.

5.2.1 Reference state

The reference state is defined as no additional blood in the skin layer and no blood vessel in the CSF layer. Each layer is expressed by the index i as before shown in Fig.

2.6 (a) and Fig. 5.1,

$i = 1$: Skin layer

$i = 2$: Skull layer

$i = 3$: CSF layer

$i = 4$: Gray matter layer

$i = 5$: White matter layer

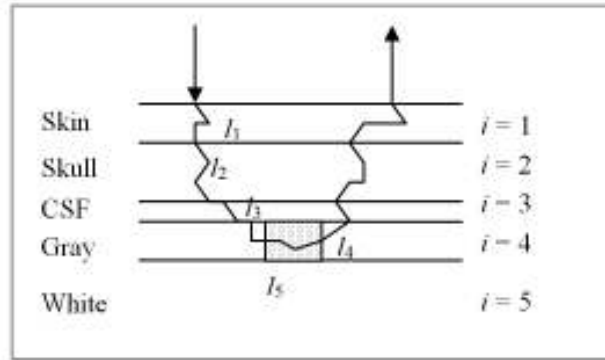


Fig. 5.1: A cross-section of the head model with an activated region in the gray matter and the standard state of the superficial layers.

Here Eqs. (2.16)-(2.19) are rewritten as Eqs. (5.1)-(5.4) in the following

- Rest state

$$OD^n(\lambda) = -\ln \frac{\Phi^n(\lambda)}{\Phi_0(\lambda)} = \sum_{i=1}^5 \left[\left\{ \varepsilon_{HbO_2}(\lambda) C_{HbO_2i}^n + \varepsilon_{Hb}(\lambda) C_{Hbi}^n \right\} l_i + S_i \right] \quad (5.1)$$

- Activated state

$$OD^a(\lambda) = -\ln \frac{\Phi^a(\lambda)}{\Phi_0(\lambda)} = \sum_{i=1}^5 \left[\left\{ \varepsilon_{HbO_2}(\lambda) C_{HbO_2i}^a + \varepsilon_{Hb}(\lambda) C_{Hbi}^a \right\} l_i + S_i \right] \quad (5.2)$$

- Difference between the activated and rest states (ΔOD)

$$\begin{aligned}
\Delta OD(\lambda) &= OD^a(\lambda) - OD^n(\lambda) = -\ln \frac{\Phi^a(\lambda)}{\Phi^n(\lambda)} \\
&= \sum_{i=1}^5 \left\{ \varepsilon_{HbO_2}(\lambda) [C_{HbO_2i}^a - C_{HbO_2i}^n] + \varepsilon_{Hb}(\lambda) [C_{Hbi}^a - C_{Hbi}^n] \right\} l_i \\
&= \sum_{i=1}^5 \left\{ \varepsilon_{HbO_2}(\lambda) \Delta C_{HbO_2i} + \varepsilon_{Hb}(\lambda) \Delta C_{Hbi} \right\} l_i
\end{aligned} \tag{5.3}$$

No change in the blood concentration is assumed when the brain is activated from the rest state, and $\Delta C_{HbO_2i} = \Delta C_{Hbi} = 0$ ($i = 1, 2, 3, 5$) except in the gray matter layer. Therefore, only the terms for $i = 4$ remain,

$$\begin{aligned}
\Delta OD(\lambda) &= \left\{ \varepsilon_{HbO_2}(\lambda) \Delta C_{HbO_2,4} + \varepsilon_{Hb}(\lambda) \Delta C_{Hb4} \right\} l_4 \\
&= \left\{ \varepsilon_{HbO_2}(\lambda) \Delta C_{HbO_2,G} + \varepsilon_{Hb}(\lambda) \Delta C_{HbG} \right\} l_G \quad (i = 4 = G)
\end{aligned} \tag{5.4}$$

5.2.2 Existence of blood vessel in the CSF layer

In the case of existence of a thick blood vessel in the CSF layer as shown in Fig. 5.2, the effective pathlength is assumed not to change for $i = 1, 2$ and to change for the layers $i = 3, 4, 5$ from the reference state. In particular, the change for the layer $i = 3$ will be large and the changes for the layers $i = 4, 5$ will be small. By indicating the effective pathlength of each layer by l_{vi} when a thick blood vessel exists in the CSF layer, the comparison of l_{vi} with l_i for no blood vessel in the CSF layer can be expressed as the following,

$$l_{v1} \approx l_1, l_{v2} \approx l_2, l_{v3} \ll l_3, l_{v4} < l_4, l_{v5} < l_5. \tag{5.5}$$

Actually, the venous blood vessel, e.g., sagittal sinus, exists in the dura mater, and in this study it is assumed that the sagittal sinus is located in the CSF layer.

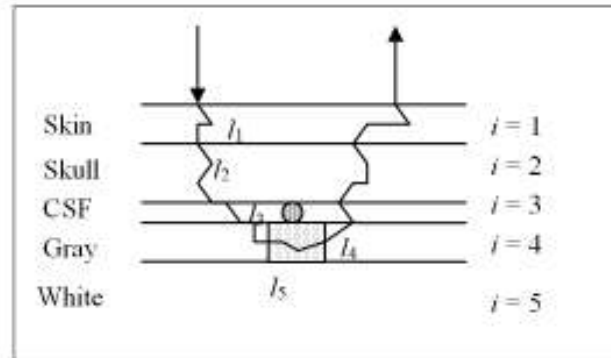


Fig. 5.2: A cross-section of the head model indicating a thick blood vessel existing in the CSF layer and an activated region in the gray matter layer.

By using a subscript “v” to indicate the existence of a thick blood vessel in the CSF layer, OD_v at the rest and activated states with a blood vessel in the CSF layer are given by,

- Rest state:

$$OD_v^n(\lambda) = -\ln \frac{\Phi^n(\lambda)}{\Phi_0(\lambda)} = \sum_{i=1}^5 \left[\left\{ \varepsilon_{HbO_2}(\lambda) C_{HbO_2i}^n + \varepsilon_{Hb}(\lambda) C_{Hbi}^n \right\} l_{vi} + S_i \right] \quad (5.6)$$

- Activated state:

$$OD_v^a(\lambda) = -\ln \frac{\Phi^a(\lambda)}{\Phi_0(\lambda)} = \sum_{i=1}^5 \left[\left\{ \varepsilon_{HbO_2}(\lambda) C_{HbO_2i}^a + \varepsilon_{Hb}(\lambda) C_{Hbi}^a \right\} l_{vi} + S_i \right] \quad (5.7)$$

Here, the effective pathlength of each layer l_{vi} at the activated state is assumed to be equal to that at the rest state, and again the scattering terms, S_i , are assumed not to change.

- Difference between the activated and rest state (ΔOD_v):

$$\begin{aligned}
\Delta OD_v(\lambda) &= OD_v^a(\lambda) - OD_v^n(\lambda) = -\ln \frac{\Phi^a(\lambda)}{\Phi^n(\lambda)} \\
&= \sum_{i=1}^5 \left\{ \varepsilon_{HbO_2}(\lambda) [C_{HbO_2i}^a - C_{HbO_2i}^n] + \varepsilon_{Hb}(\lambda) [C_{Hbi}^a - C_{Hbi}^n] \right\} l_{vi} \\
&= \sum_{i=1}^5 \left\{ \varepsilon_{HbO_2}(\lambda) \Delta C_{HbO_2i} + \varepsilon_{Hb}(\lambda) \Delta C_{Hbi} \right\} l_{vi}
\end{aligned} \tag{5.8}$$

Except in the gray matter layer, no change in the blood concentration is assumed when the brain is activated from the rest state, and $\Delta C_{HbO_2i} = \Delta C_{Hbi} = 0$ ($i = 1, 2, 3, 5$). Therefore, only the terms for $i = 4$ remain.

$$\begin{aligned}
\Delta OD_v(\lambda) &= \left\{ \varepsilon_{HbO_2}(\lambda) \Delta C_{HbO_2,4} + \varepsilon_{Hb}(\lambda) \Delta C_{Hb4} \right\} l_{v4} \\
&= \left\{ \varepsilon_{HbO_2}(\lambda) \Delta C_{HbO_2,G} + \varepsilon_{Hb}(\lambda) \Delta C_{HbG} \right\} l_{vG} \quad (i = 4 = G) \\
&< \left\{ \varepsilon_{HbO_2}(\lambda) \Delta C_{HbO_2,G} + \varepsilon_{Hb}(\lambda) \Delta C_{HbG} \right\} l_G \\
&= \Delta OD(\lambda) \text{ (at the reference state)}
\end{aligned} \tag{5.9}$$

The inequality comes from Eq. (5.5).

5.2.3 Blood volume changes in the skin layer

When the blood flow changes in the skin layer ($i = 1$) are induced by vaso-dilation or vaso-constriction, it is clear that the effective pathlength in the skin layer l_{s1} is different from the effective pathlength l_1 for the reference state. In the layers below the skin layer ($i = 2, 3, 4, 5$), it is not clear whether the effective pathlengths l_{si} are different from l_i for the reference state. However, it is reasonable to assume that l_{si} ($i = 2, 3, 4, 5$) are almost the same as l_i . Thus, the followings are derived,

$$l_{s1} \neq l_1, l_{s2} \approx l_2, l_{s3} \approx l_3, l_{s4} \approx l_4, l_{s5} \approx l_5 \tag{5.10}$$

Blood in the skin layer is assumed homogeneously distributed in the skin layer. In order to study the effect of the changes in the blood volume in the skin, which occurs simultaneously with the brain activation, the rest state in the gray matter with the normal blood volume in the skin is considered as the reference state, and the activated

state in the gray matter is accompanied with the blood volume change in the skin.

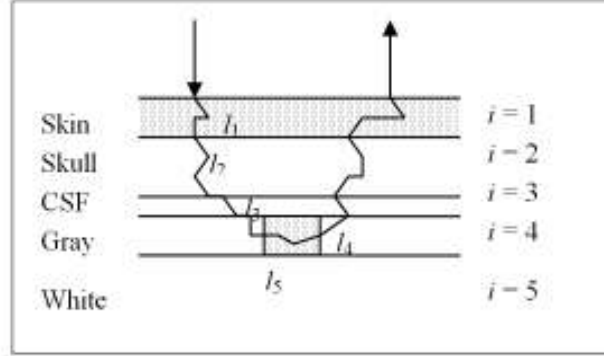


Fig. 5.3: A cross- section of head model indicating blood flow changes in the skin layer and an activated region in the gray matter layer.

The optical densities in the case of the blood volume change in the skin, ΔOD_s , are given as the following.

- Rest state with normal blood volume in the skin:

$$OD_s^n(\lambda) = -\ln \frac{\Phi^n(\lambda)}{\Phi_0(\lambda)} = \sum_{i=1}^5 \left[\left\{ \varepsilon_{HbO_2}(\lambda) C_{HbO_2}^n + \varepsilon_{Hb}(\lambda) C_{Hb}^n \right\} l_i + S_i \right] \quad (5.11)$$

- Activated state with the blood volume change in the skin:

$$OD_s^a(\lambda) = -\ln \frac{\Phi^a(\lambda)}{\Phi_0(\lambda)} = \sum_{i=1}^5 \left[\left\{ \varepsilon_{HbO_2}(\lambda) C_{HbO_2}^a + \varepsilon_{Hb}(\lambda) C_{Hb}^a \right\} l_{si} + S_i \right] \quad (5.12)$$

- Difference between the activated and rest states (ΔOD_s) assuming no change in the blood concentration in the layers $i=2, 3, 5$, and no change in scattering:

$$\begin{aligned} \Delta OD_s(\lambda) &= OD_s^a(\lambda) - OD_s^n(\lambda) = -\ln \frac{\Phi^a(\lambda)}{\Phi^n(\lambda)} \\ &= \varepsilon_{HbO_2}(\lambda) (C_{HbO_2}^a l_{s1} - C_{HbO_2}^n l_1) + \varepsilon_{HbO_2}(\lambda) \Delta C_{HbO_2} l_4 \\ &\quad + \varepsilon_{Hb}(\lambda) (C_{Hb}^a l_{s1} - C_{Hb}^n l_1) + \varepsilon_{Hb}(\lambda) \Delta C_{Hb} l_4 \end{aligned} \quad (5.13)$$

By comparing Eqs. (5.4), (5.9) and (5.13), it can be seen that the existence of blood vessel in the CSF layer and the blood volume change in the skin layer change the

effective pathlength of light propagation between the source and detector pair. Consequently, the changes in the effective pathlength influence the values of the ΔOD and the mapping images of the activated region.

5.3 Estimation of the absorption coefficient in the skin layer with increased blood volume

This section is to estimate the variation of μ_a with hemodynamic changes in the skin layer. The skin layer is divided into two parts as epidermis and dermis. The values of μ_a and μ_s' of the epidermis are assumed to remain the same as $\mu_a = 0 \text{ mm}^{-1}$ and $\mu_s' = 0.085 \text{ mm}^{-1}$, even with the blood volume changes in the skin layer. However, the value of μ_a of the dermis is expected to change responding to the blood volume changes in the skin by vasodilation. It is assumed that the variation of the physiological state in the skin layer hardly affect the scattering properties of the tissues, thus the μ_s' of the dermis is fixed as $\mu_s' = 0.073 \text{ mm}^{-1}$. In the following, μ_a values of the dermis with the normal and increased blood volumes are estimated.

(1) Dermis layer with the normal blood volume:

When the blood volume in the skin is at the normal state the absorption coefficient of the dermis, μ_a^n , is given as

$$\mu_a^n = (1 - f_v^n) \mu_{a-t} + f_v^n \mu_{a-b}^n \quad (5.14)$$

where f_v^n is the normal blood volume fraction, μ_{a-t} is the absorption coefficient of the dermis tissue excluding blood, and μ_{a-b}^n is the absorption coefficient of blood at the normal blood volume in the skin. The superscript “n” indicates the normal blood volume. According to the baseline optical properties of the skin layer (see Table. 2.1), the absorption coefficient of the dermis layer with the normal blood volume is $\mu_a^n = 0.030 \text{ mm}^{-1}$.

- Absorption coefficient of blood when blood is at the normal state, μ_{a-b}^n , is given as

$$\begin{aligned}\mu_{a-b}^n &= \mu_{Hb}^n + \mu_{HbO_2}^n = \varepsilon_{Hb} \cdot C_{Hb}^n + \varepsilon_{HbO_2} \cdot C_{HbO_2}^n \\ &= \varepsilon_{Hb}(1 - SO_2^n)C_{Hb+HbO_2}^n + \varepsilon_{HbO_2}SO_2^n C_{Hb+HbO_2}^n\end{aligned}\quad (5.15)$$

Note that $C_{Hb}^n = (1 - SO_2^n)C_{Hb+HbO_2}^n$, $C_{HbO_2}^n = SO_2^n C_{Hb+HbO_2}^n$, where the subscripts ‘‘Hb’’ and ‘‘HbO₂’’ denote deoxy- and oxy-hemoglobin, respectively, and SO_2 is the oxygen saturation of blood given by Eq. (5.16).

$$SO_2 = \frac{C_{HbO_2}}{C_{Hb} + C_{HbO_2}} \quad (5.16)$$

The parameters of ε , SO_2 , and C are given by the following

- Molar extinction coefficient, ε [66]

By using the wavelength of 805nm which is the isobestic point of absorption of oxy- and deoxy-hemoglobin, $\varepsilon_{Hb} = \varepsilon_{HbO_2} = 0.080 \text{ [mm}^{-1} \cdot \text{mM}^{-1}]$ is given.

- Oxygen saturation of blood SO_2

The oxygen saturation of blood can be given as $SO_2^n = 0.70$ when blood is at the normal state[64, 65].

- Molar concentrations of oxy- and deoxy-hemoglobin, C

Hematocrit (Hct) is the volume fraction of red blood cells in blood and normally Hct = 40%. The density of hemoglobin is 0.335 kg/L, the molecular weights of oxy- and deoxy-hemoglobin are the same 64500 g/mol = 64.5 kg/mol [67]. Then the molar concentration of hemoglobin in a whole blood of 1 liter is

$$\begin{aligned}C_{Hb+HbO_2} &= \frac{0.40L_{RBC}/L_{WB} \times 0.335\text{kg} / L_{RBC}}{64.5\text{kg/mole}_{Hb}} \\ &= 0.0021 \text{ mole}_{Hb} / L_{WB} = 2.1 \text{ mM}\end{aligned}\quad (5.17)$$

- molar concentration of deoxy-hemoglobin

$$C_{Hb}^n = (1 - SO_2^n) \cdot C_{Hb+HbO_2} = 0.3 \times 2.1 = 0.63 \text{ mM} \quad (5.18)$$

- molar concentration of oxy-hemoglobin

$$C_{HbO_2}^n = SO_2^n \cdot C_{Hb+HbO_2} = 0.7 \times 2.1 = 1.47 \text{ mM} \quad (5.19)$$

Then the absorption coefficients of blood in the skin layer with the normal and increased blood volumes are calculated as,

$$\left. \begin{aligned} \mu_{Hb}^n &= \varepsilon_{Hb} \cdot C_{Hb}^n = 0.080 \times 0.63 = 0.051 \text{ mm}^{-1} \\ \mu_{HbO_2}^n &= \varepsilon_{HbO_2} \cdot C_{HbO_2}^n = 0.080 \times 1.47 = 0.118 \text{ mm}^{-1} \\ \mu_{a-b}^n &= \mu_{Hb}^n + \mu_{HbO_2}^n = 0.051 + 0.1176 = 0.169 \text{ mm}^{-1} \end{aligned} \right\} \quad (5.20)$$

The normal blood volume fraction is assumed as $f_v^n = 0.10$ [68, 69]. From the values of $\mu_a^n = 0.030 \text{ mm}^{-1}$ and $\mu_{a-b}^n = 0.169 \text{ mm}^{-1}$ and $f_v^n = 0.10$, the absorption coefficient of the dermis tissue excluding blood is determined as $\mu_{a-t} = 0.015 \text{ mm}^{-1}$ using Eq. (5.14).

(2) Dermis layer with the increased blood volume:

When the blood volume in the skin increases the absorption coefficient of the dermis, μ_a^a , is given as

$$\mu_a^a = (1 - f_v^a) \mu_{a-t} + f_v^a \mu_{a-b}^a \quad (5.21)$$

where f_v^a is the increased blood volume fraction, and μ_{a-b}^a is the absorption coefficient of blood at the increased blood volume in the skin. The superscript “a” indicates the increased blood volume. Two cases of the increased blood volume fractions are assumed as $f_v^{a1} = 0.14$ and $f_v^{a2} = 0.18$ from the normal blood volume fraction of $f_v^n = 0.10$.

Because the isosbestic point of 805nm is used, the absorption coefficient of blood

μ_{a-b} is dependent only hematocrit and is independent of the blood volume in the dermis. It is reasonable to assume that the hematocrit is constant, and therefore $\mu_{a-b}^a = \mu_{a-b}^n = 0.169 \text{ mm}^{-1}$ from Eq. (5.20).

Now the volume fraction, f_v^a , and the absorption coefficients of tissue and blood, μ_{a-b}^t and μ_{a-b}^a , are known, the absorption coefficients of the skin layer with the increased blood volumes are estimated as the following,

$$\mu_a^{a1} = (1 - f_v^{a1})\mu_{a-t} + f_v^{a1}\mu_{a-b}^{a1} = (1 - 0.14) \times 0.015 + 0.14 \times 0.169 = 0.037 \text{ mm}^{-1} \quad (5.22)$$

$$\mu_a^{a2} = (1 - f_v^{a2})\mu_{a-t} + f_v^{a2}\mu_{a-b}^{a2} = (1 - 0.18) \times 0.015 + 0.18 \times 0.169 = 0.043 \text{ mm}^{-1} \quad (5.23)$$

Table 5.1 summarizes the parameters. Considering the volume fraction of blood in the dermis layer, the values of μ_a of the dermis with normal, increased blood volumes 0.14% and 0.18% are 0.030, 0.037 and 0.043 mm^{-1} , respectively.

Table 5.1 The optical properties of the dermis layer with blood volume changes.

Case	Blood volume fraction, f_v	μ_a [mm^{-1}]	μ_s' [mm^{-1}]
(1) Normal blood volume	0.10 (10%)	0.030	0.073
(2) Increased blood volume I	0.14 (14%)	0.037	0.073
(3) Normal blood volume II	0.18 (18%)	0.043	0.073

5.4 Models of human head with activated region, blood vessel in the CSF and blood volume changes in the skin

The basic simulation model of the human head for optical mapping in this chapter is shown in Fig. 5.4. As before, the head model consists of five layers, skin, skull, CSF, gray matter and white matter layers. When the brain is activated, an activated region (a disk with a diameter of 15mm and a height of 3.5mm) is assumed to exist in the gray matter with a higher absorption coefficient than that of the surrounding brain tissues.

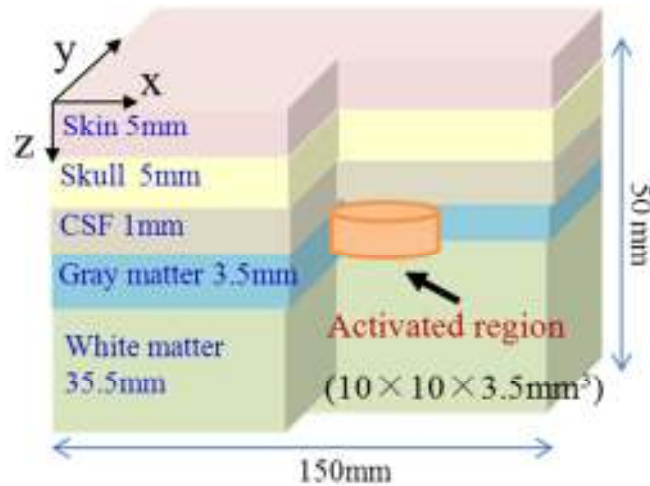


Fig. 5.4: The simulation model of the human head for optical mapping with an activated disk region.

5.4. 1 Blood vessel in the CSF layer

As shown in Fig. 1.2, a thick venous blood vessel, e.g., sagittal sinus, is in the dura mater. Although dura mater has the irregular surface, the sagittal sinus is assumed to exist as a thick venous blood vessel in the CSF layer for simplicity in the simulation. The blood vessel in the CSF layer has a baseline scattering coefficient of $\mu_s' = 3.69 \text{ mm}^{-1}$. While μ_a of the vessel varies with the vessel dynamics, μ_s' of the vessel is assumed to remain the same.

To investigate how the existence of a thick venous blood vessel in the CSF layer affect the optical mapping images of activated regions in the gray matter, five cases are considered, case (C1) with no blood vessel in the CSF layer, case (C2) with a 1 mm-side square blood vessel having μ_a of 0.13 mm^{-1} in the CSF layer, case (C3) with a 1

mm-side square blood vessel having μ_a of 0.26 mm^{-1} in the CSF layer, case (C4) with a $1 \text{ mm} \times 2 \text{ mm}$ rectangular blood vessel having μ_a of 0.13 mm^{-1} in the CSF layer, and case (C5) with a $1 \text{ mm} \times 2 \text{ mm}$ rectangular blood vessel having μ_a of 0.26 mm^{-1} in the CSF layer as listed in Table 5.2. In all cases from C1 to C5, the blood vessels are all located above the center of the activated region.

Table 5.2 Cases of a thick blood vessel existing in the CSF layer

Case	Shape of the thick blood vessel	μ_a of the blood vessel (mm^{-1})
C1	No thick blood vessel	---
C2	1 mm-side square	0.13
C3	1 mm-side square	0.26
C4	$1 \text{ mm} \times 2 \text{ mm}$ rectangle	0.13
C5	$1 \text{ mm} \times 2 \text{ mm}$ rectangle	0.26

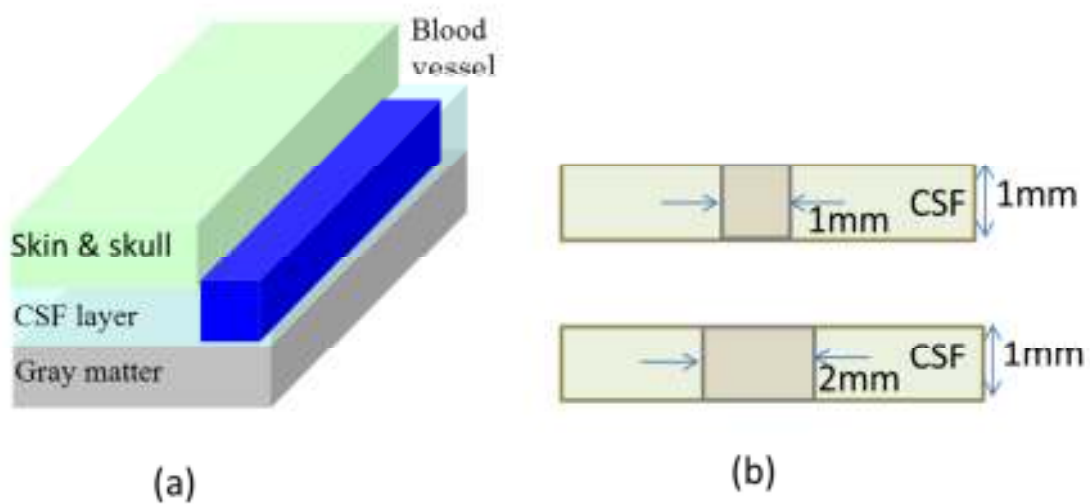


Fig. 5.5: (a) The blood vessel model in the CSF layer, and (b) the cross-section of the CSF layer with a thick blood vessel.

5.4. 2 Blood volume changes in the skin layer

To study how the blood volume changes in the skin layer influences the mapping images, the skin layer is divided into two parts as epidermis and dermis (see Fig. 5.6.). The optical properties of epidermis are assumed to be unchanged as given in the first paragraph of Section 5.3. Blood is homogeneously distributed in the dermis with a varying volume fraction, f_v , and the change in the blood flow is represented by the changes in the blood volume fraction which result in the change in the absorption coefficient of the dermis as described in Section 5.3.

Based on Table 5.1, three cases are assumed; i.e., case (S1) where μ_a of the dermis, μ_{a-skin} , is 0.030 mm^{-1} for the normal blood volume f_v of 10% , case (S2) where μ_{a-skin} is 0.037 mm^{-1} for the increased f_v of 14%, and case (S3) where μ_{a-skin} is 0.043 mm^{-1} for the increased f_v of 18% in the dermis as listed in Table 5.3. The standard optical properties of other layers and activated region at the wavelength of 805 nm are given as in Table 2.1. Note that f_v and μ_{a-skin} are kept constant while the brain is activated from the rest state.

Table 5.3 Cases of blood volume changes in the dermis layer

Case	Blood volume	Blood volume fraction, f_v	μ_a of the dermis layer, $\mu_{a-skin} (\text{mm}^{-1})$
S1	Normal blood volume	0.10 (10%)	0.030
S2	Increased blood volume I	0.14 (14%)	0.037
S3	Normal blood volume II	0.18 (18%)	0.043

In this study, the thickness of the epidermis and dermis in the model are given as 1.0 mm and 4.0 mm, respectively, although their actual thicknesses are in the range of 0.1 ~ 0.2 mm and 2.0 ~ 3.0 mm, respectively. Due to the limitation of using a very thin plastic plate for simulating the epidermis in the experiment, 1.0 mm was the smallest thickness prepared for the phantom experiments. In order to match the conditions for simulations and phantom experiments, the thickness of 1.0 mm was employed for the simulation model, too. In the phantom experiments, the changes in the blood volume

fraction were achieved by exchanging the dermis layer with high or low μ_a as shown in Fig. 5.6.

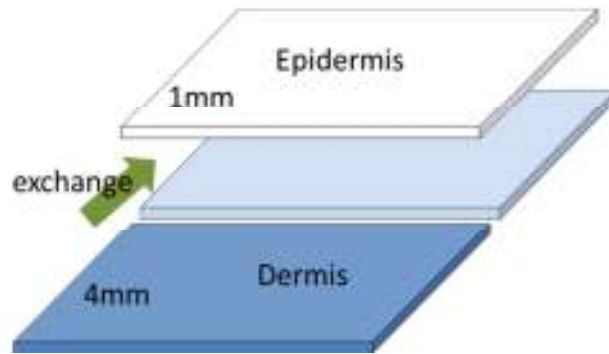


Fig. 5.6: The skin layer model of the epidermis (1.0 mm) and dermis (4.0 mm). The dermis layer is exchangeable with the layers having different absorption coefficients.

5.5 Results

5.5.1 Influence of the blood vessel in the CSF layer on mapping images

5.5.1.1 The effect of the shape and μ_a of the blood vessel

Fig. 5.7 (A) shows the simulation results of the mapping images for case (C1) without a thick blood vessel, and Fig. 5.7 (B) to (E) for cases (C2) to (C5) with a thick blood vessel indicated by vertical lines. The color bar shows the value of ΔOD . The mapping images show the distributions of $24-\Delta OD$ after spline interpolation. Comparing to case (C1) without a vessel, the existence of the vessel, cases (C2), (C3), (C4) and (C5), reduce the ΔOD values of the brain activity in the mapping images. When μ_a of the blood vessel increases from 0.13 mm^{-1} for case (C2) to 0.26 mm^{-1} for case (C3) with the same 1 mm-side square vessel, the ΔOD values of the brain activity reduce. Keeping μ_a constant as 0.26 mm^{-1} , the ΔOD values of case (C5) with the 1

mm \times 2 mm rectangular blood vessel decrease from those in case (C3) with the 1 mm-side square blood vessel.

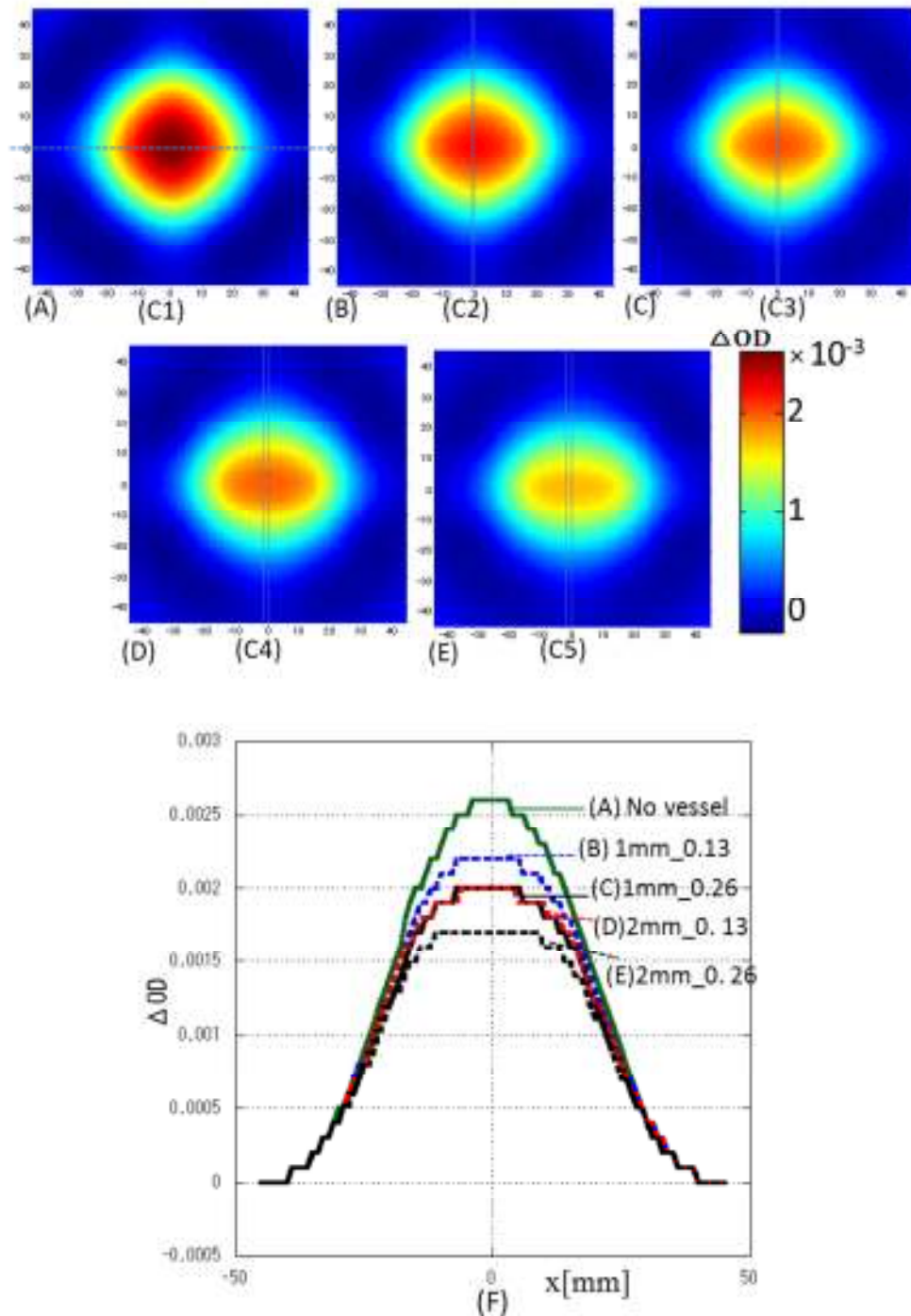


Fig. 5.7: The simulation results of mapping images with or without a blood vessel in the CSF layer. (A)-(E) simulated mapping images of cases (C1)-(C5). (F) the profiles of ΔOD along the horizontal lines (indicated by the blue dashed lines in image (A)) through the center of the activated region.

In addition, with the approximately equal hemoglobin content in the blood vessel for cases (C3) and (C4), the mapping images are almost the same. This results show that the effect of blood vessel in CSF layer on mapping images is dependent on the whole hemoglobin content.

To show the effect clearly, Fig. 5.7 (F) displays the lateral profiles of ΔOD along the horizontal lines through the centers of the activated region as indicated by the blue dashed line in Fig. 5.7(A). ΔOD for case (C1) is the largest among all the cases. Increasing both the absorption coefficient and size of the vessel decreases the value of ΔOD .

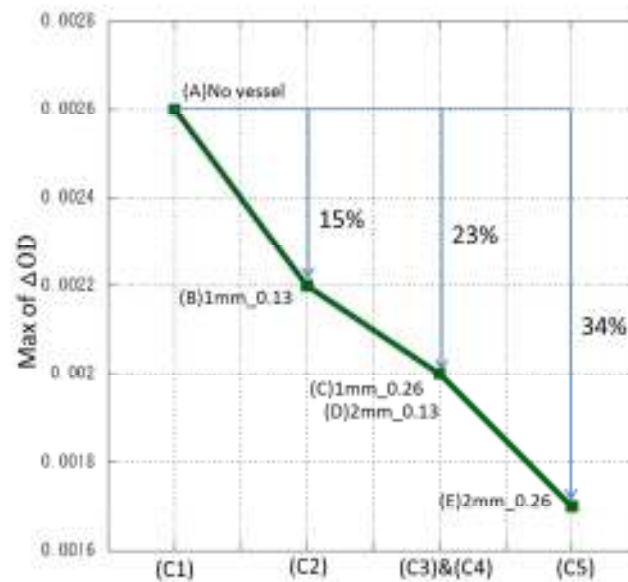


Fig. 5.8: The maximum of ΔOD to the profiles of ΔOD along the horizontal lines through the center of the activated region as for Fig. 5.7 (F).

The results also revealed that the existence of a blood vessel above the center of the activated region hardly affects the spatial distribution of ΔOD for the activated region, but the magnitude of ΔOD decreases significantly. Fig. 5.8 plots the maxima of ΔOD in Fig. 5.7 (F). The maxima of ΔOD for cases (C2), (C3)&(C4), and (C5) decrease 15%, 23% and 34% from that for case (C1).

It can be said that the existence of a blood vessel in the low-scattering and

low-absorbing CSF layer affects light propagation through the gray matter. If μ_a of the blood vessel increases by some reasons, the probability of light passing through the gray matter decreases, therefore resulting in the decrease in the value of ΔOD for brain activation.

5.5.1.2 The effect of the distance between the activated region and the blood vessel in the CSF layer

So far, the blood vessel in the CSF layer is located above the center of the activated region. Actually, however, the venous vasculature is distributed randomly over the cerebral cortex. To mimic this situation, the distance between the center of the activated region and the vessel is changed from $d = 0$ mm to $d = 5$ mm, 10 mm, 15 mm and 20 mm.

Figure 5.9 (A) illustrates the top view of the head model showing the distance between the activated region and square vessel, d , and Fig. 5.9 (B) shows the ΔOD profiles along the horizontal line shown in Fig. 5.9 (A) as a function of the distance, d , for the square vessel with the size of 1 mm-side having μ_a of 0.26 mm^{-1} , and Fig. 5.9 (C) shows those for the rectangular vessel with the size of 1 mm \times 2 mm having μ_a of 0.26 mm^{-1} . Figure 5.9 (B) and (C) show a similar trend of ΔOD profiles with the increase in the distance, d . When the vessels are right above the center of the activated region, the influence is the maximum. The influence decreases with the increase in the distance, and when the distance is larger than 15 mm, there is almost no effect of the thick blood vessel on the optical mapping images. With a larger rectangular vessel with the size of 1 mm \times 2 mm, the magnitude of the change in ΔOD is larger. The asymmetry of the profile for the rectangular vessel with $d = 0$ mm may be caused by a numerical error.

These results demonstrate that the influence of thick blood vessels in the CSF layer on optical mapping images of activated regions is dependent on the distance between the activated region and the vessels.

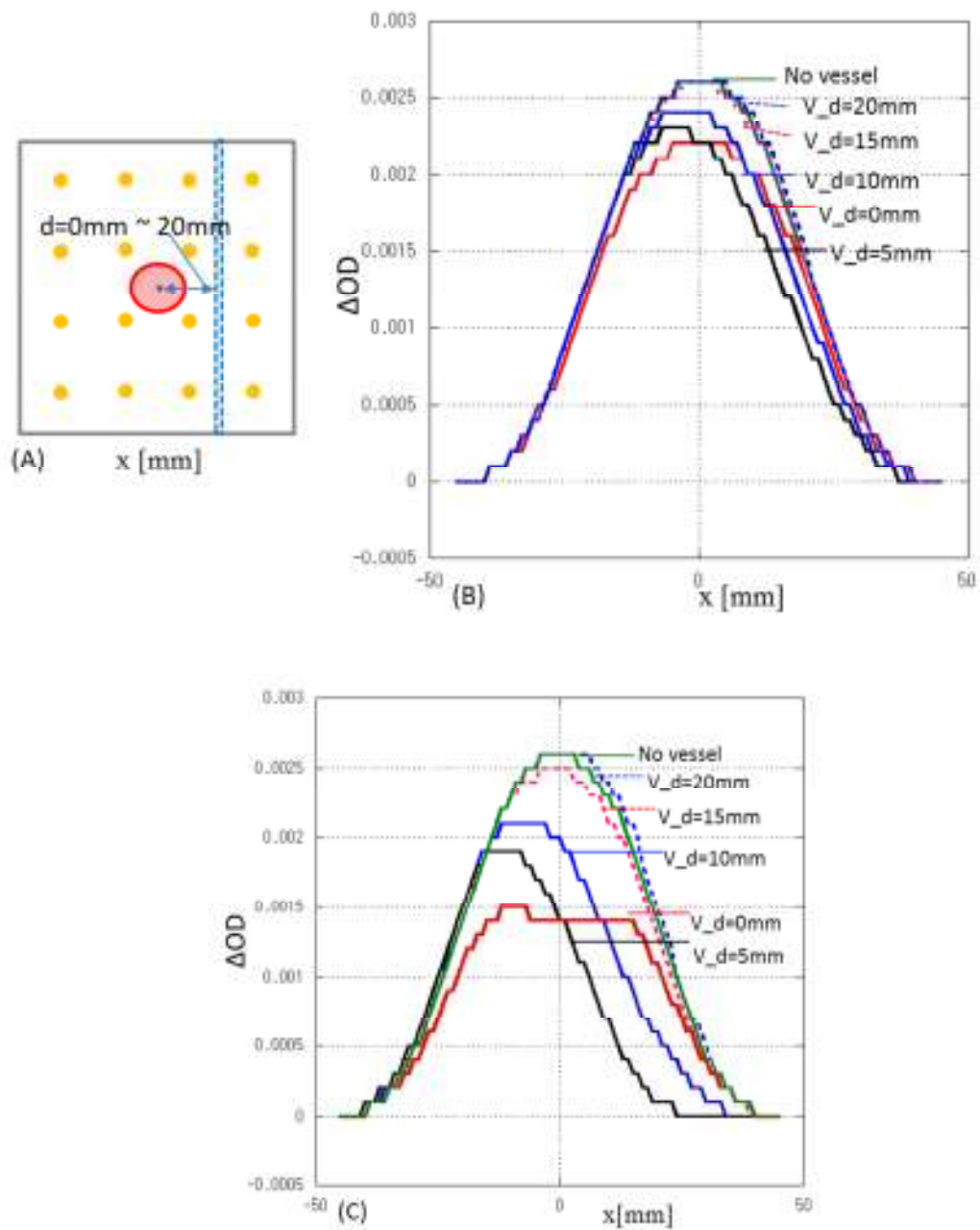


Fig. 5.9: (A) Top view of the head model shows the distance between the activated region and the square vessel. The profiles of ΔOD along the horizontal line through the center of the activated regions a function of the distance between the activated region and (B) the square vessel with the size of 1 mm-side having μ_a of 0.26 mm^{-1} , and (C) the rectangular vessel with the size of 1 mm x 2 mm having μ_a of 0.26 mm^{-1} .

5.5.2 Influence of the blood volume changes in the skin layer on mapping images

Figure 5.10 (A), (B) and (C) show the simulation results of the mapping images for cases (S1), (S2) and (S3) where μ_a of the dermis layer, μ_{a-skin} , changes. Comparing with case (S1) with the normal blood volume in the skin layer, ΔOD increases for cases (S2) and (S3) where the blood volume fraction, f_v , increases. As the blood volume in the skin layer increases, μ_{a-skin} increases from case (S2) to case (S3), and the value of ΔOD increases.

Figure 5.10 (D) shows the profiles of ΔOD along the horizontal lines through the center of the activated region. The peak values of ΔOD increase with the increase in μ_{a-skin} in the skin layer. Figure 5.10 (E) displays the maximum ΔOD as a function of μ_{a-skin} . Comparing with the case of the normal blood volume in the skin layer $\mu_{a-skin} = 0.030 \text{ mm}^{-1}$, the maximum ΔOD increases 10% and 19% for $\mu_{a-skin} = 0.037 \text{ mm}^{-1}$ and $\mu_{a-skin} = 0.043 \text{ mm}^{-1}$, respectively.

The simulation results show that the mapping images have a strong dependency on the change in the blood volume fraction in the skin layer. The increase in μ_{a-skin} induced by the increase in f_v increases the value of ΔOD of the brain activity in the gray matter.

These results are contrary to those of simulation for the blood vessel in the CSF layer and look unreasonable intuitively because light penetration to the deeper tissues is blocked by higher absorption of the skin layer.

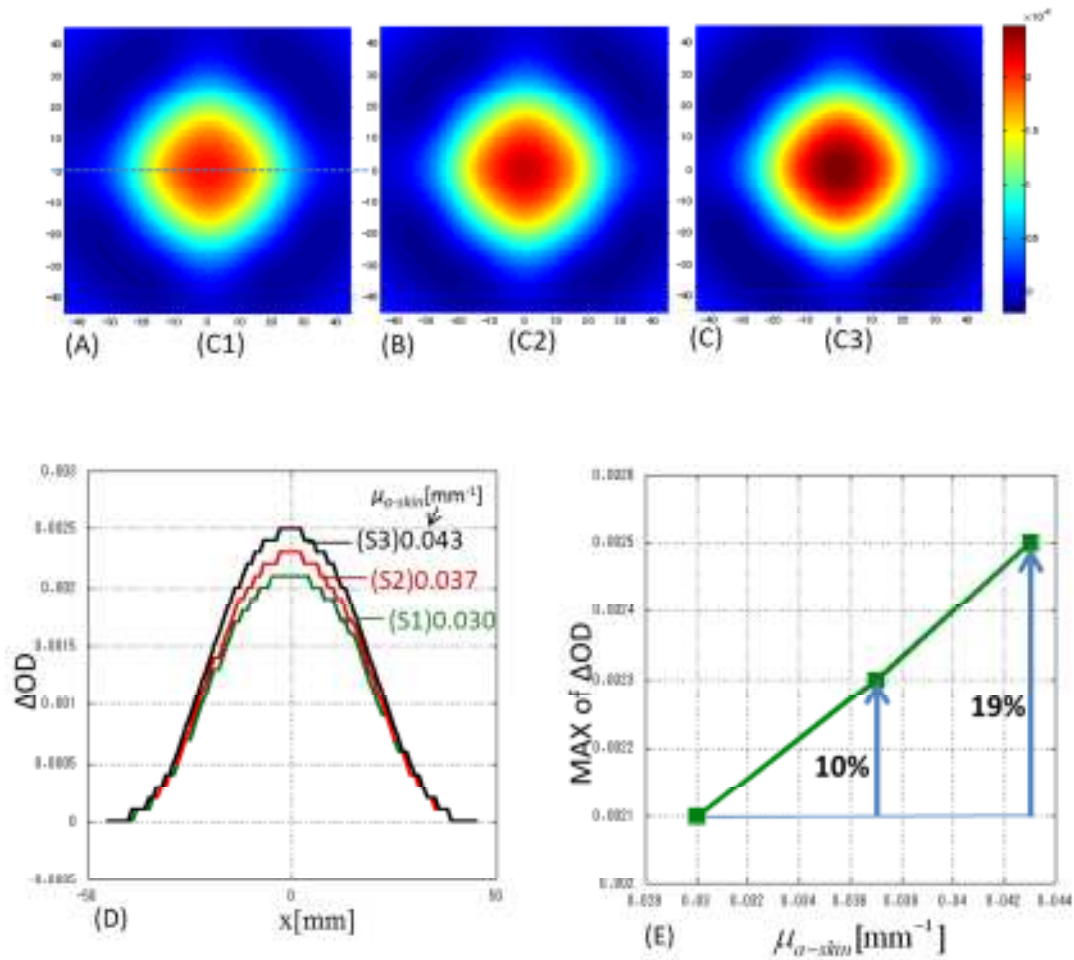


Fig. 5.10: The simulation results of the mapping images for cases (S1), (S2) and (S3) where μ_{a-skin} of the dermis layer changes.

In order to understand these results, Φ^n and Φ^a measured at the 24 data points are plotted in Fig. 5.11(A), and $\Delta OD = \ln(\Phi^n / \Phi^a)$ in Fig. 5.11(B) for the three cases (S1), (S2) and (S3). The abscissa corresponds to the number of the data points shown in Fig. 2.7. As seen from Fig. 5.11(A), the differences between Φ^n and Φ^a with the same μ_{a-skin} are very small compared to their magnitudes, and Φ^n and Φ^a look almost the same although their magnitudes greatly decrease with the increase in μ_{a-skin} . However, Fig. 5.11(B) shows that ΔOD values showing the brain activation (data points, No.9, 12, 13, and 16) increases with the increase in μ_{a-skin} resulting in the higher sensitivity of the mapping images to the brain activation.

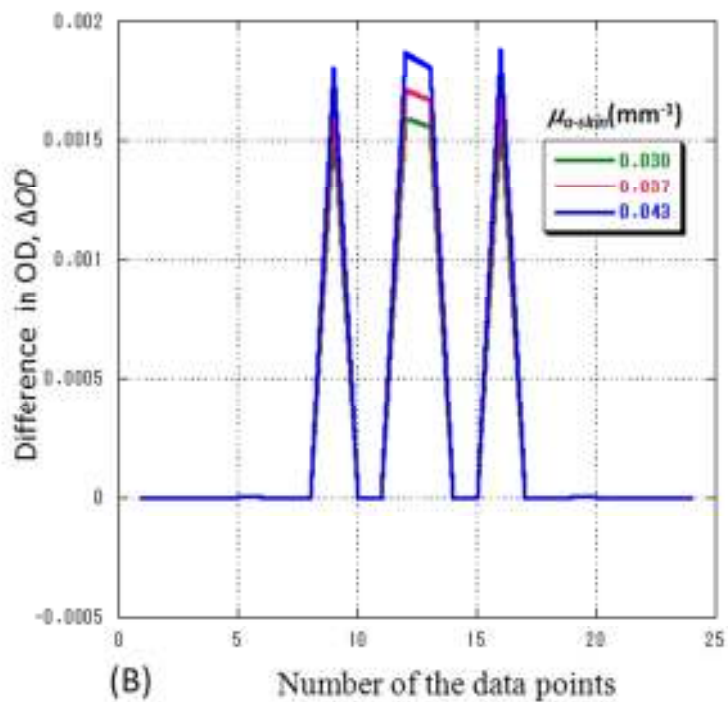
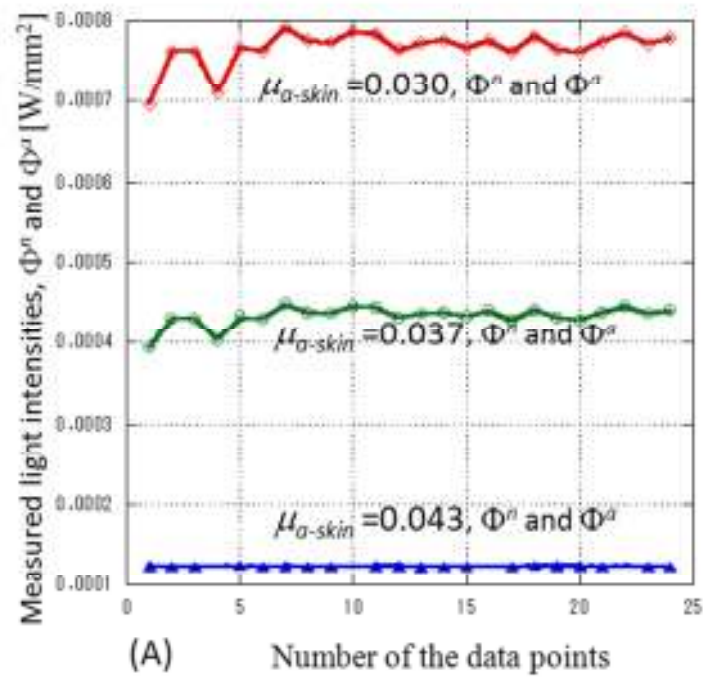


Fig. 5.11: (A) The measured light intensities, Φ^n and Φ^a , and (B) OD at the 24 data points for three cases of different μ_a of dermis layer. Superscripts “ a ” and “ n ” indicate the activated and rest states.

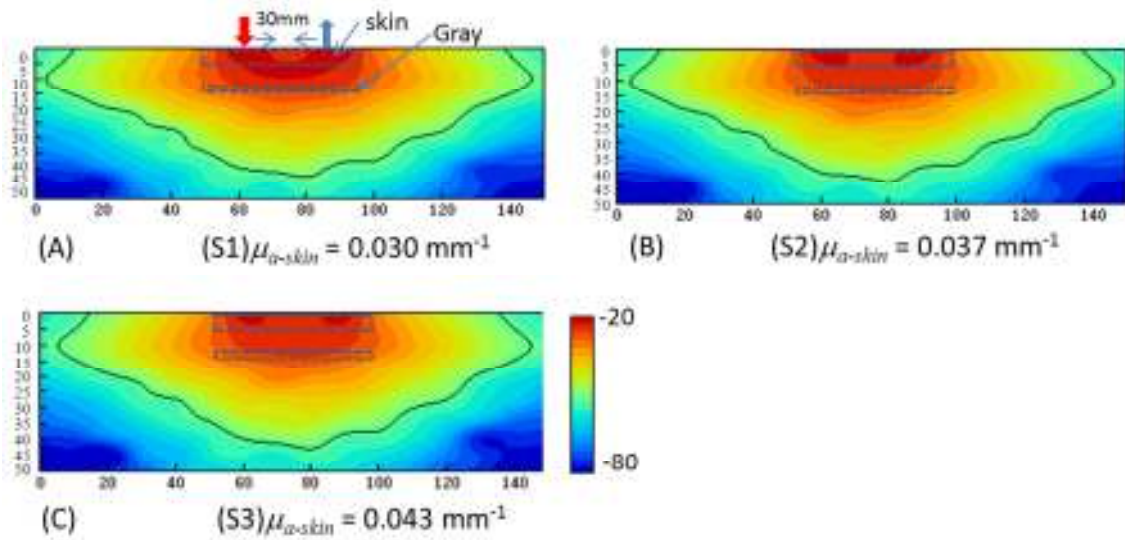


Fig. 5.12: The lightpath probability distributions $\psi(r)$ for three cases of different μ_{a-skin} .

Table 5.4 The lightpath probabilities averaged over the skin and gray matter layers. The ranges of the averaging in the skin and gray matter layers are marked in Fig 5.12 as dashed line.

Case	μ_{a-skin} (mm^{-1})	ψ_{skin}	ψ_{gray}	$\frac{\psi_{gray}}{\psi_{skin}}$
(S1)	0.030	7.03×10^{-8}	1.06×10^{-9}	1.50×10^{-2}
(S2)	0.037	5.79×10^{-8}	9.91×10^{-10}	1.71×10^{-2}
(S3)	0.046	4.23×10^{-8}	8.01×10^{-10}	1.89×10^{-2}

To further examine the influence of μ_a skin on mapping images, the lightpath probability distributions, $\psi(r)$, are calculated, which represents the sensitivity of the absorption change at position r to the change in the measured light intensity Φ . (Section 2.3.2).

Figure 5.12 (A), (B) and (C) show the lightpath probability distributions, $\psi(r)$, for three cases with $\mu_{a-skin} =$ (S1) 0.030 mm^{-1} , (S2) 0.037 mm^{-1} , and (S3) 0.043 mm^{-1} ,

respectively. The lightpath probability between the source and detector decreases with the increase in μ_{a-skin} . To see the difference in more detail, the values of the lightpath probabilities averaged over the skin and gray matter layers, ψ_{skin} and ψ_{gray} , are listed in Table 5.1 where ψ_{skin} and ψ_{gray} are the averages over the rectangular regions indicated by the blue lines in the skin and gray matter layers in Fig. 5.12, respectively. ψ_{skin} is always much larger than ψ_{gray} , but their ratio, ψ_{gray}/ψ_{skin} , increases with the increase in μ_{a-skin} by 14 % and 26 % as shown in Table 5.4 and Fig. 5.13.

By increasing μ_{a-skin} , the contribution of the skin layer to the attenuation of the measured light intensities relatively decreases compared to those of the gray matter layer. Then the change in the absorption in the gray matter leads to larger ΔOD than that with lower absorption in the skin layer. This explains the reason why ΔOD values of the optical mapping image increases with the increase in μ_{a-skin} .

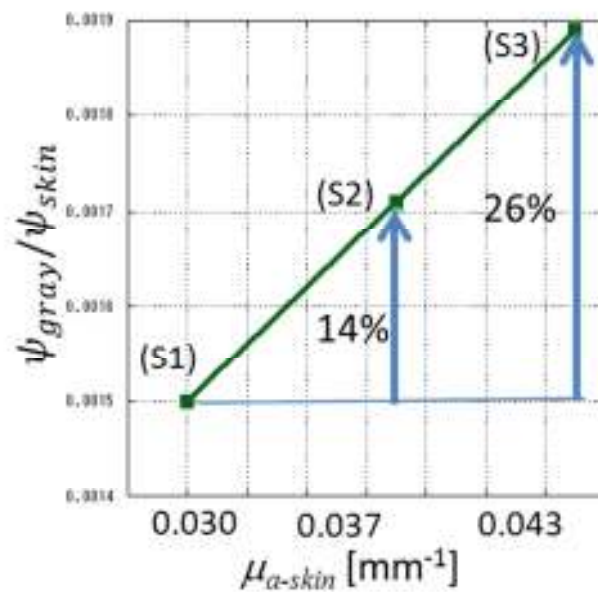


Fig. 5.13: The ratios of ψ_{gray}/ψ_{skin} in Table 5.4 are plotted.

5.5.3 When the blood volume in the skin layer increases simultaneously with the brain activation

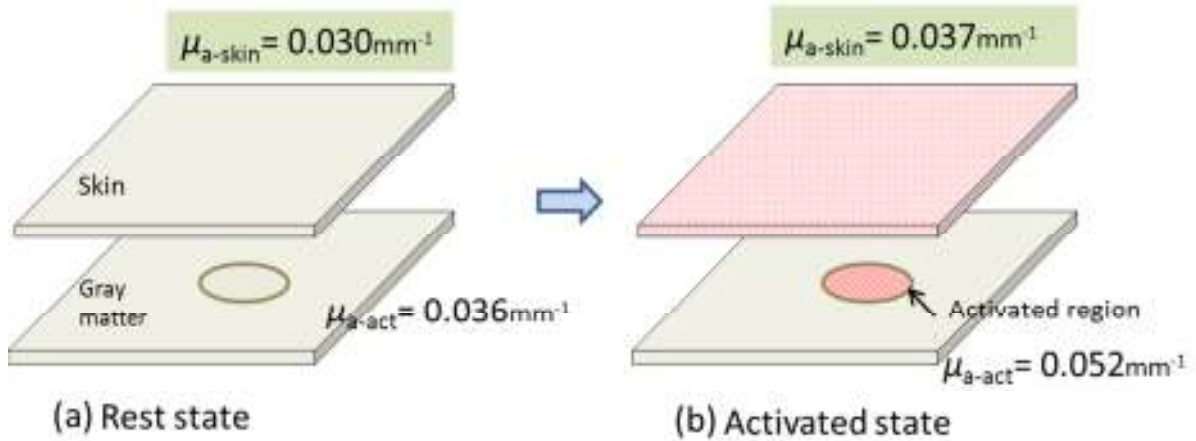


Fig. 5.14: The blood volume in the skin layer increases simultaneously with brain activation. (a) rest state, (b) activated state.

In the simulation of previous section 5.5.2, the blood volume in the skin layer is kept constant for the rest and activated states in the brain. However, brain activation is often accompanied by the increase in the blood volume in the skin layer. In this section, the blood volume in the skin layer is assumed to increase from the normal value simultaneously with brain activation. As shown in Fig. 5.14, for the rest state, the absorption coefficients of the skin (dermis) layer and the activated region, μ_{a-skin} and μ_{a-act} , are 0.030 mm^{-1} and 0.036 mm^{-1} respectively. When the brain is activated, the absorption coefficients of the skin layer and the activated region, μ_{a-skin} and μ_{a-act} , increase to 0.037 mm^{-1} and 0.052 mm^{-1} , respectively.

Figure 5.15 (a) shows the simulation result of the mapping image for simultaneous increase in μ_{a-skin} and μ_{a-act} in the activated state. The activated region indicated by the dashed circle is hardly observable in the mapping image. Fig. 5.15(b) shows the values of the 24 data points. The ΔODs at the data points, No. 9, 12, 13, and 16, close to the activated region did not show larger values than those at other data points. Therefore, the increase in μ_{a-act} by brain activation is unobservable in the mapping image. When

μ_{a-skin} increases from 0.030 mm^{-1} to 0.037 mm^{-1} simultaneously with the increase in μ_{a-act} in the activated state, the effect of the increase in μ_{a-skin} on the mapping image is greater than the increase in μ_{a-act} by the brain activation. So, 40% increase in the blood volume fraction, f_v , in the skin layer from 0.10 to 0.14 leading to 23% increase in μ_{a-skin} completely hinders from imaging the brain activation in the gray matter with 44% increase in μ_{a-act} . There are several reasons. The dermis layer is much closer to the sources and detectors. The blood volume changes are assumed to take place over the whole dermis layer while the activated region occupies only a part of the gray matter layer.

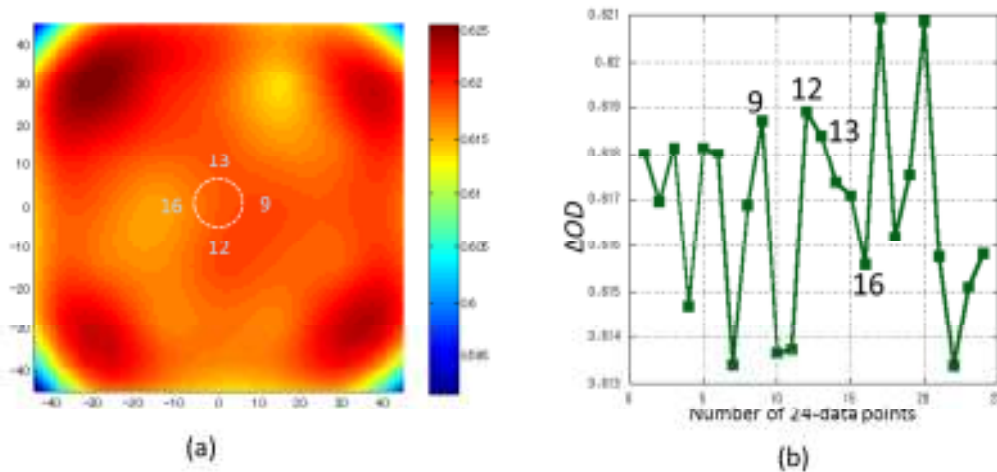


Fig. 5.15: (a) The simulation results of the mapping image for simultaneous increase in μ_{a-skin} and μ_{a-act} by brain activation. μ_{a-skin} and μ_{a-act} increase from 0.030 mm^{-1} to 0.037 mm^{-1} and from 0.036 mm^{-1} to 0.052 mm^{-1} , respectively. (b) ΔOD at the 24 data points for the mapping image of (a). The dashed circle in the mapping image indicates the true activated regions. 9, 12, 13 and 16 are the numbers of the data points close to the activated region.

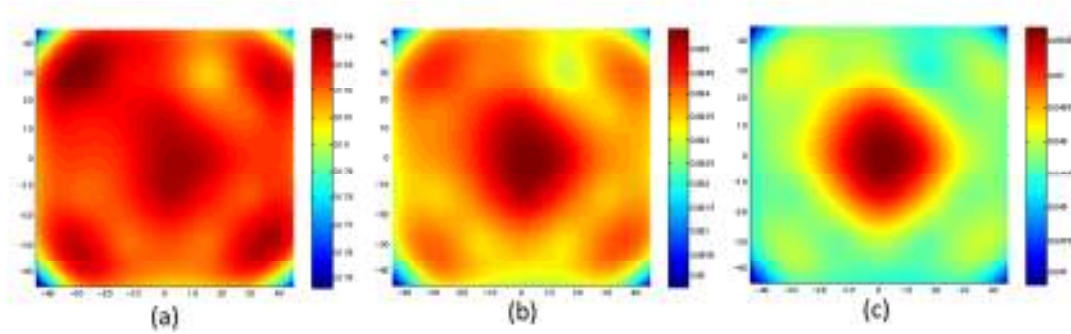


Fig. 5.16: The simulation results of the mapping image for simultaneous increase in μ_{a-skin} and μ_{a-act} by brain activation. (a) μ_{a-skin} increases from 0.030 mm^{-1} to 0.032 mm^{-1} , (b) μ_{a-skin} increases from 0.030 mm^{-1} to 0.031 mm^{-1} , and (c) μ_{a-skin} increases from 0.030 mm^{-1} to 0.0305 mm^{-1} .

Figure 5.15 shows that the increase in μ_{a-skin} from 0.030 mm^{-1} to 0.037 mm^{-1} at the activated state is too large to observe the activated region in the mapping images. Then a question is how much increase in μ_{a-skin} would be allowed to observe the activated region. To answer the question, the following three cases are considered; (a) μ_{a-skin} increases 6.7% from 0.030 mm^{-1} to 0.032 mm^{-1} , (b) μ_{a-skin} increases 3.3% from 0.030 mm^{-1} to 0.031 mm^{-1} , and (c) μ_{a-skin} increases 1.7% from 0.030 mm^{-1} to 0.0305 mm^{-1} . From the rest to activated state, the absorption coefficient of the activated region, μ_{a-act} , increases from 0.036 mm^{-1} to 0.052 mm^{-1} in the same way as before. Fig. 5.16 shows the results of simulation.

In case of (a) for 6.7% increase in μ_{a-skin} , it is difficult to observe the activated region. In cases of (b) and (c) for 3.3% and 1.7% increases in μ_{a-skin} , the activated region is observable, especially in case (c). It is found that when μ_{a-skin} and μ_{a-act} increase simultaneously, the activated region can be observable in the mapping images only if the μ_{a-skin} increases less than about 3%. Increase in μ_{a-skin} of 3% corresponds to the increase in the blood volume fraction, f_v , of 5% from 0.10 to 0.105. So it can be said that the activated brain regions are observable when f_v increases less than 5%.

5.6 Discussion and Conclusion

Both the vein in the CSF layer and blood volume changes in the skin layer affect the images of optical mapping. It is because that anatomical variations in the superficial layers lead to the different effective pathlength in the activated region and different sensitivity of the activated region to ΔOD . The skin and CSF layers are anatomically separated by the skull layer, and the effects of intracranial and extracranial blood volume to mapping images are contrary. The significant result of this study is that the signal of the mapping image by the activated region increases with the increase in μ_{a-skin} representing the increase in the skin blood volume, contrary to a common understanding that the increase in μ_{a-skin} decreases the signal of the mapping image by the activated region. The existence of a thick vein above the center of the activated region reduces the maximum of ΔOD by 15% with the size of 1 mm-side square having μ_a of 0.26 mm^{-1} and reduces by 34% with the size of 1 mm \times 2 mm rectangle having μ_a of 0.26 mm^{-1} . On the contrary, the increases in μ_{a-skin} from 0.030 mm^{-1} to 0.037 mm^{-1} and to 0.043 mm^{-1} , increase the maximum of ΔOD by 10% and 19%, respectively. When the blood volume in the skin layer increases simultaneously with the brain activation, it becomes difficult to observe the activated region in the mapping images because the effects of the blood volume increase in the skin layer is greater than that of the brain activation. When the changes in μ_{a-skin} or f_v are smaller than 3 % or 5 %, respectively, the activated region can be observable in the mapping images.

Due to the individual anatomical and physiological variation, the effective pathlength of light through the head is different. Comparisons among different subjects or different regions within a subject are difficult unless the pathlengths of light are determined. Future studies are needed to remove these influences and improve the performances of the mapping images. In fMRI, measuring two brains simultaneously, termed hyperscanning have been developed [70].

There are several limitations in this numerical study where a simple five-layered model is used to mimic the human head. Recently, the realistic head models based on

MR head images have been used to predict light propagation in the head for NIRS and optical mapping [71, 72]. Although the head model is simple in this study, the trends of the influences of the superficial layers on the optical mapping are the same.

The spatial resolution of the mapping image is relatively low, because the arrangement of the probes is a conventional topographic array. By using of high-density probes, the spatial resolution of the mapping images can be improved significantly [63].

Chapter 6 Influences of Blood Volume Changes in Cerebrospinal Fluid and Skin Layers on Optical Mapping: phantom experiments

6.1 Introduction

In this chapter, the influences of the existence of a thick blood vessel in the CSF layer and the blood flow changes in the skin layer on optical mapping are investigated by phantom experiments. Even though the numerical simulations in chapter 5 have demonstrated the influences quantitatively, the phantom experiments are performed to further support the results of the numerical study.

Phantoms simulating head tissues can provide realistic changes in the optical properties and can evaluate the performance of optical mapping. Multi-layered optical phantoms developed in a previous study generally have regular shapes and fixed optical properties [73]. To overcome these limitations, there is a need of tissue-like phantoms with changeable optical properties. Some dynamic phantoms have been developed. Funane et al. [74] proposed a dynamic phantom with two stage-driven absorbers for mimicking hemoglobin changes in tissues, which was used to evaluate the effect of superficial tissues in NIRS. This type of phantoms simulates absorption changes in tissues but cannot simulate spatial variations in the absorption coefficient. Koh et al. [75] developed a dynamic test phantom consisting of a modified liquid crystal display (LCD) sandwiched between two layers of tissue simulating epoxy resin, in which the attenuation at different regions was electrically controlled. However, due to the LCD property, this setup can only simulate absorption changes in two dimensions.

In this experimental study, a layered-phantom was used, which had a rectangular

cavity in the CSF layer for insertion of a rectangular blood vessel phantom to simulate the existence of blood vessel. In addition, the absorption coefficient of dermis was varied by exchanging the skin layer phantom with different optical properties to simulate the blood volume changes in the skin layer.

In this chapter, firstly a head phantom is introduced for the experiments to study the effects of a blood vessel in the CSF layer and blood volume changes in the skin layer. Secondly, the measurement systems for optical mapping and its principles are described. The last part of this chapter will show the experimental results of optical mapping and discuss how the superficial layers influence on mapping images.

6.2 Head phantom

6.2.1 Head model with a blood vessel in the CSF layer

Figure 6.1 shows the structure of the head phantoms having five layers and vessel phantom in the CSF layer. A square or a rectangular blood vessel phantom was used to mimic the existence of the blood vessel in the CSF layer. A CSF layer phantom with the same height with the blood vessel was used, which had a space for inserting the blood vessel phantoms or a rectangular bar with the optical properties same as those of the

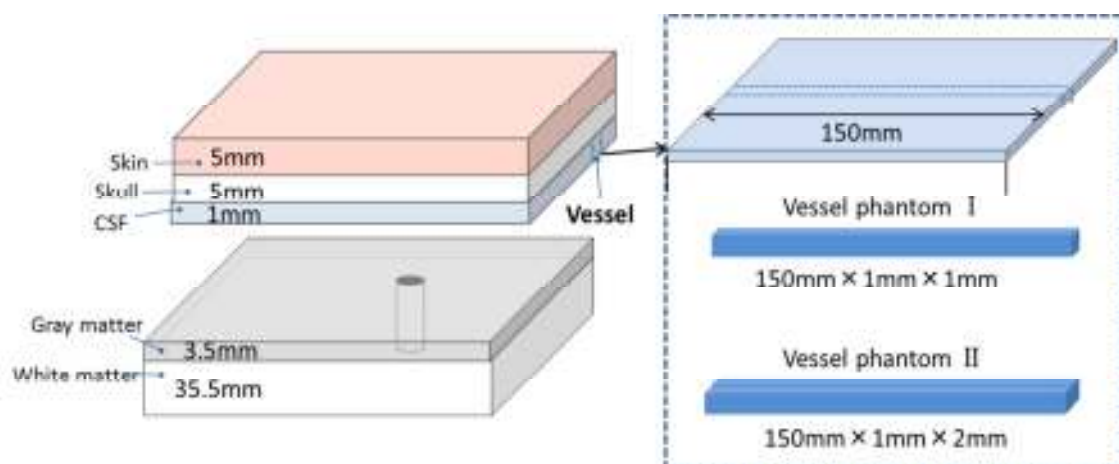


Fig. 6.1: Head model and blood vessel phantoms to be inserted into the CSF layer.

CSF layer to simulate the case of no vessel in the CSF layer.

Table 6.1 shows the size and optical properties of the blood vessel phantoms. Five cases are considered. i.e., case (C1) with no vessel in the CSF layer, case (C2) with a 1 mm-side square blood vessel having μ_a of 0.13 mm⁻¹ and μ_s' of 3.69 mm⁻¹, case (C3) with a 1 mm-side square blood vessel having μ_a of 0.26 mm⁻¹ and μ_s' of 3.69 mm⁻¹, case (C4) with a 1 mm×2 mm rectangular blood vessel having μ_a of 0.13 mm⁻¹ and μ_s' of 3.69 mm⁻¹, and (C5) with a 1 mm×2 mm rectangular blood vessel having μ_a of 0.26 mm⁻¹ and μ_s' of 3.69 mm⁻¹.

Table 6-1 The size and optical properties of blood vessel in the CSF layer.

Size of vessel	case	μ_a (mm ⁻¹)	μ_s' (mm ⁻¹)
Nothing	(C1)	0.02	0.30
Square	(C2)	0.13	3.69
 1-mm×1-mm	(C3)	0.26	3.69
Rectangular	(C4)	0.13	3.69
 1-mm×2-mm	(C5)	0.26	3.69

6.2.2 Head model with blood volume changes in the skin layer

The skin layer phantoms were divided into two parts: epidermis and dermis. The thickness of the epidermis and dermis were given as 1.0 mm and 4.0 mm. As explained in Chap. 5, the epidermis in the skin phantom was much thicker than the real ones, but this was employed due to the limitation in the experimental setup. The material of the dermis was the same as those mentioned in Chap. 2, while the material of the epidermis was a vinyl chloride plastic sheet which scattered light similarly to the tissues. The probe holders were attached on the epidermis layer and the dermis layer was movable. Figure 6.2 shows the head model which was able to simulate the blood volume changes in the skin layer. Three dermis phantoms with different μ_a were prepared to simulate varying blood volume in the skin layer.

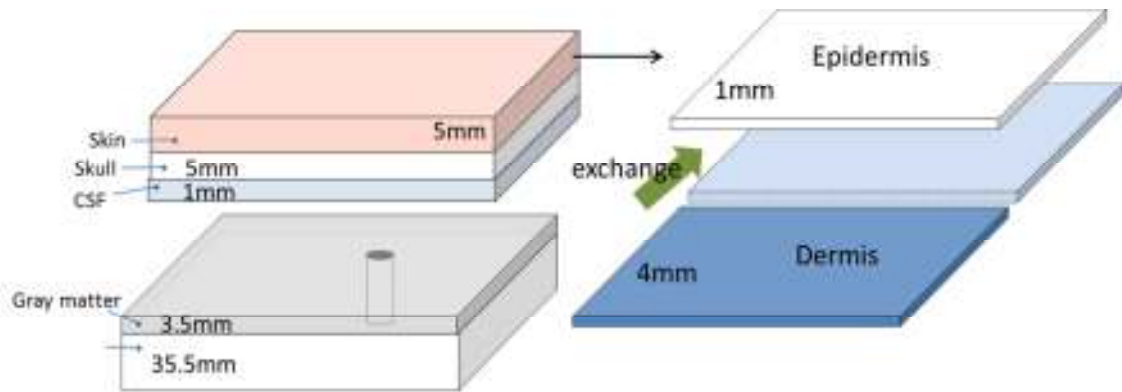


Fig. 6.2: Head model with blood volume changes in the skin layer.

The optical properties of the epidermis and dermis layers are shown in Table 6.2. μ_a and μ_s' of the epidermis was fixed as 0 mm^{-1} and 0.85 mm^{-1} . Three cases were assumed for the optical properties of the dermis; case (S1) where μ_a of the dermis was 0.030 mm^{-1} without blood, case (S2) where μ_a of the dermis was 0.056 mm^{-1} for the normal blood volume fraction and case (S3) where μ_a of the dermis was 0.086 mm^{-1} for the increased blood volume fraction. In the phantom experiments, the values of μ_a for cases (S2) and (S3) were 1.2~1.5 times those used in simulation of Section 5.2.4. It is assumed that even if the increase in μ_a in the dermis is slightly bigger, the tendency of the influence does not change. The standard optical properties of each layer at the wavelength of 805nm are listed in Table 2.1.

Table 6-2 The optical properties of the skin layer consisting of the epidermis and dermis.

Tissue	Case	$\mu_a (\text{mm}^{-1})$	$\mu_s' (\text{mm}^{-1})$
Epidermis	S1~S3	0	0.85
Dermis	S1	0.030	0.73
	S2	0.056	0.73
	S3	0.086	0.73

6.3 Measuring methods

As mentioned in Section 2.4.4, a multi-channel CW-NIRS imaging system (FOIRE-3000: Shimadzu Corporation) was used in the experiment. The arrangement of the probes is shown in Fig. 2.4. The changes in the optical density (ΔOD) at 805nm were used as the input data for mapping images, and 24 measured values of ΔOD were located at the 24 data points. The optical mapping images were constructed by 2-D spline interpolation of ΔOD s at the 24 data points.

Figure 6.3 shows a typical sequence of the measured OD values as a function of time in the measurement process for studying the effect of the blood vessel in the CSF layer. The vessel size is $150\text{mm}\times 1\text{mm}\times 1\text{mm}$, and its $\mu_a = 0.13\text{ mm}^{-1}$.

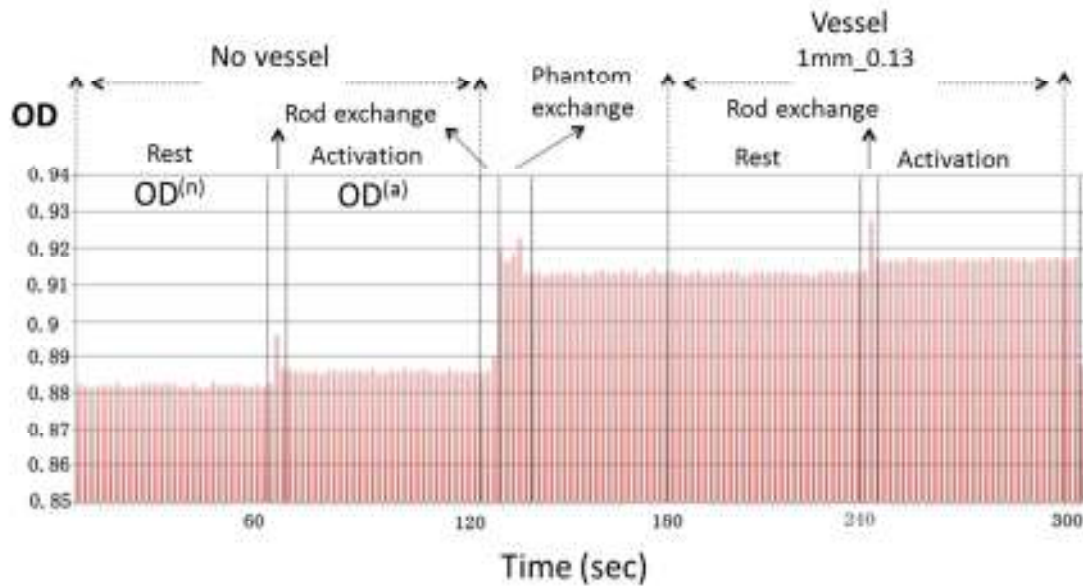


Fig. 6.3: An example of the measured OD values in the measurement process for studying the effect of the blood vessel in the CSF layer. OD values at the data point 9 are shown. The vessel size was $150\text{mm}\times 1\text{mm}\times 1\text{mm}$, and its $\mu_a = 0.13\text{ mm}^{-1}$.

Firstly, to simulate case (C1) with no vessel, a rod with the optical properties of the CSF layer having the same size with the blood vessel was inserted into the horizontal

rectangular cavity in the CSF layer. For the rest state (OD^n), a rod for the rest state was inserted into the vertical cavity penetrating the gray matter and white matter layers. After 60 seconds, the rod for the rest state was replaced by a rod for the activated state to simulate the activated state (OD^a). Thus, the change in the OD for the case of no vessel, ΔOD , was obtained by

$$\Delta OD = OD^a - OD^n \quad (6.1)$$

Secondly, to simulate the existence of a blood vessel in the CSF layer, a blood vessel phantom was inserted into the horizontal cavity by replacing the rod for the CSF layer. An interval was set for the replacement of the two rods. For cases (C2) to (C5) with a blood vessel in the CSF layer, the rods for the rest and activated states were exchanged per 60 seconds to simulate the rest and activated states. Again, ΔOD s for the cases with a blood vessel in the CSF layer were obtained. Every measurement is repeated five times and the average value was used for constructing optical mapping images.

Moreover, to evaluate the reproducibility of the measurement, the standard deviations (SDs) of ΔOD s at 24 data points for repeated five measurements were calculated for the case of the blood vessel with the size of 150 mm×1 mm×2 mm and $\mu_a = 0.26 \text{ mm}^{-1}$. Figure 6.4 shows the results of ΔOD as the mean±SD for the repeated five measurements. The arrangement of probes and activated region is shown on the left. The graph displays that although there are differences in the SD values among the 24 data, the SD values are less than 5 % for all data. This result confirms the reproducibility of the phantom measurements.

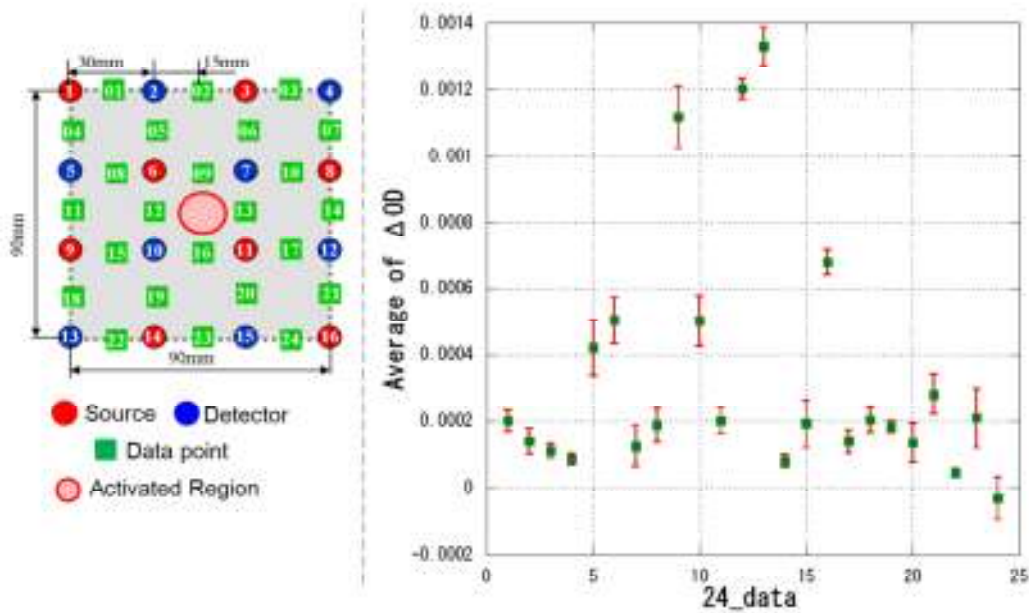


Fig. 6.4: (left) Arrangements of source, detector, data point and the position of the activated region in the gray matter. (right) green dots are the averages of ΔOD at 24 data points, and the red error bars are the standard deviation for repeated five measurements.

6.4 Experimental results

6.4.1 Effect of the blood vessel in the CSF layer

Figure 6.5 shows the optical mapping images obtained by the phantom experiments; (A) showing the arrangement of the detector, activated region and blood vessel, (B) to (F) showing the images for cases (C1) to (C5), respectively, and (G) showing the ΔOD profiles. Comparing with case (C1) without the vessel, the existence of the vessel, cases (C2), (C3), (C4) and (C5), reduced ΔOD of the brain activation in the mapping images. As μ_a increased from 0.13 mm^{-1} for case (C2) to 0.26 mm^{-1} for case (C3) with the same 1 mm -side square vessel, the maximum of ΔOD reduced from 0.023 to 0.019 . Keeping μ_a constant as 0.26 mm^{-1} , the maximum of ΔOD of case (C5) with the $1 \text{ mm} \times 2 \text{ mm}$ rectangular blood vessel reduced to 0.0015 from 0.0017 of case

(C3) with the 1 mm-side square blood vessel.

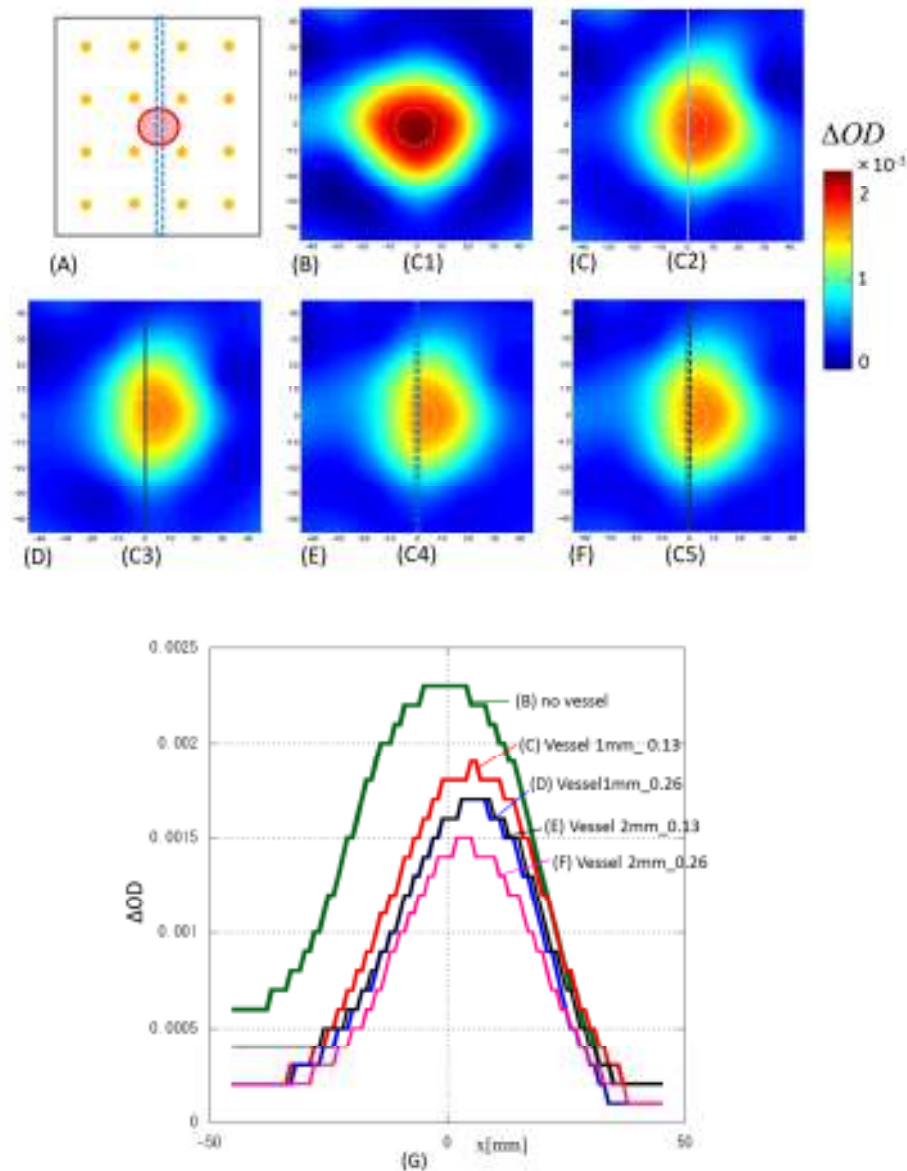


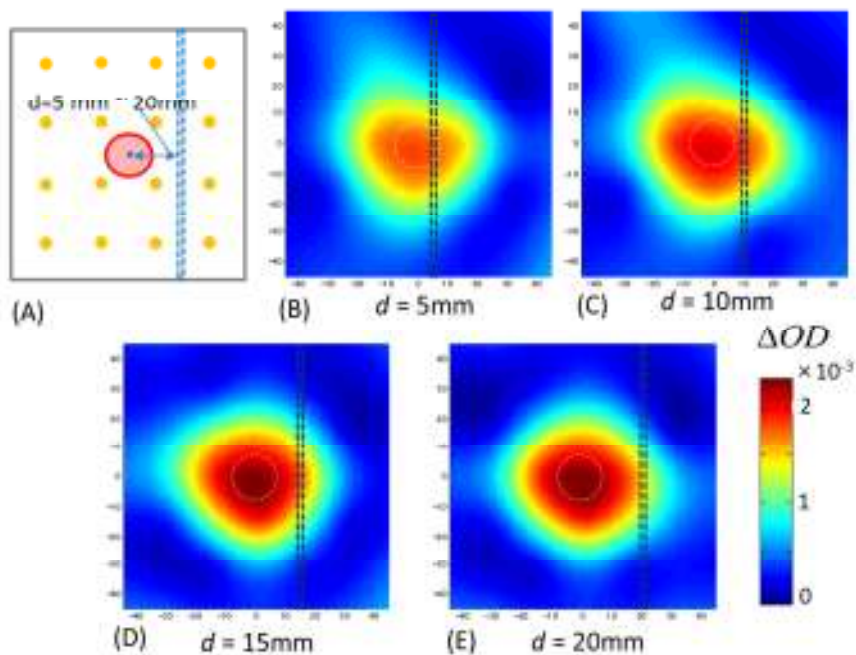
Fig. 6.5: (A) Top view of the head model including the activated region in the gray matter and blood vessel in the CSF layer. (B)-(F) experimental mapping images of cases (C1)-(C5). The dashed circle and rectangular superimposed on the mapping images indicated the shapes of the activated region and blood vessel. (G) the profiles of ΔOD along the horizontal lines through the center of the activated region.

ΔOD for case (C1) without the vessel is the largest among all the cases. These

experimental results support the numerical results that both increases in the absorption coefficient and size of the vessel reduce ΔOD .

Figure 6.6 shows the influence of the distance between the center of activated region and vessel, d , on the mapping images when the 1 mm \times 2 mm rectangular blood vessel with $\mu_a = 0.26 \text{ mm}^{-1}$ was used; (A) showing the arrangement of the sources, detectors, activated region and the blood vessel, (B) to (E) showing the images for $d = 5 \text{ mm}$, 10 mm, 15 mm and 20 mm, respectively, and (F) showing the ΔOD profiles along the horizontal lines through the centers of the activated regions. The effect of the vessel to the mapping images decreased with the increase in d . For $d = 0 \text{ mm}$, the effect of the blood vessel to the mapping images was the greatest. As d increased larger than 15 mm, the effect of the vessel became negligible.

The same experiment using a 1 mm-side square blood vessel with $\mu_a = 0.26 \text{ mm}^{-1}$ was also performed. The results (not shown here) were similar with those using the 1 mm \times 2 mm rectangular blood vessel with $\mu_a = 0.26 \text{ mm}^{-1}$. The ΔOD values for $d = 0 \text{ mm}$ were the largest, and there was no effect of the blood vessel as d became larger than 15 mm.



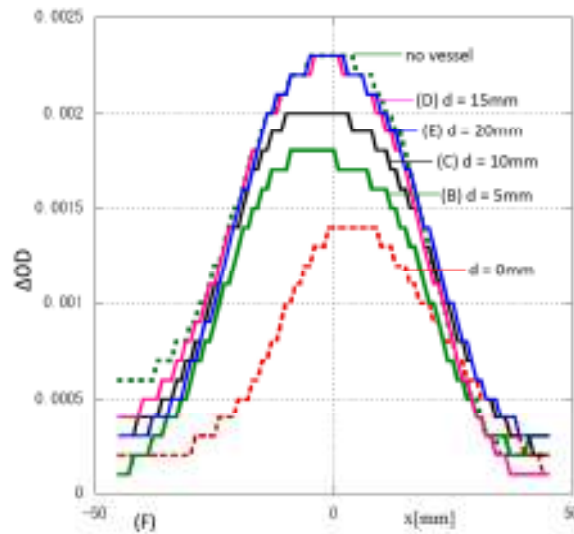


Fig. 6.6: (A) Top view of the head model including the activated region in gray matter and blood vessel in CSF layer. (B) to (E) experimentally obtained mapping images for different distances, (B) $d = 5$ mm, (C) $d = 10$ mm, (D) $d = 15$ mm, and (E) $d = 20$ mm for the blood vessel having a 1-mm \times 2-mm rectangular shape with $\mu_a = 0.26$ mm $^{-1}$. The dashed circles and rectangles superimposed on the mapping images indicate the shapes of the activated region and blood vessel. (F) the profiles of ΔOD along the horizontal lines through the center of the activated region. The dashed green and red curves show the profiles of ΔOD for no vessel and $d = 0$ mm.

6.4.2 Effect of the blood volume changes in the skin layer

Figure 6.7 (A)-(C) shows the optical mapping images obtained by the phantom experiments for cases (S1), (S2) and (S3) with varying μ_a of the dermis; (A) case (S1) where μ_a of the dermis was 0.030mm $^{-1}$, (B) case (S2) where μ_a of the dermis was 0.056 mm $^{-1}$, and (C) case (S3) where μ_a of the dermis was 0.086 mm $^{-1}$. For case (S1) without blood in the dermis, ΔOD was smaller than cases (S2) and (S3) where μ_a of the dermis increased. With the increase in the blood volume fraction in the dermis, μ_a of the skin layer increased from case (S2) to case (S3), and the value of ΔOD increased. Fig. 6.7 (D) shows the profiles of ΔOD along the horizontal lines through the center of the active region. The peak values of ΔOD increased with the increase in μ_a of the dermis.

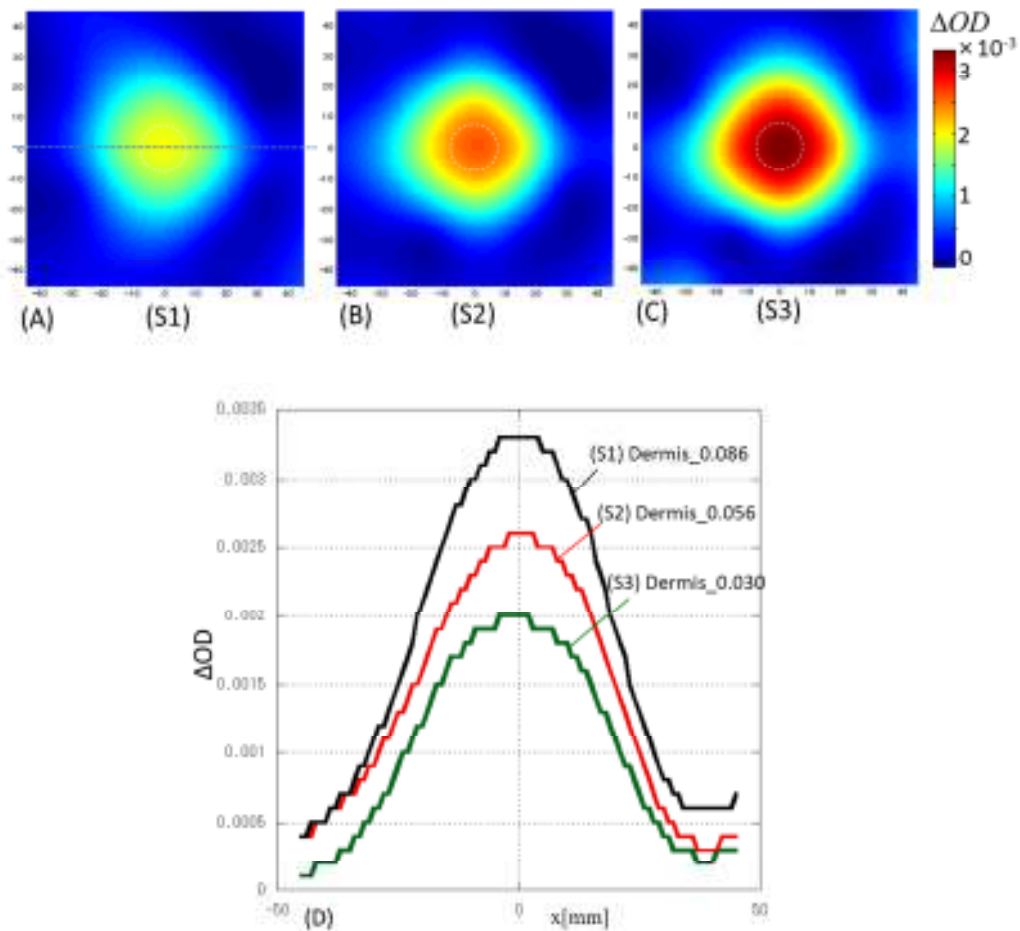


Fig. 6.7: (A) to (C) The experimental mapping images of cases (S1) to (S3), respectively. (D) the profiles of ΔOD along the horizontal lines through the center of the activated region.

6.5 Discussions and conclusions

Figure 6.8 compares the simulation and experimental results of 24 ΔOD for the same model with no vessel in the CSF layer. The ΔOD values at the data points of 9, 12, 13 and 16, which are closest to the activated region, mainly contribute to the ΔOD distribution in the mapping image. As seen from Fig. 6.8, the experimental results were slightly smaller than the simulation results at the data points of 9, 12, 13 and 16, but the agreement between the simulated and experimental results is good overall. There are

some reasons for attenuation of the signal in the phantom experiment, such as, the gap between the layers in the phantom, the contact angle between the fiber and the phantom surface, poor contact of the fibers to the phantom surface, and so on. The ΔOD values at the other data points obtained by experiments fluctuated around zero of the numerical results. However, in the phantom experiment, due to the systematic errors, the ΔOD values might be minus or plus at the area of no absorption change.

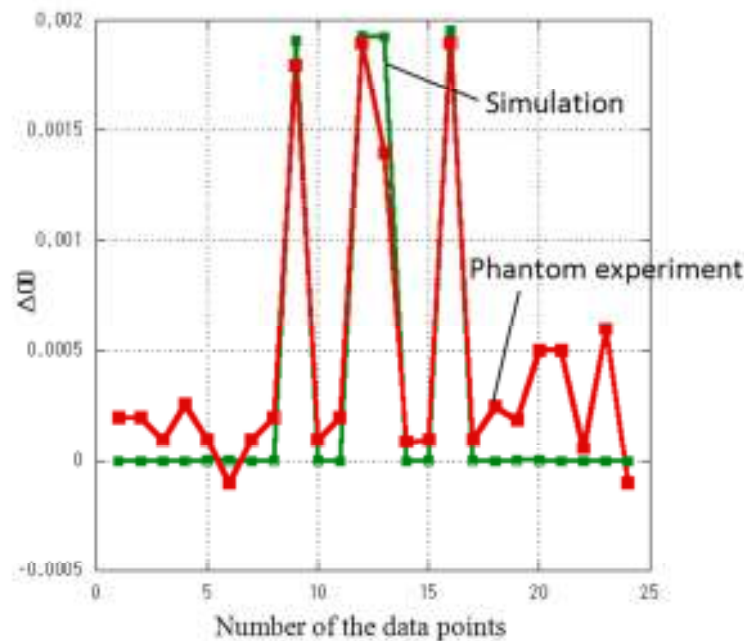


Fig. 6.8: The comparison of simulation and phantom experimental results of 24 ΔOD s. A head phantom with no vessel in the CSF layer was used.

The comparison indicates that the errors between the simulation and phantom experiment results are acceptable. The experimental results of the influences of the blood volume changes in the skin layer and the existence of thick blood vessel in the CSF layer on the images of optical mapping were very similar with the numerical results. The increase in the blood volume in the skin layer increased the ΔOD values while the existence of the blood vessel in the CSF layer decreased the ΔOD values. The experimental results demonstrated further support to the simulation results. Both the

blood vessel in the CSF layer and blood volume changes in the skin layer affect the images of optical mapping.

Chapter 7 General Conclusions

This dissertation has proposed numerical and experimental methods to investigate the influences of structural and physiological differences of superficial head layers on optical mapping. To study these influences, light propagation in the three-dimensional head model has been simulated by solving the photon diffusion equation using the FEM, and the optical mapping images have been constructed from the simulated measurement data. Experiments using tissue-mimicking phantoms with spatially varying thickness and changeable optical properties of head layers were also performed to further support the numerical study.

The contents of this dissertation are summarized from two major aspects: quantifying the above stated influences on the mapping images of brain activities for the cases of (1) spatially varying thicknesses of the skull and CSF layers and (2) a thick blood vessel in the CSF layer and (3) blood volume changes in the skin layer. The findings of this study are as follows.

Differences in the thicknesses of both the skull and CSF layers affect the mapping images of brain activities. The increase in the skull thickness decreases the value of ΔOD of the activated region significantly. The values of maximum of ΔOD decrease to about 40 % of its original value with every 1 mm increase in the skull thickness. In contrast, the increase in the CSF thickness increases the value of ΔOD of the activated region generally. When the CSF thickness increases further more than about 3 mm, the value of ΔOD slightly decreases. The effects of the CSF thickness on the mapping images are less significant than those of the skull thickness. It is also found that the effects of the spatially varying thicknesses of the skull and CSF layers on the mapping images are smaller than those of the position of the activated region relative to the data points.

Both the thick vein in the CSF layer and the blood volume changes in the skin layer affect the images of optical mapping. Contrary to the common understanding, the ΔOD values in the mapping images of the activated region increase with the increase in

the blood volume in the skin layer. The maximum of the ΔOD value increases about 14 % from its original value with every 0.01 mm^{-1} increases in the μ_a of the skin layer due to the increase in the blood volume fraction in the skin layer from 0.10 to 0.165. On the other hand, the existence of a thick blood vessel ($\phi=2\text{mm}$, $\mu_a=0.13\text{mm}^{-1}$) in the CSF layer decreases about 20% of the maximum value of ΔOD . It is also found that the mapping images are not observable when the blood volume fraction in the skin layer increases from 0.10 to 0.105 simultaneously with the brain activation in the gray matter layer. Overall, both the simulation and experimental study show the influences of the superficial layers on the images of optical mapping in similar ways.

The quantitative results about the influences of the superficial layers in the study provide information for how the optical mapping images are to be corrected for comparing the images among different individuals and for different head regions in an individual. To remove the effect of anatomy changes and improve the quality of the mapping image of the brain activation, these results can be used to compensate the mapping images in combination with images of other modalities such as MRI and X-ray CT as a priori information of the head anatomy. Hence, *in vivo* experiments considering the influences of structural and hemodynamic differences in the superficial layers on optical mapping remain as a future subject. Furthermore, these results help better understand light propagation through the head and pursue the future optical mapping studies.

Although the head models in this study consist of layered slabs and the arrangement of the probes is the simplest one with an equal source-detector distance of 30 mm, the methodology of the simulation and phantom experiment in this study can be applied to sophisticated head models and with varied source-detector distances. If the head model is extended to more realistic 3D models based on the MR or x-ray CT images, the results from the simulation and phantom experiment would be more reliable and can be easily generalized. Furthermore, the influences of the superficial layers on the mapping images can be directly and quantitatively investigated. Hence, future study on the modeling of realistic head model is necessary.

References

- [1] B. Chance, "Optical method," *Annu. Rev. Biophys. Chem.* **20**, 1-28, (1991).
- [2] F. F. Jobsis, "Noninvasive, infrared monitoring of cerebral and myocardial oxygen sufficiency and circulatory parameters," *Science* **198**, 1264-1267 (1997).
- [3] M. Cope and D. T. Delpy, "System for long-term measurement of cerebral blood and tissue oxygenation on newborn infants by near infra-red transillumination," *Med. Biol. Eng. Comput.* **26**, 289-294 (1988).
- [4] Y. Hoshi and M. Tamura, "Detection of dynamic changes in cerebral oxygenation coupled to neuronal function mental work in man," *Neurosci. Lett.* **150**, 5-8 (1993).
- [5] A. Villringer, J. Planck, C. Hock, L. Schleinkofer, U. Dirnagl, "Near infrared spectroscopy (NIRS): a new tool to study hemodynamic changes during activation of brain function in human adults," *Neurosci. Lett.* **154**, 101-104 (1993).
- [6] B. Chance, A. Villringer, K. M. Einhaupl, "Optical imaging of brain function and metabolism," *Garmisch-Partenkirchen, J. Neurol.* **239**, 359-360 (1992).
- [7] T. Kato, A. Kamei, S. Takahashi, T. Ozaki, "Human visual cortical function during photic stimulation monitoring by means of near-infrared spectroscopy," *J. Cereb. Blood Flow Metab.* **13**, 516-520 (1993).
- [8] A. Maki, Y. Yamashida, Y. Ito, E. Watanabe, H. Koizumi, "Spatial and temporal analysis of human motor activity using noninvasive NIR topography," *Med.phys.* **22**, 1997-2005 (1995).
- [9] T. Yamamoto, A. Maki, Y. Yamashida, Y. Tanikawa, Y. Yamada, H. Koizumi, "Noninvasive brain-functional measurement system: optical topography," in *optical Tomography and Spectroscopy of Tissue IV*, Proc. SPIE. 4250 (2001).
- [10] Y. Yamashida, A. Maki, H. Koizumi, "Near-infrared topographic measurement system : imaging of absorbers localized in a scattering medium," *Rev. Sci. Instrum.* **67**, 730-732 (1996).
- [11] Y. Yamashida, A. Maki, H. Koizumi, "Measurement system for noninvasive dynamic optical topography," *J. Biomed. Opt.* **4**, 414-417 (1999).
- [12] H. Koizumi, T. Yamamoto, A. Maki, Y. Yamashita, H. Sato, H. Kawaguchi, N. Ichikawa, "Optical topography: practical problems and new applications," *Appl. Opt.* **42**, 3054-3062 (2003).

- [13] H. Eda, I. Oda, Y. Ito, Y. Wada, Y. Oikawa, Y. Tsunazawa, M. Takada, Y. Tsuchiya, Y. Yamashita, M. Oda, A. Sassaroli, Y. Yamada, M. Tamura, “Multi-channel time-resolved optical tomographic imaging system,” *Review of Scientific Instruments*, **70**, 3595-3602 (1999).
- [14] V. Toronov, A. Webb, J. H. Choi, M. Wolf, A. Michalos, E. Gratton, “Investigation of human brain hemodynamics by simultaneous near-infrared spectroscopy and functional magnetic resonance imaging,” *Medical Physics*, **28**, 521-527 (2001).
- [15] D. T. Delpy, M. Cope, P. van der Zee, S. Arridge, S. Wray, J. Wyatt, “Estimation of optical pathlength through tissue from direct time of flight measurement,” *Phys. Med. Biol.* **33**, 1433-1442 (1988).
- [16] T. J. Germon, P. D. Evans, A. R. Manara, N. J. Barnett, P. Wall, R. J. Nelson, “Sensitivity of near infrared spectroscopy to cerebral and extra-cerebral oxygenation changes is determined by emitter–detector separation,” *J. Clin. Monit. Comput.* **14**, 353–360 (1998).
- [17] T. Takahashi, Y. Takikawa, R. Kawagoe, S. Shibuya, T. Iwano, S. Kitazawa, “Influence of skin blood flow on near-infrared spectroscopy signals measured on the forehead during a verbal fluency task,” *NeuroImage*, **57**, 991-1002 (2011).
- [18] E. Kirilina, A. Jelzow, A. Heine, M. Niessing, H. Wabnitz, R. Bruhl, B. Ittermann, A. Jacobs, I. Tachtsidis, “The physiological origin of task-evoked systemic artefacts in functional near infrared spectroscopy,” *NeuroImage*, **61**, 70-81 (2012).
- [19] S. Kohno, I. Miyai, A. Seiyama, I. Oda, A. Ishikawa, S. Tsuneishi, T. Amita, K. Shimizu, “Removal of the skin blood flow artifact in functional near-infrared spectroscopic imaging data through independent component analysis,” *J. Biomed. Opt.* **12**, 062111,1-9 (2007).
- [20] N. M. Gregg, B. R. White, B. W. Zeff, A. J. Berger, J. P. culver, “Brain specificity of diffuse optical imaging: improvements from superficial signal regression and tomography,” *Front. Neurosci.* **2**, 1-8 (2010).
- [21] T. Funane, H. Atsumori, T. Katura, N. A. Obata, H. Sato, Y. Tanikawa, E. Okada, M. Kiguchi, “Quantitative evaluation of deep and shallow tissue layers contribution to fNIRS signal using multi-distance optodes and independent component analysis,” *NeuroImage*. **85**, 150-165 (2014).
- [22] T. Yamada, S. Umeyama, K. Matsuda, “Separation of fNIRS signals into functional and systemic components based on differences in hemodynamic modalities,”

- PLoSOne **7**, e50271 (2012).
- [23] A. P. Gibson, C. J. Hebden, S. R. Arridge, “Recent advances in diffuse optical imaging,” *Phys. Med. Boil.* **50**, R1-R43 (2005).
- [24] B. W. Pogue, K. D. Paulsen, “High-resolution near-infrared tomographic imaging simulations of the rat cranium by use of a priori magnetic resonance imaging structural information,” *Opt. Lett.* **23**, 1716–8 (1998).
- [25] M. Schweiger, S. R. Arridge, “Optical tomographic reconstruction in a complex head model using a priori region boundary information,” *Phys. Med. Biol.* **44**, 2703–21 (1999).
- [26] H. Kawaguchi, T. Hayashi, T. Kato, E. Okada, “Theoretical evaluation of accuracy in position and size of brain activity obtained by near-infrared topography,” *Phys. Med. Biol.* **49**, 2753-2765 (2004).
- [27] J. C. Gore, “Principles and practice of functional MRI of the human brain,” *J. Clin. Invest.* **112**, 4–9 (2004).
- [28] J. Haueisen, D. S. Tuch, C. Ramon, P. H. Schimpf, V. J. Wedeen, J. S. George, J. W. Belliveau, “The influence of brain tissue anisotropy on human EEG and MEG,” *Neuroimage*, **15**, 159 –166 (2002).
- [29] S. R. Arridge, “Optical tomography in medical imaging,” *Inverse Probl.* **15**, R41–R93 (1999).
- [30] A. Gibson, H. Dehghani, “Diffuse optical imaging,” *Phil. Trans. R. Soc. A.* **367**, 3055-3072 (2009).
- [31] M. D. Ross, K. A. Lee, W. M. Castle, “Skull thickness of black and white races,” *S. Afr. Med.J.* **50**, 635-638 (1976).
- [32] E. M. C. Hillman, “Experimental and Theoretical Investigations of Near Infrared Tomographic Imaging Methods and Clinical Applications,” in *Department of Medical Physics and Bioengineering*. London: University College London, 235-237 (2002).
- [33] H. Dehghani, S. R. Arridge, M. Schweiger, D. T. Delpy, “Optical tomography in the presence of void regions,” *J. Opt. Soc. Am. A.* **17**, 1659-1670 (2000).
- [34] E. Okada, D. T. Delpy, “Near-infrared light propagation in an adult head model. I. Modeling of low-level scattering in the cerebrospinal fluid layer,” *Appl. Opt.* **42**, 2906-2914 (2003).
- [35] T. Gautama, D. Mandic, M. V. Hulle, “Signal nonlinearity in fMRI: a comparison

- between BOLD and MION,” *IEEE Trans. Med. Imaging*, **22**, 636-644 (2003).
- [36] J. Frahm, K. Merboldt, W. Hnicke, A. Kleinschmidt, H. Boecker, “Brain or vein-oxygenation or flow? On signal physiology in functional MRI of human brain activation,” *NMR Biomed.* **7**, 45-53 (1994).
- [37] J. Culver, A. Siegel, M. Franceschini, J. Mandeville, D. Boas, “ Evidence that cerebral blood volume can provide brain activation maps with better spatial resolution than deoxygenated hemoglobin,” *Neuroimage*, **27**, 947-959 (2005).
- [38] M. Dehaes, L. Gagon, F. Lesage, M. Pelegrini-Issac, A. Vignaud, R. Valabregue, R. Grebe, F. Wallois, H. Benali, “Quantitative investigation of the effect of the extra-cerebral vasculature in diffuse optical imaging: a simulation study,” *Biomed. Opt. Express*, **2**, 680-695 (2011).
- [39] E. Okada, D. T. Delpy, “Near-infrared light propagation in an adult head model. II. Effect of superficial tissue thickness on the sensitivity of the near-infrared spectroscopy signal,” *App. Opt.* **42**, 2915-2922 (2003).
- [40] V. D. Tuan, “Biomedical photonics handbook,” CRC press, 2-6~2-11 (2003).
- [41] Y. Yamada, “Light-tissue interaction and optical imaging in biomedicine,” *Annual review of heat transfer*, **6**, 1-59 (1995).
- [42] K. Furutsu, Y. Yamada, “Diffusion approximation for a dissipative random medium and the applications,” *Phys. Rev. E.* **50**, 3634–3640 (1994).
- [43] M. Ferrari, V. Quaresima, “A brief review on the history of human functional near-infrared spectroscopy (fNIRS) development and fields of application,” *Neuroimage*, **63**, 921-935 (2012).
- [44] D. T. Sandwell, “Biharmonic Spline Interpolation of GEOS-3 and SEASAT Altimeter Data, *Geophys.*” *Res. Lett.* **14**, 139-142 (1987).
- [45] B. C. Wilson, G. Adam, “A Monte Carlo Model for the Absorption and Flux Distributions of Light in Tissue,” *Med. Phys.* **10**, 824–830 (1983).
- [46] J. J. Duderstadt, L. J. Hamilton, “Nuclear Reactor Analysis,” John Wiley and Sons, New York, Chap. 4, 672-675 (1976).
- [47] A. Ishimaru, “Wave Propagation and Scattering in Random Media,” Academic Press, New York, Vol. **1** (1978).
- [48] T. Koyama, A. Iwasaki, Y. Ogoshi, E. Okada, “Practical and adequate approach to modeling light propagation in an adult head with low-scattering regions by use of diffusion theory,” *Appl. Opt.* **44**, 2094-2103 (2005).

- [49] R. A. J. Groenhuis, H. A. Ferwerda, J. J. T. Bosch, "Scattering and Absorption of Turbid Materials Determined from Reflection Measurements," *Appl. Opt.* **22**, 2456–2467 (1983).
- [50] J. Haselgrove, J. Leigh, C. Yee, N. G. Wang, M. Maris, B. Chance, "Monte Carlo and diffusion calculations of photon migration in noninfinite highly scattering media," in *Time-Resolved Spectroscopy and Imaging of Tissues*, B. Chance and A. Katzir, eds. *Proc. SPIE* **1431**, 30–41 (1991).
- [51] T. J. Farrell, M. S. Patterson, B. C. Wilson, "A diffusion theory model of spatially resolved, steady-state diffuse reflectance for the noninvasive determination of tissue optical properties in vivo," *Med. Phys.* **19**, 879–888 (1992).
- [52] W. F. Cheong, S. A. Prahl, A. J. Welch, "A review of the optical properties of biological tissues," *IEEE J. Quantum Electron.* **26**, 2166-2185 (1990).
- [53] C. R. Simpson, M. Kohl, M. Essenpreis, M. Cope, "Near-infrared optical properties of ex vivo human skin and subcutaneous tissue measured using the Monte Carlo inversion technique," *Phys. Med. Biol.* **43**, 2465-2478 (1998).
- [54] M. Firbank, M. Hiraoka, M. Essenpreis, D. T. Delpy, "Measurement of the optical properties of the skull in the wavelength range 650–950 nm," *Phys. Med. Biol.* **38**, 503–510 (1993).
- [55] P. van der Zee, M. Essenpreis, and D. T. Delpy, "Optical properties of brain tissue," in *Photon Migration and Imaging in Random Media and Tissues*, B. Chance and R. R. Alfano, eds., *Proc. SPIE* **1888**, 454–465 (1993).
- [56] M. Firbank, S. R. Arridge, M. Schweiger, D. T. Delpy, "An investigation of light transport through scattering bodies with non-scattering region," *Phys. Med. Biol.* **41**, 767–783 (1996).
- [57] H. Dehghani, D. T. Delpy, "Near-infrared spectroscopy of the adult head: effect of scattering and absorbing obstructions in the cerebrospinal fluid layer on light distribution in the tissue," *Appl. Opt.* **39**, 4721-4729 (2000).
- [58] E. Okada, "The effect of superficial tissue of the head on spatial sensitivity profiles for near infrared spectroscopy and imaging," *Optical review*, **7**, 375-382 (2000).
- [59] T. Hayashi, Y. Kashio, E. Okada, "Effect of superficial tissue on spatial sensitivity profile of optical brain activity measurement evaluated by direct hybrid Monte Carlo-diffusion method," *Optical review*, **10**, 501-505 (2003).
- [60] G. E. Strangman, Q. Zhang, Z. Li, "Scalp and skull influence on near infrared

- photon propagation in the Colin27 brain template,” *NeuroImage*, **85**, 136-149 (2014).
- [61] N. Chauveau, X. Franceries, B. Doyon, B. Rigaud, J. P. Morucci, P. Celsis, “Effects of skull thickness, anisotropy, and inhomogeneity on forward EEG/ERP computations using a spherical three-dimensional resistor mesh model,” *Human Brain Mapping*, **21**, 86-97 (2004).
- [62] H. Zhao, Y. Tanikawa, F. Gao, Y. Onodera, A. Sassaroli, K. Tanaka, Y. Yamada, “Maps of optical differential pathlength factor of human adult forehead, somatosensory motor, occipital regions at multi-wavelengths in NIR,” *Phys. Med. Biol.* **47**, 2075-2093 (2002).
- [63] T. Yamamoto, A. Maki, T. Kadoya, Y. Tanikawa, Y. Yamada, E. Okada, H. Koizumi, “Arranging optical fibres for the spatial resolution improvement of topographical images,” *Phys. Med. Biol.* **47**, 3429-3440 (2002).
- [64] T. J. Germon, N. M. Kane, A. R. Manara, R. J. Nelson, “Near-infrared spectroscopy in adults: Effects of extracranial ischaemia and intracranial hypoxia on estimation of cerebral oxygenation,” *Br. J. Anaesth.* **73**, 503– 506 (1994).
- [65] S. N. Davie, H. P. Grocott, “Impact of extracranial contamination on regional cerebral oxygen saturation: A comparison of three cerebral oximetry technologies,” *Anesthesiology*, **116**, 1-7, (2012).
- [66] S. Takatani, M. D. Graham, “Theoretical analysis of diffuse reflectance from a two-layer tissue model,” *IEEE Trans. Biomed. Eng.* **BME-26**, 656-664 (1987).
- [67] D. O. Cooney, “Biomedical Engineering Principles,” Marcell Dekker, New York, Table 3.1, 1976.
- [68] H. Liu, B. Chance, A. H. Hielscher, S. L. Jacques and F. K. Tittel, “ Influence of blood vessels on the measurement of hemoglobin oxygenation as determined by time-resolved reflectance spectroscopy,” *Am. Assoc. Phys. Med.*, **22**, 1209-1217 (1995).
- [69] S. L. Jacques, “Optical assessment of cutaneous blood volume depends on the vessel size distribution: a computer simulation study,” *J. Biophotonics*, **3**, 75-81, (2010).
- [70] P. R. Montague, G. S. Berns, J. D. Cohen, S. M. McClure, G. Pagnoni, “Hyperscanning: simultaneous fMRI during linked social interactions,” *Neuroimage*, **16**, 1159–1164 (2002).

- [71] Y. Fukui, Y. Ajichi, E. Okada, “Monte Carlo prediction of near-infrared light propagation in realistic adult and neonatal head models,” *Appl. Opt.* **42**, 2881–2887 (2003).
- [72] H. Kawaguchi, T. Koyama, E. Okada, “Effect of probe arrangement on reproducibility of images by near-infrared topography evaluated by a virtual head phantom,” *Appl. Opt.* **46**, 1658–1668 (2007).
- [73] M. Firbank, M. Oda, D. T. Delpy, “An improved design for a stable and reproducible phantom material for use in near-infrared spectroscopy and imaging,” *Phys. Med. Biol.* **40**, 955-961 (1995).
- [74] T. Funane, H. Atsumori, M. Kiguchi, Y. Tanikawa, E. Okada, “Dynamic phantom with two stage-driven absorbers for mimicking hemoglobin changes in superficial and deep tissues,” *J. Biomed. Opt.* **17**, 047001 (2012).
- [75] P. H. Koh, C. E. Elwell, D. T. Delpy, “Development of a dynamic test phantom for optical topography,” *Adv. Exp. Med. Biol.* **645**, 141-146 (2009).

Acknowledgements

I would like to express my deepest appreciation to Prof. Yukio Yamada for his continuing support and constant encouragement throughout this work. He not only gave me the opportunity to join his laboratory, but has also guided me towards the essence of research. Without his insightful discussions and constructive feedback on my presentations and papers, this work would not have been possible. It has been a great honor and privilege working under his supervision.

I am very grateful to Associate Professor Kazuto Masamoto for his invaluable comments during laboratory seminars and warm encouragement. I would particularly like to thank Associate Prof. Shinpei Okawa, who gave me useful advises on the FEM and beneficial comments at the beginning of this study.

I would like to express my gratitude to other members of this dissertation committee: Takuji Koike, Makoto Shimojo, Hiroshi Yokoi and Eiji Okada. They have taken their precious time to read the drafts and made valuable comments and suggestions to improve my dissertation.

I would also like to thank Dr. Yoko Hoshi and Ms. Yukari Tanikawa for their intriguing discussions related to this work.

I appreciate Yokoi Lab by providing NIRS imaging system for this work.

Special thanks to Ms. Nanae Shibahara, Mr. Daishi Kuramashi, Mr. Ryo Togashi, Mr. Zhen Nan and Mr. Takada Masakazu who developed the simulation and experiment environments for optical mapping. Thanks also go to other Yamada Lab members for being supportive and friendly.

I would like to thank the members of Masamoto Lab. In the past one and a half years, they gave me great assistance and happy memories. Again, I owe a very important debt to the Dongurien nursery school in UEC.

Finally, I want to thank my family for their understanding and love.

This work was partly supported by JSPS KAKENHI (No. 17360095 and No. 22360087).

Publications

a. Refereed publications the work is based on

- (1) Shuping Wang, Nanae Shibahara, Daishi Kuramashi, Shinpei Okawa, Naoto Kakuta, Eiji Okada, Atsushi Maki, and Yukio Yamada, Effects of spatial variation of skull and cerebrospinal fluid layers on optical mapping of brain activities, *Optical Review*, 17 (4), July,2010, pp. 410-420. (related to Chap. 3)
- (2) Shuping Wang, Yoko Hoshi, and Yukio Yamada, “Influences of Blood Flow Changes in Cerebrospinal Fluid and Skin Layers on Optical Mapping,” The 35th Annual International Conference of the IEEE Engineering in Medicine and Biology Society (IEEE EMBC2013), Osaka, Japan, July 3-7, 2013. (査読付) (related to Chap. 5)
- (1’) Shuping Wang, Nanae Shibahara, Daishi Kuramashi, Shinpei Okawa, Naoto Kakuta, Eiji Okada, Atsushi Maki, and Yukio Yamada, “Effects of Spatial Variation of Skull and Cerebrospinal Fluid Layers on Optical Mapping of Brain Activities,” The 4th Asian and Pacific Rim Symposium on Biophotonics (APBP2009), Jeju, Korea, May 27-29, 2009, pp. 114-115. (related to Chap. 3)
- (1’’) Mariko Oki, Nanae Shibahara, Ryo Togashi, Shuping Wang, Shinpei Okawa, Youko Hoshi, Yukio Yamada, “Effects of the anatomy of the head on optical mapping of brain activities,” The 4th Asian and Pacific Rim Symposium on Biophotonics (APBP2009), Jeju, Korea, May 27-29, 2009, pp. 129-130. (related to Chap. 4)

b. Other refereed publications

- (1) Shuping Wang, Lanqing Xu, Hui Li, and Yukio Yamada, “Diffusely Scattered Polarized Light in Turbid Media: Monte Carlo Simulation,” The 2nd Asian and Pacific Rim Symposium on Biophotonics (APBP2004), Taipei, Dec. 15-17, 2004, pp. 40-41.

- (2) Shuping Wang, Lanqing Xu, Hui Li, “Monte Carlo simulation of the diffusely scattered polarized light in turbid media,” Proceedings of SPIE, Vol. 5630, pp. 823-832 (2005).